Neoclassical Transport Theory for the Near-Axis Region of Tokamaks

Shinsuke Satake

Dissertation

Department of Fusion Science
School of Mathematical and Physical Science
The Graduate University for Advanced Studies

Doctor of Philosophy

March, 2003

Abstract

In the investigation of the transport phenomena in a magnetic confined plasma, neoclassical transport theory, which describes the transport processes of charged particles by Coulomb collisions in a torus configuration, has played an important role. Neoclassical transport theory in a tokamak has been studied in detail from the beginning of fusion research, and it has been regarded as being a well-established theory.

Recently, however, it has been found that the conventional neoclassical transport theory cannot be applied to some parameter regimes in the improved confinement plasma experiments. Particularly, in a reversed magnetic shear discharge which accompanies an improved confinement region called the internal transport barrier (ITB), the observed ion thermal temperature T_i and the safety factor q around the magnetic axis sometimes become much higher than those in a normal magnetic shear configuration with no improvement of core plasma confinement. In a reversed shear configuration, the ion orbit width in the minor radial direction becomes wider, and the conventional neoclassical transport theory, which is based on the small orbit width (SOW) approximation, is not valid in the near-axis region. In fact, the observed ion thermal conductivity in reversed shear configuration discharges is sometimes below the standard neoclassical transport level around the magnetic axis.

In this dissertation, a new formulation of neoclassical transport theory which correctly reflects the finite orbit width (FOW) effect of the particle orbits appearing around the magnetic axis is constructed, and it is applied to the numerical calculation of the ion thermal conductivity near the magnetic axis. The contents consist of three parts as follows:

1. As the basis of the transport analysis, a precise investigation of particle orbits near the magnetic axis is shown. In the near-axis region, there appear characteristic orbits with a relatively wide width called Potato orbits. A clear classification of these non-standard particle orbits, which have not been properly treated in the conventional studies of neoclassical transport, is established. It is shown that the conventional neoclassical transport theory should be largely modified

by considering the effect of potato particles in the near-axis region.

2. To include the orbital properties of potato particles in neoclassical transport theory, Lagrangian approach of transport analysis is adopted. In this approach, the transport equations are derived based on the reduced drift kinetic equation described in a Lagrangian representation, in which three constants of motion (COM) along each particle orbit in the collisionless limit (the particle energy $\mathcal{E}$, the magnetic moment μ, and the averaged poloidal flux surface position $\langle\psi\rangle$) are chosen as the independent variables in the phase space. The transport coefficients are obtained by integrating information of the background field along the exact orbit of each particle. Therefore, Lagrangian formulation can correctly include the FOW effect to neoclassical transport.

3. Using the Lagrangian transport theory, the ion thermal conductivity χ_i around the magnetic axis is calculated numerically. In the calculation, the orbital properties of potato orbits are correctly reflected. It is found that the resultant χ_i is lower than that predicted by conventional neoclassical transport theory. The Lagrangian approach can explain the reductive tendency of χ_i near the magnetic axis found both in recent experiments and in other transport simulations using the δf Monte Carlo method. An advanced numerical calculation method of parallelized computing by Message Passing Interface (MPI) is adopted in the calculation.

The advanced point in this work is that we develop the Lagrangian transport theory so as to be applicable to the numerical calculation in realistic cases for the first time. We introduce a model collision operator which is suitable to handle in analysis and also retain the important property of momentum conservation of the collision operator. Applying the model collision operator enables us to treat the transport caused by the like-species particle collisions in the Lagrangian formulation, which is not correctly treated in previous studies on the Lagrangian transport theory using simple Lorentz approximation collision operator. We also derive the explicit expression of the Jacobian in the COM space $(\mathcal{E}, \mu, \langle\psi\rangle)$ for the first time which is essential to apply the formulation to numerical calculations. The numerical method of integration in the $(\mathcal{E}, \mu)$ space, of which the integral region cannot be given analytically, is proposed by applying the Monte Carlo integration method. The numerical method enables us to calculate transport coefficients in a quantitatively correct way with including the FOW effect of potato orbits.

The formulation of the Lagrangian transport theory shown in this dissertation can

reproduce the results of the standard neoclassical theory in the region away from the axis. We can see quantitatively how the presence of potato particles affects neoclassical transport as approaching to the magnetic axis. It is shown that the region in which χ_i reduces from the standard neoclassical level expands outward from the magnetic axis as the potato width becomes wider in a reversed magnetic shear configuration, in which the q-factor around the axis is relatively higher than that in a normal shear configuration. Therefore, it is found that Lagrangian transport analysis including the FOW effect is really important to consider the transport phenomena in a reversed shear configuration, which attracts much attention in these days.

In this study, the effectiveness of the Lagrangian approach in transport analysis with the FOW effect is demonstrated for the first time. We believe that this work have made a breakthrough to utilize Lagrangian approach in various transport problems in plasmas.

Acknowledgement

First of all, I would like to thank my supervisor, Dr. Masao Okamoto for having kindly advised me throughout my doctor course. I thank him especially for having given me the freedom to work, and for having welcomed discussions with me at anytime. I had received much inspiration on this work from fruitful discussions with him.

I am also grateful to Dr. Hideo Sugama for having encouraged and helped me to acquire a more comprehensive understanding of neoclassical transport theory. In my doctor course, it had been my pleasure to have had beneficial seminars on plasma physics with him.

As concerning this work, I would like to thank Dr. Noriyoshi Nakajima for giving useful suggestions on the numerical calculation method. I am very grateful to Dr. Wei-xing Wang for providing precise data of his simulations. I am also grateful to Dr. Masahiro Wakatani for having suggested this challenging and interesting topic of neoclassical transport theory for my master thesis, which has grown into the main theme of my dissertation. I would like to acknowledge all the staffs in Theory and Data Analysis Division in NIFS for their friendliness and for having given me a lot of suggestions on my work. At last, I would like to express my sincere thanks to my parents.

This work is supported by JSPS Research Fellowships for Young Scientists No. 10177.

There's no way in front of me,
It just appears behind me as I go.
Oh Nature, my Father
You raised me alone and independent,
My vast and great Father.
So don't take your eyes off me
And guard me, please.
Always fill me with your intrepid spirit
In order to go on my long way,
In order to walk this long way of mine.

Journey, by Koutaro Takamura.

Contents

Chapter 1

Introduction

Recently, neoclassical transport in the core region of tokamaks has attracted much attention again. It is well-known that there appear non-standard guiding-center orbits near the magnetic axis called "potato" orbits[1]. Typical orbit width of potato particles is as large as $(q^2\rho^2 R_0)^{1/3}$, where q is the safety factor, ρ is the Larmor radius, and R_0 is the major radius, respectively. In recent tokamak experiments in reversed magnetic shear configuration accompanied by the internal transport barrier (ITB)[2, 3, 4, 5], the measured ion thermal conductivities in the core region sometimes become lower than those predicted by a conventional neoclassical transport theory[2, 5, 6, 7]. In fact, the standard neoclassical transport theory[8, 9] constructed in the small-orbit-width (SOW) approximation is not applicable to the near-axis region, and the orbital properties of potato particles should be considered in analyzing transport in this region. Then, several transport theories have been presented to include the effect of potato particles[10, 11, 12, 13, 14], and Monte Carlo simulations (so called the δf-method)[15, 16, 17, 18, 19] have also been carried out to calculate the ion thermal conductivity χ_i in the near-axis region. However, there exist differences in the resultant χ_i depending on the models used in analytical calculations, and neoclassical transport theory in the near-axis region has not been completed yet.

Neoclassical transport theory has usually been discussed in an Eulerian representation. Then, the extension of the theory to the near-axis region has also been discussed in an Eulerian manner. However, to include nonlocal orbital properties in the transport theory, Lagrangian formulation[20, 21, 22] has been found to be suitable for a collisionless (banana-regime) plasma. In this approach, transport phenomena are described by a reduced drift-kinetic equation in the phase space of three constants-of-motion (COM) along each collisionless particle orbit in an axisymmetric system. The previous works have proven that Lagrangian formulation can reproduce the results obtained from the

standard Eulerian formulation built in the SOW limit in the region away from the magnetic axis.

The present article is the first practical application of the Lagrangian formulation to the near-axis region in which the finite-orbit-width (FOW) effect becomes really important. To utilize Lagrangian transport theory, we improve the treatment of like-particle collision term in the formulation to retain the momentum conservation property. It is also shown that our formulation with the model collision operator is suitable to numerical calculation. In contrast to the other Lagrangian approaches using some analytical approximations, our calculation reflects quantitatively correct properties of all types of particles appearing around the magnetic axis. It is found that the ion thermal conductivity χ_i obtained by the Lagrangian transport theory becomes significantly lower than that predicted by the conventional Eulerian theory. It is shown that the reduction of χ_i from the standard neoclassical level occurs in the range of a typical potato orbit width from the magnetic axis $r \lesssim 2(2q^2\rho^2R_0)^{1/3}$. Therefore, the modification of neoclassical transport theory is really important in a reversed shear configuration since potato width is proportional to $q^{2/3}$, and the q-factor becomes large near the axis in this configuration. Our result can explain the reductive tendency of χ_i found in the recent results of both Monte Carlo simulations and experimental diagnostics in the core region.

This dissertation is organized as follows. In Chapter 2, the analysis of guiding-center orbits is reviewed[23], and the classification of orbit types in the COM space is presented. The reduced kinetic equation and collision operator in the COM space are derived in Chapter 3, and the transport equation is obtained by solving the kinetic equation[24]. We also discuss how to compare the neoclassical fluxes between Lagrangian and Eulerian representations. Transport coefficients including the ion thermal conductivity in the near-axis region are calculated numerically in Chapter 4. The comparison between the ion thermal conductivity calculated by our formulation and those obtained from experiments or other Monte Carlo simulations is shown in Chapter 5. Finally in Chapter 6, the summary of this dissertation is given. Main results and future studies relating to this thesis are discussed.

Chapter 2

Particle orbit near the magnetic axis

2.1 Introduction

As a beginning of this chapter, let us look back briefly the conventional analysis on particle orbit and see what is the problem when considering neoclassical transport in the region near the magnetic axis. Particle orbits in tokamaks have already been investigated in detail for the region away from the axis. For example, a radial width of a trapped particle, or a "banana width", is approximated in the conventional analysis as[25]

$$\Delta_b \sim \sqrt{\epsilon}\rho_p, \tag{2.1}$$

where $\epsilon = r/R_0$ is the inverse aspect ratio and $\rho_p = mv/eB_p$ is the poloidal Larmor radius. The fraction of trapped particles is given as

$$f_t \sim \sqrt{\epsilon}. \tag{2.2}$$

These characteristic quantities can be written by local values such as ϵ and ρ_p when an instant radial position of a particle r is assumed to be much larger than the banana width of the orbit Δ_b; $\Delta_b/r \ll 1$. According to Eq. (2.1), a banana width seems to be infinity on the magnetic axis because $\rho_p \propto 1/B_p \propto 1/r$. However, equations (2.1) and (2.2) are invalid near the axis. Actually, both the banana width and the fraction of banana particles are finite on the magnetic axis as found by Stix[26]. The typical orbit width of trapped particles passing near the magnetic axis, which are called "potato" particles[1], is $\sim (q^2\rho^2R_0)^{1/3}$, where q is the safety factor and $\rho = mv/eB_0$ is the gyroradius.

This invalidity in orbit analysis is also responsible for the reason why the standard neoclassical transport theory[8, 9] cannot be applied to the near-axis region. In a simple

estimation, the neoclassical diffusion and thermal conductivity D and χ are given as[27]

$$D, \chi \sim f_t \nu_{eff} \Delta_b^2 \propto \epsilon^{-3/2} \nu \rho^2, \tag{2.3}$$

where $\nu_{eff} = \nu / f_t^2$ is the effective collision frequency for banana particles. These coefficients seem to go to infinity on the axis. However, this estimation is obviously incorrect because the actual orbit properties neat the axis are not evaluated properly. In this way, it has been recognized that a detailed investigation about the properties of particle orbits is important and constitutes the basis of the neoclassical transport theory for the near-axis region. The most important point in analyzing particle orbits near the magnetic axis is to take account of the finiteness of orbit width, since in this region the ordering $\Delta_b / r \ll 1$ is not valid.

As we will see in this chapter, there appears various types of particle orbits which are characteristic in the near-axis region. To make a clear classification of such orbits, we introduce two signs with respect to particle motions :

$$\sigma_{\|} \equiv \frac{v_{\|}}{|v_{\|}|}, \tag{2.4}$$

$$\sigma_{\theta} \equiv \frac{\dot{\theta}}{|\dot{\theta}|}, \tag{2.5}$$

where $v_{\|}$ is the velocity component parallel to the magnetic field. The poloidal angular velocity $\dot{\theta}$ is defined as

$$\dot{\theta} \equiv \mathbf{v} \cdot \nabla \theta = (\mathbf{v}_{\|} + \mathbf{v}_d) \cdot \nabla \theta, \tag{2.6}$$

where $\mathbf{v}_d$ is the sum of the grad-B, curvature, and $\mathbf{E} \times \mathbf{B}$ drift velocities. Conventionally, orbit topology is classified as "passing" or "trapped" depending on whether the sign of parallel velocity $\sigma_{\|}$ reverses along an orbit or not. However, particle orbits passing near the magnetic axis are strongly affected by the grad-B and curvature drifts, and there appear new types of orbit. We show later that all these orbit types can be properly classified by counting the number of turning points of both $\sigma_{\|}$ and σ_{θ}.

In connection with the Lagrangian transport theory in §3, we show in this chapter two classifications of orbit types in the space of constants of motion (COM). One can make a set of COM (z_1, z_2, z_3), where z_1, z_2, z_3 are independent, arbitrary functions of well-known three constants of motion of particles in an axisymmetric, collisionless system : the particle energy $\mathcal{E}$, the magnetic moment μ, and the canonical angular momentum P_{ζ}.

For a detailed understanding on orbit properties near the axis, we first use in §2.2 a familiar choice of COM : $(z_1, z_2, z_3) = (v, \xi_s, r_s)$, where v is the particle velocity, r_s

is the minor radius at which the orbit crosses the mid-plane $Z = 0$, and $\xi_s = v_\parallel/v$ is the cosine of the pitch angle on that point. Particle orbit analysis in this space has been investigated by Chu [28] and Egedal[29]. In the present paper, a simple analytic expression of the boundary for each type of orbit is given.

Our Lagrangian transport theory is developed in the COM space $(\mathcal{E}, \mu, \langle r \rangle)$ proposed by S. Wang [22], where $\langle r \rangle$ is the bounce-averaged radial position of a particle. The classification of particle orbits in this space is shown in §2.3. This description is more convenient and physically more understandable than that in the former choice of COM in utilizing it for Lagrangian formulation. In the $(\mathcal{E}, \mu, \langle r \rangle)$ space, the classification of orbit types proposed here becomes important.

2.2 Analysis of orbits near the magnetic axis

Let us consider an axisymmetric configuration like a tokamak. Coordinates are chosen as in Fig. 2.1; r is the minor radius, ζ the toroidal angle, and θ the poloidal angle. A general axisymmetric magnetic field is written as $\mathbf{B} = I\nabla\zeta + \nabla\zeta \times \nabla\psi$, where $I = RB_t$ and ψ is the poloidal flux. For simplicity, we assume that the magnetic surfaces have concentric circular poloidal cross sections and that the safety factor q is constant. Then the poloidal flux can be written as $\psi = (B_0 r^2)/(2q)$, where $B_0 = I/R_0$ is the magnetic field strength on the magnetic axis $R = R_0$. Note that we take $\mathbf{j} \cdot \mathbf{B} > 0$, where $\mathbf{j}$ is the plasma current density. In an axisymmetric system, there are three constants of motion as follows:

$$\mathcal{E} = \frac{mv^2}{2} + e\Phi \quad : \quad \text{Total energy of a particle,} \tag{2.7a}$$

$$\mu = \frac{mv_\perp^2}{2B} \quad : \quad \text{Magnetic moment,} \tag{2.7b}$$

$$P_\zeta = \psi - \frac{Iv_\parallel}{\Omega} \quad : \quad \text{Canonical angular momentum,} \tag{2.7c}$$

where Φ is the electrostatic potential and $\Omega = eB/m$ is the gyrofrequency. Particle motion averaged with respect to gyrophase is described by the guiding-center equations of motion. To the lowest order in ρ/L, where ρ is the gyroradius and L the gradient scale length of the magnetic field, they are written as

$$\mathbf{v} = v_\parallel \mathbf{b} + \frac{\mathbf{b}}{m\Omega} \times (\mu\nabla B + mv_\parallel^2 \mathbf{b} \cdot \nabla\mathbf{b}), \tag{2.8}$$

$$\frac{dv_\parallel}{dt} = -\frac{\mu}{m}\mathbf{b} \cdot \nabla B, \tag{2.9}$$

where $\mathbf{b}$ is the unit vector parallel to the magnetic field. The $\mathbf{E} \times \mathbf{B}$ drift is neglected in the orbit analysis here. The second term on the right-hand side of Eq. (2.8) represents

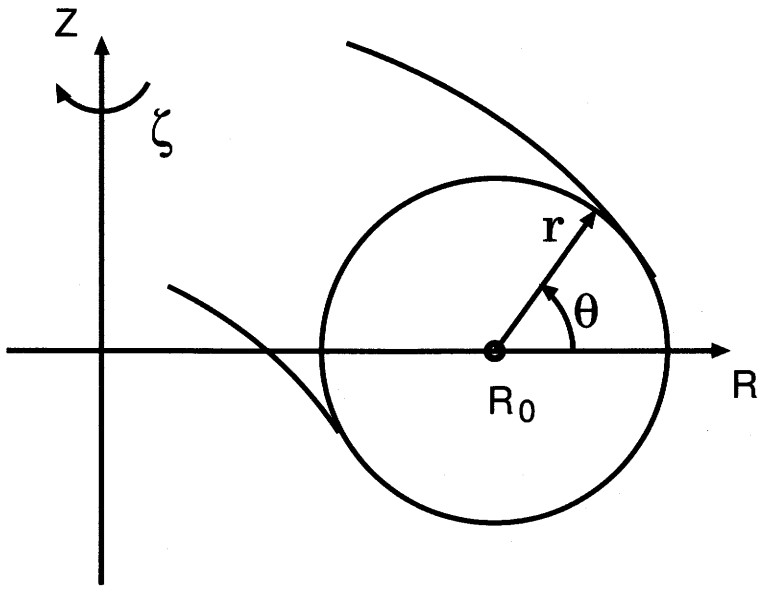

Figure 2.1: Coordinate system.

the drift velocity $\mathbf{v}_d$. Using the large-aspect-ratio and low-β approximations, we can write

$$B \simeq \frac{B_0}{1+\epsilon\cos\theta} \simeq B_0(1-\epsilon\cos\theta), \tag{2.10a}$$

$$\mathbf{v}_d \simeq -\frac{1}{R_0\Omega_0}\left(v_\parallel^2+\frac{1}{2}v_\perp^2\right)\hat{z}, \tag{2.10b}$$

where $\Omega_0 = eB_0/m$. From these expressions, the poloidal angular velocity is written as

$$\dot{\theta} \equiv \mathbf{v}\cdot\nabla\theta = \frac{1}{qR_0}\left[v_\parallel - \frac{q}{r\Omega_0}\left(v_\parallel^2+\frac{1}{2}v_\perp^2\right)\cos\theta\right], \tag{2.11}$$

which shows that the contribution of $\mathbf{v}_d$ to $\dot{\theta}$ increases proportional to $1/r$ near the magnetic axis. Particle orbits can be analyzed with the three constants of motion and Eqs. (2.8) – (2.11).

Examples of orbits near the axis numerically calculated by Eqs. (2.8) and (2.9) are shown in Figs. 2.2 – 2.5. In these figures, orbits of hydrogen ions with $\mathcal{E} = 10\text{keV}$ are plotted, where other parameters are given as $R_0 = 4\text{m}$, $q = 3$, and $B_0 = 4\text{T}$, respectively. The arrows in these figures represent the direction of the particle motion. In the calculations, the minor radius of the starting point r_s on the mid-plane $Z = 0$ and the cosine of the pitch angle of velocity at that point $\xi_s = v_\parallel/v$ are given as initial conditions. Orbit types are classified below according to the number of turning points of $\sigma_\parallel$ and σ_θ defined in Eqs. (2.4) and (2.5), respectively.

Figure 2.2 shows the orbits of passing particles. Both the signs $\sigma_\parallel$ and σ_θ are constant over the orbits. The radial displacement of a passing orbit ($|r(\theta=0)-r(\theta=\pi)|$) has a minimum value for the particles with $\xi_s = \pm 1$, as in the orbits B and D. From the equation of conservation of P_ζ and noting the fact that $v_\parallel = \pm v$ for such particles, one can find that the minimum displacement is $2q\rho$. On the other hand, A and C are the passing orbits which have the maximum radial displacement starting from the same positions as in B and D. As shown later in Fig. 2.6, these particles are on the boundary to other types of orbit. Though the maximum displacement of passing orbit near the axis becomes as large as $(q^2\rho^2 R_0)^{1/3}$, most of the passing particles still have a small displacement of the order of $q\rho$.

Figure 2.3 shows banana orbits. We identify banana orbits with those which have two turning points for each of $\sigma_\parallel$ and σ_θ, and then do not encircle the magnetic axis. The banana width, which is measured on the mid-plane, increases when the orbit is close to the magnetic axis, but it remains finite even if the orbit passes through the axis. The orbit E in Fig. 2.3 represents the widest banana orbit. To obtain the maximum banana width, let us consider a particle which starts from the magnetic axis $r_s = 0$ with $\xi_0 = v_{\parallel 0}/v < 0$. If the particle has the turning point at $(r,\theta) = (r_1,\pi)$, then $\dot{\theta} = 0$ on that point. Therefore, from Eq. (2.11), we obtain

$$r_1 = -\frac{q}{v_{\parallel 1}\Omega_0}\left(v_{\parallel 1}^2 + \frac{1}{2}v_{\perp 1}^2\right) \simeq -\frac{q}{v_{\parallel 1}\Omega_0}\frac{\mu B_0}{m}\left(1+\frac{r_1}{R_0}\right). \tag{2.12}$$

where $v_{\parallel 1}$ and $v_{\perp 1}$ are the parallel and perpendicular velocities at $r = r_1$ respectively, and we use an approximation $v_{\parallel 1}^2 \ll v_{\perp 1}^2$ on the turning point. On the other hand, from the conservation of $\mathcal{E}$ and P_ζ at $r = 0$ and r_1, we have

$$\frac{v_{\parallel 0}^2}{2} + \frac{\mu B_0}{m} = \frac{v_{\parallel 1}}{2} + \frac{\mu B_0}{m}\left(1+\frac{r_1}{R_0}\right), \tag{2.13}$$

$$v_{\parallel 0} = v_{\parallel 1} - \frac{\Omega_0 r_1^2}{2qR_0}. \tag{2.14}$$

Solving Eqs. (2.12) – (2.14), we obtain

$$r_1 = (2q^2\rho^2 R_0)^{1/3}, \tag{2.15}$$

$$\xi_0 = -\frac{3}{2}\left(\frac{q\rho}{2R_0}\right)^{1/3}. \tag{2.16}$$

Note that we take $\rho = v/\Omega_0$ here and hereafter. Solving similar equations for constants of motion concerning $(r,\theta) = (r_1,\pi)$ and $(\Delta_p, 0)$, we obtain the maximum banana width Δ_p,

$$\Delta_p = 2r_1 = 2(2q^2\rho^2 R_0)^{1/3}. \tag{2.17}$$

Lin, Tang, and Lee [15] showed a similar result, but it has different numerical factors. It is because they used $v_{\|1} = 0$ as the condition of the turning point of $\dot{\theta}$. As shown in Fig. 2.3, the positions of $v_\| = 0$ and $\dot{\theta} = 0$ tend to deviate from each other on a banana orbit passing near the magnetic axis. Therefore, using $\dot{\theta} = 0$ as the poloidal turning condition is more correct in the orbit analysis.

Figure 2.4 shows orbits of a typical type appearing near the magnetic axis. These particles have a constant $\sigma_\|$ but σ_θ changes twice on the orbits. They are located on the inside or the outside of the torus and are poloidally trapped. We name those orbits with $\sigma_\| = +1$ "outer-circulating" (solid lines), and those with $\sigma_\| = -1$ "inner-circulating" (dashed lines). Note that this criterion is reversed for electrons, or when the direction of the parallel current is anti-parallel to the magnetic field. The maximum width of outer-circulating orbit Δ_{oc} can be obtained by solving the equations of motion for the particle with $(r_s, \xi_s) = (0, 0)$, which corresponds to the orbit G. The result is

$$\Delta_{oc} = (4q^2\rho^2 R_0)^{1/3}. \tag{2.18}$$

On the other hand, the widest inner-circulating orbit H corresponds to the inner part of the widest banana orbit E in Fig. 2.3. Thus we obtain

$$\Delta_{ic} = r_1 = (2q^2\rho^2 R_0)^{1/3}. \tag{2.19}$$

The minimum width of circulating orbits is zero. Such particles are stagnated on the mid-plane, and move only in the toroidal direction. Stagnation occurs when a particle satisfy $\dot{\theta} = 0$ and $\dot{r} = 0$ on the mid-plane, and by solving Eq. (2.11) we have

$$r_s = \frac{q\rho}{2\xi_s}(1 + \xi_s^2) \quad \text{: stagnation condition.} \tag{2.20}$$

Note that the domain of r_s is extended to negative values, where $r_s < 0$ represents the starting point of a inner-circulating orbit $(r, \theta) = (|r_s|, \pi)$.

A remarkable difference between outer- and inner-circulating orbits is the region in which each type of orbit can exist. Like the orbit J, inner-circulating orbits can exist only in the region $-\Delta_{ic} \leq r_s \leq 0$ enclosed by the widest one; the orbit H. On the other hand, outer-circulating orbits can exist away from the axis $r_s \geq \Delta_{oc}$ like the orbit I. Orbits like I are conventionally classified as "deeply-trapped" banana, but in fact they have no turning point of $\sigma_\|$ and can move freely in the toroidal direction.

Figure 2.5 shows orbits which encircle the magnetic axis but are magnetically trapped, i. e., $\sigma_\|$ changes twice on these orbits. We divide these orbits further into two types. One type consists of the orbits which have four turning points of σ_θ like the orbit L in

Table 2.1: Classification of particle orbits.

Orbit type	Turning points of $\sigma_{\parallel}$, σ_θ	Sign of $\sigma_{\parallel}$
Passing	0 , 0	+ or −
Banana	2 , 2	±
Outer-circulating	0 , 2	$+^a$
Inner-circulating	0 , 2	$-^a$
Kidney	2 , 0	±
Concave-kidney	2 , 4	±

[a] For ions. The sign is opposite for electrons.

Fig. 2.5. The other consists of the orbits which have no turning point of σ_θ like the orbit M. We name the former "concave-kidney" to distinguish it from the latter called "kidney" by Chu [28]. Concave-kidney orbits have a larger radial displacement than kidney orbits.

The summary of the classification of orbits is shown in Table 2.1. Orbits are clearly classified by the number of turning points of $\sigma_{\parallel}$ and σ_θ. One can see that all the orbits which are poloidally trapped (banana, inner-circulating, and outer-circulating orbits) have two turning points of σ_θ.

In the classification shown here, the terminology "potato orbit" is not used. Originally, potato orbits are defined as those which have a typical orbit width $\Delta_r \sim (q^2\rho^2 R_0)^{1/3}$[1]. We have shown that various types of orbits have this characteristic width, for example Δ_p, Δ_{oc} and Δ_{ic}. Then it is difficult to make a mathematically specific criterion for potato orbits. In this text, therefore, we use the classification defined in Table 2.1 to mention a specific orbit type, and "potato orbit" is used as a generic term referring to typical orbits near the magnetic axis with $\Delta_r \sim (q^2\rho^2 R_0)^{1/3}$.

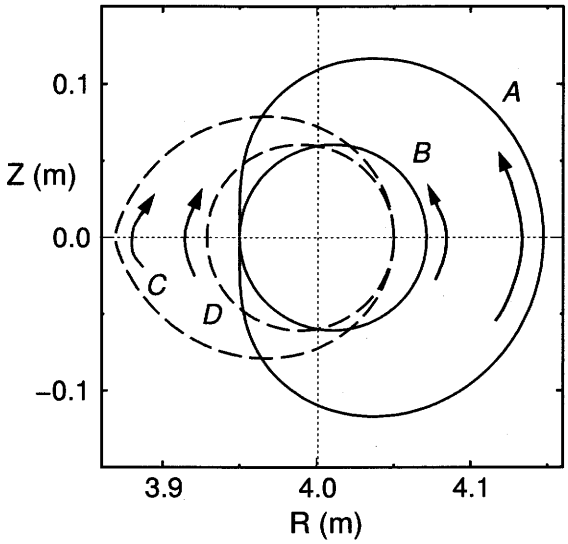

Figure 2.2: Orbits of passing particles. Solid lines represent co-passing orbits ($v_\parallel > 0$) and dashed lines counter-passing orbits ($v_\parallel < 0$). The maximum radial displacement of passing orbit near the axis is shown by the orbit A or C, which is as large as $\sim (q^2\rho^2 R_0)^{1/3}$. However, most of the passing orbits have a small radial displacement $\sim 2q\rho$ as shown by the orbits B and D.

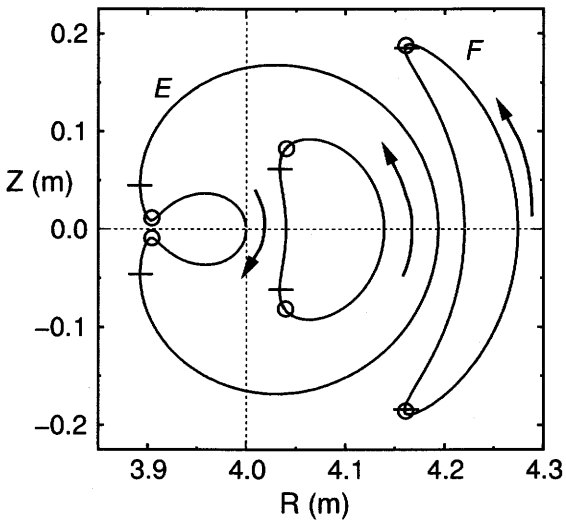

Figure 2.3: Orbits of banana particles. The circles and the bars marked on these orbits represent the turning points of the sign σ_θ (poloidal angular velocity) and $\sigma_\parallel$ (parallel velocity), respectively. Near the magnetic axis, these two kinds of turning point tend to deviate from each other. The orbit E is the widest banana of which the radial width is Δ_p given by Eq. (2.17).

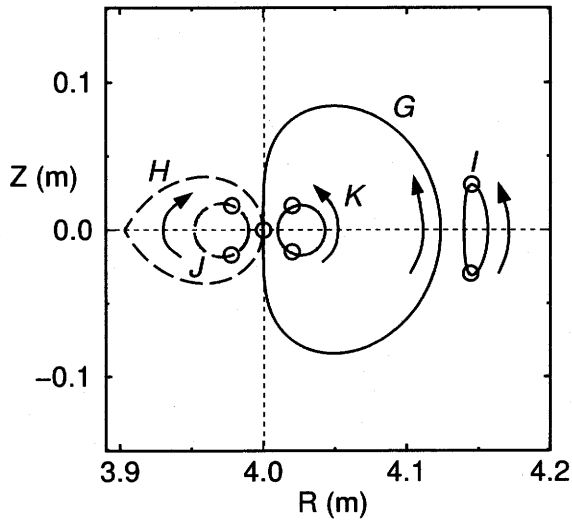

Figure 2.4: Orbits of outer-circulating particles (solid lines) and inner-circulating particles (dashed lines). The sign $\sigma_{\|}$ is positive for outer-circulating orbits, while it is negative for inner-circulating orbits. Orbits G and H are the widest ones for outer- and inner-circulating orbits, respectively. Inner-circulating orbits exist only in the region enclosed by the orbit H. Outer-circulating orbits can exist away from the magnetic axis like the orbit I.

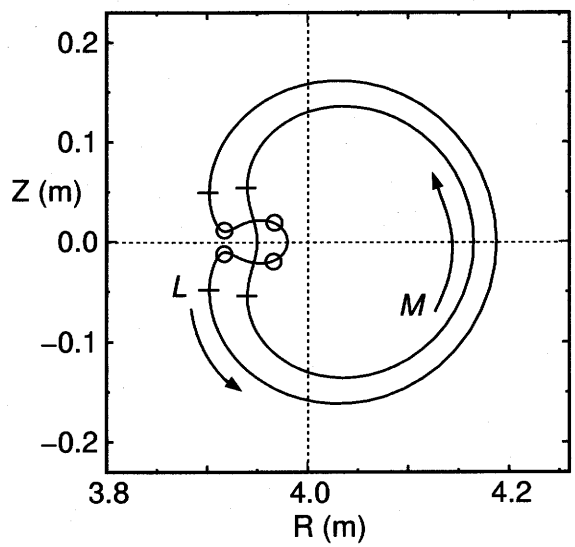

Figure 2.5: Orbits of concave-kidney L and kidney M. Only concave-kidney particles have four turning points of σ_θ, while $\sigma_{\|}$ changes twice on both types of orbit.

2.3 Classification in the (v, ξ_s, r_s) space

In this section, we classify orbit types in the (v, ξ_s, r_s) space, where r_s and ξ_s is defined in §2.2. This set of COM is often used to classify orbit types, and a similar set of COM is used in the Lagrangian formulation of transport theory by Zaitsev *et al.*[21].

The regions and the boundaries in the (r_s, ξ_s) plane for each type of orbit of ions with $\mathcal{E} = 10$keV in the model configuration used in §2.2 are shown in Fig. 2.6, and the regions near the origin and near the concave-kidney region are magnified in Figs. 2.7 and 2.8, respectively. In Figs. 2.6 – 2.8, negative r_s means the crossing points of particle orbits on the mid-plane $Z = 0$ at the inside of the torus; $(r, \theta) = (|r_s|, \pi)$. The extension of r_s to the negative region makes it convenient to express boundaries of orbit types. A similar expression is used in a paper by Egedal[29].

The points (r_s, ξ_s) which correspond to the orbits A to M in Figs. 2.2 – 2.5 are plotted in Figs. 2.6 – 2.8. Note that there are two different points in the (r_s, ξ_s) plane corresponding to the same one orbit, because any orbit crosses the mid-plane twice. In Fig. 2.6, the points E, G and H correspond to orbits with maximum width for banana Δ_p, outer-circulating Δ_{oc}, and inner-circulating Δ_{ic}, respectively. We newly distinguish the region of concave-kidney (vi) from the region kidney (v). This distinction becomes important in the next section in which orbits are classified in the $(\mathcal{E}, \mu, \langle r \rangle)$ space.

In the case of a simple model configuration used here, boundaries of orbit types can be solved analytically. Dotted lines in the circulating regions in Fig. 2.6 correspond to the orbits stagnated at $Z = 0$ and r_s given by Eq. (2.20). The other boundaries are given as follows.

First, the boundary *b1* which lies between the outer-circulating and co-passing regions and between the inner-circulating and counter-passing regions is obtained from equations like (2.13) and (2.14) for a particle passing through the magnetic axis. The result is

$$\xi_s = \frac{1}{2}\left[\frac{R_0}{q\rho}\epsilon_s(1+\epsilon_s) \pm \sqrt{\left(\frac{R_0^2\epsilon_s^2}{q^2\rho^2} - 4\right)(1+\epsilon_s+\epsilon_s^2)}\right], \tag{2.21}$$

where $\epsilon_s = r_s/R_0$ and we choose $-$ for $2q\rho \le r_s \le \Delta_{oc}$ (the boundary of the outer-circulating region) and $+$ for $-\Delta_{ic} \le r_s \le -2q\rho$ (the boundary of the inner-circulating region). We have used the large-aspect-ratio approximation and the terms higher than $O(\epsilon_s^3)$ have been neglected. This equation also represents the boundary between the banana and concave-kidney regions E-G at $\Delta_{oc} < r_s < \Delta_p$ in Fig. 2.8.

Second, to obtain the boundaries between the concave-kidney and kidney regions G-X in Figs. 2.6 and 2.8, let us consider a concave-kidney particle which starts from

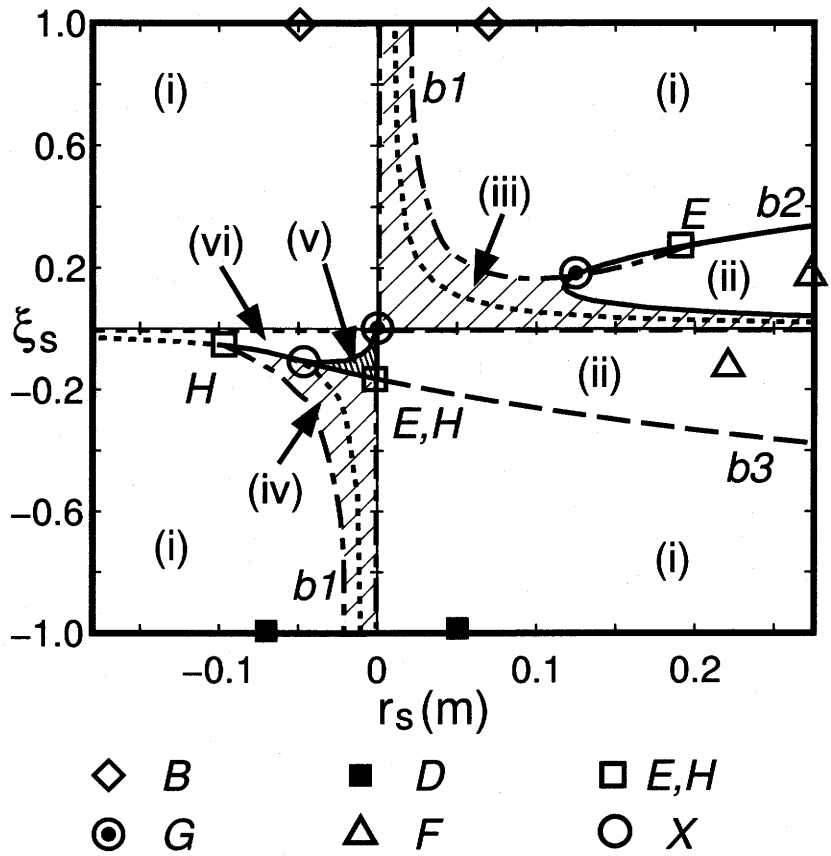

Figure 2.6: The regions and the boundaries for each type of orbit in the (r_s, ξ_s) plane, where r_s is the minor radius at which orbits cross the mid-plane $Z = 0$, and $\xi_s = v_{\|}/v$ at that point. Negative r_s means the inside of the torus. The regions (i) – (vi) correspond to (i) passing, (ii) banana, (iii) outer-circulating, (iv) inner-circulating, (v) concave-kidney, and (vi) kidney, respectively. Dotted lines given by Eq. (2.20) in the circulating regions correspond to the stagnated orbits with $\dot{r} = \dot{\theta} = 0$. Dash-dotted lines *b1* are given by Eq. (2.21). Solid line *b2* enclosing the region (ii) is given by Eq. (2.27). Dashed line *b3* is given by Eq. (2.28). Pairs of the same marks B, D, etc. correspond to the orbits in Figs. 2.2 – 2.5. (See also Figs. 2.7 and 2.8 for some orbits not shown here.)

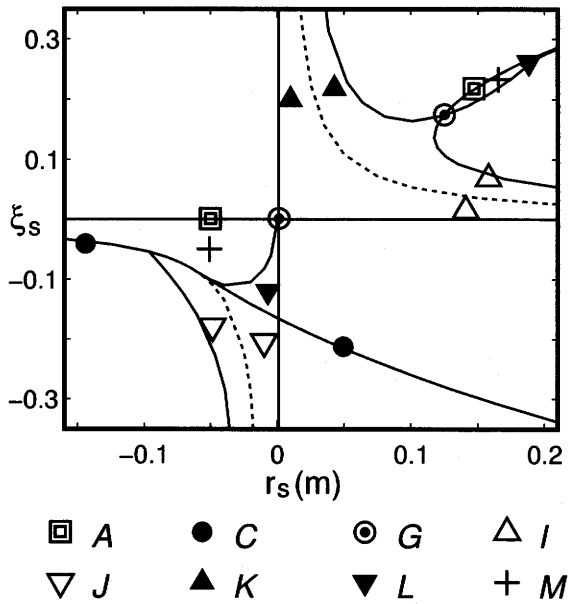

Figure 2.7: A magnification of the region near the origin in the (r_s, ξ_s) plane in Fig. 2.6. Pairs of marks correspond to the orbits in Figs. 2.2 – 2.5.

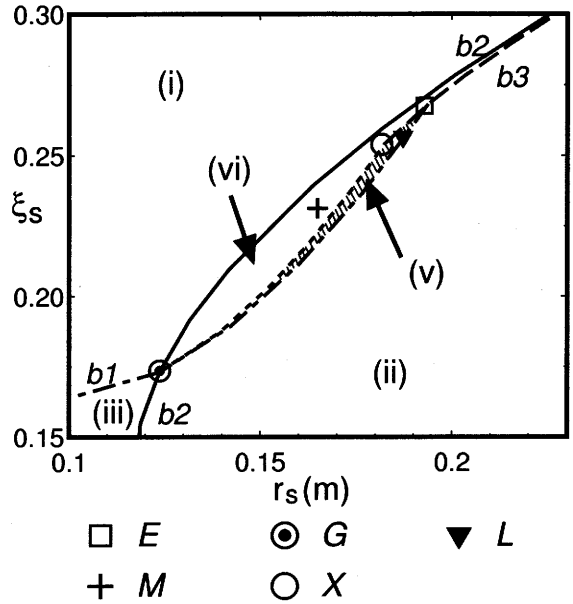

Figure 2.8: The regions of concave-kidney (v) and kidney (vi) at $r_s > 0$. The boundary G-X between these two regions plotted by the dotted line is given by Eq. (2.26). Other lines and marks are defined in the same way as in Fig. 2.6.

the point $(r, Z) = (r_s, 0)$ and turns at (r_t, θ_t). The equations of the constants of motion are written as

$$\frac{v_{\|s}^2}{2} + \frac{\mu B_0}{m}(1 - \epsilon_s) = \frac{v_{\|t}^2}{2} + \frac{\mu B_0}{m}(1 - \epsilon_t \cos\theta_t), \tag{2.22}$$

$$v_{\|s} - \frac{\Omega_0 r_s^2}{2qR_0} = v_{\|t} - \frac{\Omega_0 r_t^2}{2qR_0}, \tag{2.23}$$

where the subscripts s and t mean the values at the points $r = r_s$ and r_t respectively. From the condition $\dot{\theta} = 0$ at (r_t, θ_t), we obtain

$$\cos\theta_t = \frac{2r_t\xi_t}{q\rho(1 + \xi_t^2)} \quad (< 0). \tag{2.24}$$

Combining Eqs. (2.22) – (2.24), we obtain

$$-\left(\frac{1 - \epsilon_s}{1 - \xi_s^2}\right)\xi_t^4 + 3\xi_t^2 - 4\left(\xi_s - \frac{R_0}{2q\rho}\epsilon_s^2\right)\xi_t + \frac{(\xi_s^2 - \epsilon_s)}{(1 - \xi_s^2)} = 0. \tag{2.25}$$

The necessary condition for a concave-kidney particle to exist is that Eq. (2.25) has real solutions for ξ_t. Therefore, the boundaries G-X in the (r_s, ξ_s) plane are approximately

given by the discriminant of Eq. (2.25) (neglecting $O(\xi_t^4)$ term),

$$D = 4\left(\xi_s - \frac{R_0}{2q\rho}\epsilon_s^2\right)^2 - \frac{3(\xi_s^2 - \epsilon_s)}{(1-\xi_s^2)} = 0. \tag{2.26}$$

Third, solving equations for a particle which passes the mid-plane $Z = 0$ with $\xi = 0$, we obtain

$$\xi_s^3 - \frac{4q\rho}{R_0}\xi_s^2 - 2\epsilon_s(1-\epsilon_s)\xi_s + \frac{2q\rho}{R_0} = 0. \tag{2.27}$$

This equation, which corresponds to the boundary *b2* in Figs. 2.6 and 2.8, has two real solutions $\xi_s > 0$ in the region $r_s \gtrsim 1.5(q^2\rho^2 R_0)^{1/3}$. One solution represents the boundary between the banana and outer-circulating regions, while the other corresponds to the boundary between the kidney and passing regions. As shown in Fig. 2.8, the kidney region is very narrow and then the latter solution is almost the same as the upper boundary of the banana region *b3* at $r_s > \Delta_p$. In particular, away from the magnetic axis, two solutions of Eq. (2.27) are approximated as $\xi_s \simeq q\rho/r_s \sim 0$ and $\xi_s \simeq \sqrt{2\epsilon_s}$, which give the conventional representation of the banana region.

Finally, the upper and lower boundaries of the banana region *b3* are obtained from equations for a particle which has the turning point $\dot{\theta} = 0$ at $(r, \theta) = (r_t, \pi)$. Taking $r_t = x\Delta_{ic}$ $(x \geq 1)$ and using the approximation $r_t/R_0 \ll 1$, these boundaries (r_s, ξ_s) can be given in terms of x as

$$\begin{cases} r_s = x(1 \pm x^{-3/2})\Delta_{ic}, \\ \xi_s = \left(\dfrac{q\rho}{2R_0}\right)^{1/3}\left(\pm 2x^{1/2} + \dfrac{1}{2x}\right), \end{cases} \tag{2.28}$$

where we choose $+$ $(-)$ for the upper (lower) boundary. When $x \gg 1$, these equations result in $\xi_s \simeq \pm\sqrt{2\epsilon_s}$. Applying these equations to $x < 1$, they represent the boundary E-X in Figs. 2.6 and 2.8. In Fig. 2.6, three boundaries, which are given by Eqs. (2.20), (2.26), and (2.28), respectively, converge on the point X at $r_s < 0$. This point is given by solving Eq. (2.28) for $|r_s| = r_t$ as

$$[r_s, \xi_s] = \left[-\left(\frac{q^2\rho^2 R_0}{2}\right)^{1/3}, -\left(\frac{q\rho}{4R_0}\right)^{1/3}\right], \tag{2.29}$$

and another pair to the point X at $r_s > 0$ is written as

$$[r_s, \xi_s] = \left[3\left(\frac{q^2\rho^2 R_0}{2}\right)^{1/3}, \frac{3}{2}\left(\frac{2q\rho}{R_0}\right)^{1/3}\right]. \tag{2.30}$$

Let us discuss the results of this section. As shown in Eq. (2.16), the banana region has the finite fraction $|\xi_0|$ (~ 0.16 for the parameters used in Figs. 2.2 – 2.5) on the

magnetic axis. We can see from Fig. 2.6 that a considerable fraction of particles which have been regarded as bananas are actually identified as outer-circulating particles. Within $|r_s| < 2q\rho$ ($\sim$ 2cm), nearly half of particles are circulating ones. The deviation of the banana-passing boundary from the conventional expression in Eq. (2.2) can be seen for $r < \Delta_p$ ($\sim$ 20cm). Since ξ_0 and Δ_p increases with $q\rho$, the modification on orbit classification is significant for high energy particles and in high-q configurations. It is also noted that because $\rho_e/\rho_i \propto \sqrt{m_e/m_i} \ll 1$ for the two species with the same energy, the modification on the particle orbits near the axis is more important for ions than that for electrons.

In recent approaches of extending neoclassical transport theory to the near-axis region, the main modification is to take account of potato particles in solving the transport equation. In the (r_s, ξ_s) plane, we find that any particle which has one of a pair of points (r_s, ξ_s) around the origin in the range about $|r_s| \leq (q^2\rho^2 R_0)^{1/3}$ and $|\xi_s| \leq (q\rho/R_0)^{1/3}$ has this characteristic orbit width. Therefore, potato orbits are not only banana orbits passing through near the magnetic axis but consist of many types of orbit appearing around the origin in the (r_s, ξ_s) plane in Fig. 2.6, and all of them will contribute to the neoclassical transport near the axis. Therefore, recent studies for extension of neoclassical transport theory[10, 11, 12, 13, 14] are insufficient in that they do not consider inner-circulating and kidney orbits.

As concerns Lagrangian transport theory, there are some difficulties in using the set of COM (v, ξ_s, r_s) in practice, though Zaitsev *et al.*[21] have attempted to. The position r_s jumps when a particle changes from passing to banana particle, and from inner-circulating to concave-kidney particles. Such a discontinuity is unfavorable to construct transport equations. Moreover, since there are two values of r_s for each orbit and the difference between them is large for potato particles, the transport equation in the Lagrangian representation is not simply connected to the transport phenomena in real space if z_3 is taken as r_s. Though the classification of orbit types in the (v, ξ_s, r_s) space is a useful way in itself, it does not seem to be suitable to apply to Lagrangian formulation in the region near the magnetic axis.

2.4 Classification in the $(\mathcal{E}, \mu, \langle r \rangle)$ space

In this section, the region of each orbit type in the $(\mathcal{E}, \mu, \langle r \rangle)$ space is investigated as a basis of the Lagrangian transport theory in §3.

Let us consider a transformation from Cartesian coordinate system (x_i, v_i) to $(z_i, \tilde{z}_i) =$

$(\mathcal{E}, \mu, \langle r \rangle, \theta, \zeta, \phi)$. In axisymmetric systems with drift approximation, the toroidal angle ζ and the gyrophase ϕ can be neglected, and the guiding-center position is described by the minor radius r and the poloidal angle θ. Three constants of motion are defined as

$$\mathcal{E} \equiv \frac{1}{2}mv^2 + e\Phi, \tag{2.31a}$$

$$\mu \equiv \frac{mv_\perp^2}{2B}, \tag{2.31b}$$

$$\langle r \rangle \equiv \frac{1}{\tau_b} \oint r \frac{d\theta}{\dot{\theta}}, \tag{2.31c}$$

where $v_\perp$ is the velocity perpendicular to the magnetic field lines, and the integral in Eq. (2.31c) is carried out along one poloidal circuit of an orbit. The poloidal bounce time τ_b is given by

$$\tau_b = \oint \frac{d\theta}{\dot{\theta}}. \tag{2.32}$$

We can also use the poloidal flux surface label ψ and $\langle \psi \rangle$ instead of r and $\langle r \rangle$ for a radial coordinate when it is convenient. In fact, we use $\langle \psi \rangle$ in the derivation of the Lagrangian transport equation in §3. In this section, however, we choose $\langle r \rangle$ to describe orbit properties in the COM space because of the convenience of analysis.

Note that the definition of the orbital integral is different according to orbit types. For passing orbits and kidney orbits, θ varies monotonously in time. Then the orbital integral of a function $F(r, \theta)$ along these orbits is defined as

$$\oint F(r,\theta)\frac{d\theta}{\dot{\theta}} = \sigma_\theta \int_0^{2\pi} F(r,\theta)\frac{d\theta}{\dot{\theta}}, \tag{2.33}$$

where r is a function of $(\mathcal{E}, \mu, \langle r \rangle, \theta)$ and depends on orbit types. On the other hand, as shown in §2.2, banana, outer-circulating, and inner-circulating orbits have two turning points of σ_θ at which $\dot{\theta} = 0$. Writing one of the turning points $\theta = \theta_t$ $(0 \leq \theta_t \leq \pi)$, the orbital integral is defined as

$$\oint F(r,\theta)\frac{d\theta}{\dot{\theta}} = \sum_{\sigma_\theta = \pm 1} \sigma_\theta \int_{-\theta_t}^{+\theta_t} F(r,\theta)\frac{d\theta}{\dot{\theta}} \tag{2.34}$$

for banana and outer-circulating orbits, and

$$\oint F(r,\theta)\frac{d\theta}{\dot{\theta}} = \sum_{\sigma_\theta = \pm 1} \sigma_\theta \int_{\theta_t}^{2\pi-\theta_t} F(r,\theta)\frac{d\theta}{\dot{\theta}} \tag{2.35}$$

for inner-circulating orbits. Note that the integrand F depends on the sign σ_θ through $r = r(z_i, \theta; \sigma_\theta)$ as shown in Fig. 2.9, where σ_θ (not $\sigma_\parallel$) indicates the inner or outer part

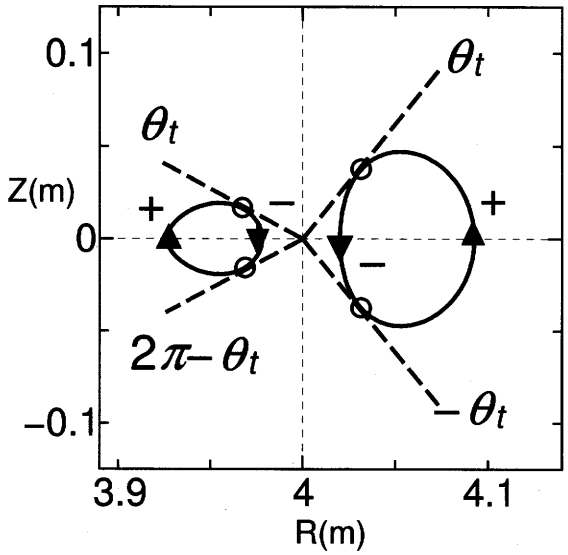

Figure 2.9: Orbital integrations along inner- and outer-circulating particle orbits. The circles and $\pm$ represent turning points and signs of σ_θ, respectively. For a given $(\mathcal{E}, \mu, \langle r \rangle)$, there are two solutions for the particle position $r(\theta)$ which are distinguished by $\sigma_\theta = \pm 1$.

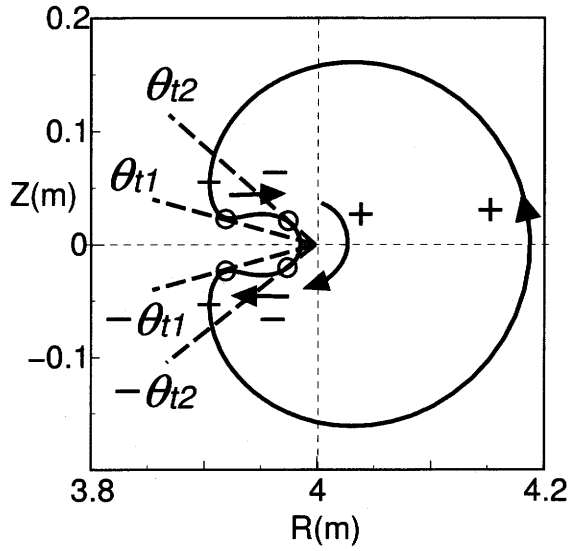

Figure 2.10: Orbital integration along a concave-kidney particle orbit. The bars represents the turning points of $\sigma_\parallel$, and other marks are used in the same meaning as in Fig. 2.6.

of a circulating (or a banana) orbit. For concave-kidney orbits, there are four turning points $\theta = \pm\theta_{t1}, \pm\theta_{t2}$ $(\pi/2 \leq \theta_{t2} \leq \theta_{t1} \leq \pi)$ at which $\dot{\theta} = 0$ as shown in Fig. 2.10. Therefore the orbital integral is defined as

$$\oint \frac{d\theta}{\dot{\theta}} = \sigma_\theta(\theta = 0) \cdot \left[\int_{-\theta_{t1}}^{\theta_{t1}} \frac{d\theta}{\dot{\theta}} + \int_{\theta_{t1}}^{\theta_{t2}} \frac{d\theta}{\dot{\theta}} + \int_{\theta_{t2}}^{2\pi-\theta_{t2}} \frac{d\theta}{\dot{\theta}} + \int_{2\pi-\theta_{t2}}^{2\pi-\theta_{t1}} \frac{d\theta}{\dot{\theta}} \right], \tag{2.36}$$

where $\sigma_\theta(\theta = 0)$ is $+1$ for ions and -1 for electrons in the present configuration.

Next, let us show the region of each orbit types in the $(\mathcal{E}, \mu, \langle r \rangle)$ space. Here, we introduce the normalized magnetic moment λ_0 as

$$\lambda_0 \equiv \frac{\mu B_0}{\mathcal{E}}. \tag{2.37}$$

In Fig. 2.11, we classify the orbit types in the $(\langle r \rangle, \lambda_0)$ plane for hydrogen ions with $\mathcal{E} = 10$keV, where the configuration is set in the same way as in §2.3. Since some parts of regions are overlapped one another in the $(\langle r \rangle, \lambda_0)$ plane, regions are shown separately in three figures. Figures 2.11(a) and (b) show regions of orbits which have

positive and negative $\sigma_{\|}$, respectively. Since banana particles take both signs of $\sigma_{\|}$, its region appears on both figures. In Fig. 2.11(c), the kidney and concave-kidney regions are shown. To compare with the classification in the (r_s, ξ_s) plane, three characteristic points E (=H), G, and X, which correspond to the orbits with the same marks in Fig. 2.6, are plotted in Fig. 2.11.

In the $(\langle r \rangle, \lambda_0)$ plane, these boundaries are obtained by a numerical method. However, in the present configuration with a constant-q profile, boundaries *l1* and *l2* in Figs. 2.11(a) and (b) can be obtained analytically. These lines correspond to the upper boundary of the outer-circulating region, and the upper boundary of the inner-circulating region which connects to the lower boundary of the banana region, respectively. From Eq. (2.20), they are written as

$$\lambda_0 = 2\left(1 \pm \frac{\langle r \rangle}{R_0}\right)\left[1 - \left(\frac{\langle r \rangle}{q\rho}\right)^2 \left(1 - \sqrt{1 - \left(\frac{q\rho}{\langle r \rangle}\right)^2}\right)\right], \tag{2.38}$$

where we choose $+$ $(-)$ for the boundary *l1* (*l2*). In the limit $\langle r \rangle \gg q\rho$, Eq. (2.38) results in $\lambda_0 = 1 \pm \langle r \rangle / R_0$ and agree with the conventional description for the banana region. Because any orbits on the boundary Eq. (2.38) are stagnated on the mid-plane $Z = 0$, their averaged position are given by $\langle r \rangle = |r_s|$ from Eq. (2.20). Then, positions of the points E (=H) is given analytically as

$$[\langle r \rangle, \lambda_0] = \left[(2q^2\rho^2 R_0)^{1/3}, 1 - \frac{9}{4}\left(\frac{q\rho}{2R_0}\right)^{2/3}\right], \tag{2.39}$$

and the point X is also given as

$$[\langle r \rangle, \lambda_0] = \left[\left(\frac{q^2\rho^2 R_0}{2}\right)^{1/3}, \left\{1 - \left(\frac{q\rho}{4R_0}\right)^{2/3}\right\} \cdot \left\{1 - \frac{1}{2^{1/3}}\left(\frac{q\rho}{R_0}\right)^{2/3}\right\}\right]. \tag{2.40}$$

To obtain the position of G, which corresponds to the outer-circulating orbit with maximum width $\Delta_{oc} = (4q^2\rho^2 R_0)^{1/3}$, we need to calculate its average position numerically. It is given by

$$\mathrm{G}: \qquad [\langle r \rangle, \lambda_0] = \left[\chi(4q^2\rho^2 R_0)^{1/3},\ 1\ \right], \tag{2.41}$$

where the numerical factor is $\chi \simeq 0.6$. We find that χ is almost independent of particle energy and q factor in the case of a constant-q profile. The dependency of regions on particle energy $\mathcal{E}$ and magnetic field configuration appears through $q\rho$ and R_0 in Eqs. (2.38) to (2.41). Then, the points E, G, and X move outward in the $\langle r \rangle$-direction for higher energy particles and in a high-q configuration such as a reversed shear configuration.

From Eqs. (2.39) and (2.41), one finds that potato particles correspond to those appearing around

$$(\langle r\rangle, \lambda_0) \sim \left((q^2\rho^2 R_0)^{1/3}, 1 \pm (q\rho/R_0)^{1/3}\right) \tag{2.42}$$

in the $(\langle r\rangle, \lambda_0)$ plane. For the convenience of notation, we introduce a typical minor radius

$$r_p = 2(2q^2\rho_{i0}^2 R_0)^{1/3}, \tag{2.43}$$

where $\rho_{i0} = m_i v_{thi}/e_i B_0$. In later, we will show that the neoclassical transport coefficients are largely modified in the central region $0 < r \lesssim r_p$ by the presence of potato orbits.

There are no particles in the region above the boundary *l1*. In particular, counter-passing and inner-circulating particles, i. e., particles with $\sigma_\parallel = -1 = \text{const}$, do not exist in the region above the boundary *l2*. Therefore, there is a limitation on the minimum value of $\langle r\rangle$ for a given $\mathcal{E}$, which is obtained from Eq. (2.38) as $\langle r\rangle \geq q\rho$. This is because any particle which passes through the magnetic axis has a finite orbit width.

Overlaps of orbit regions occur around the boundary *l2*. One can see in Figs. 2.11(a) and (c) that the upper boundary of the co-passing region *l3* enters the banana region and the gap between *l2* and *l3* corresponds to the kidney region. The kidney region also overlaps with the concave-kidney region, which is enclosed by the solid curve E-G-X in Fig. 2.11(c). It is possible that some two orbits, of which orbit topologies are different between themselves, can simultaneously have the same $\mathcal{E}$, μ and $\langle r\rangle$. The overlap of region in the $(\mathcal{E}, \mu, \langle r\rangle)$ space has not been noticed in the previous works. However, we should take account of these overlaps in the Lagrangian formulation of transport theory even if we apply it to the region away from the magnetic axis, because the overlaps between the kidney, co-passing, and banana regions still remain there. In overlapped regions, particle orbits cannot be identified only by the value $(\mathcal{E}, \mu, \langle r\rangle)$, and the criterion in Table 2.1 should be adopted to identify them.

As approaching $l2$, a banana (or a concave-kidney) orbit bifurcates into a kidney and a counter-passing (kidney and an inner-circulating) orbit as shown in Fig. 2.12. Such barely-transit particles are almost stagnated at $(r, \theta) = (\langle r\rangle, \pi)$. We call the solid-line part of $l2$ "the transition boundary" hereafter. There is the other type of stagnated particles appear on the boundary $l1$. They are outer-circulating particles stagnated at $(r, \theta) = (\langle r\rangle, 0)$ and move only in the toroidal direction. Conventionally, such particles have been regarded as banana particles in the limit $v_\parallel = 0$, but in fact stagnation occurs when $\dot{\theta}$ becomes zero on $Z = 0$ plane, and stagnated particles have finite $v_\parallel$. Note that on

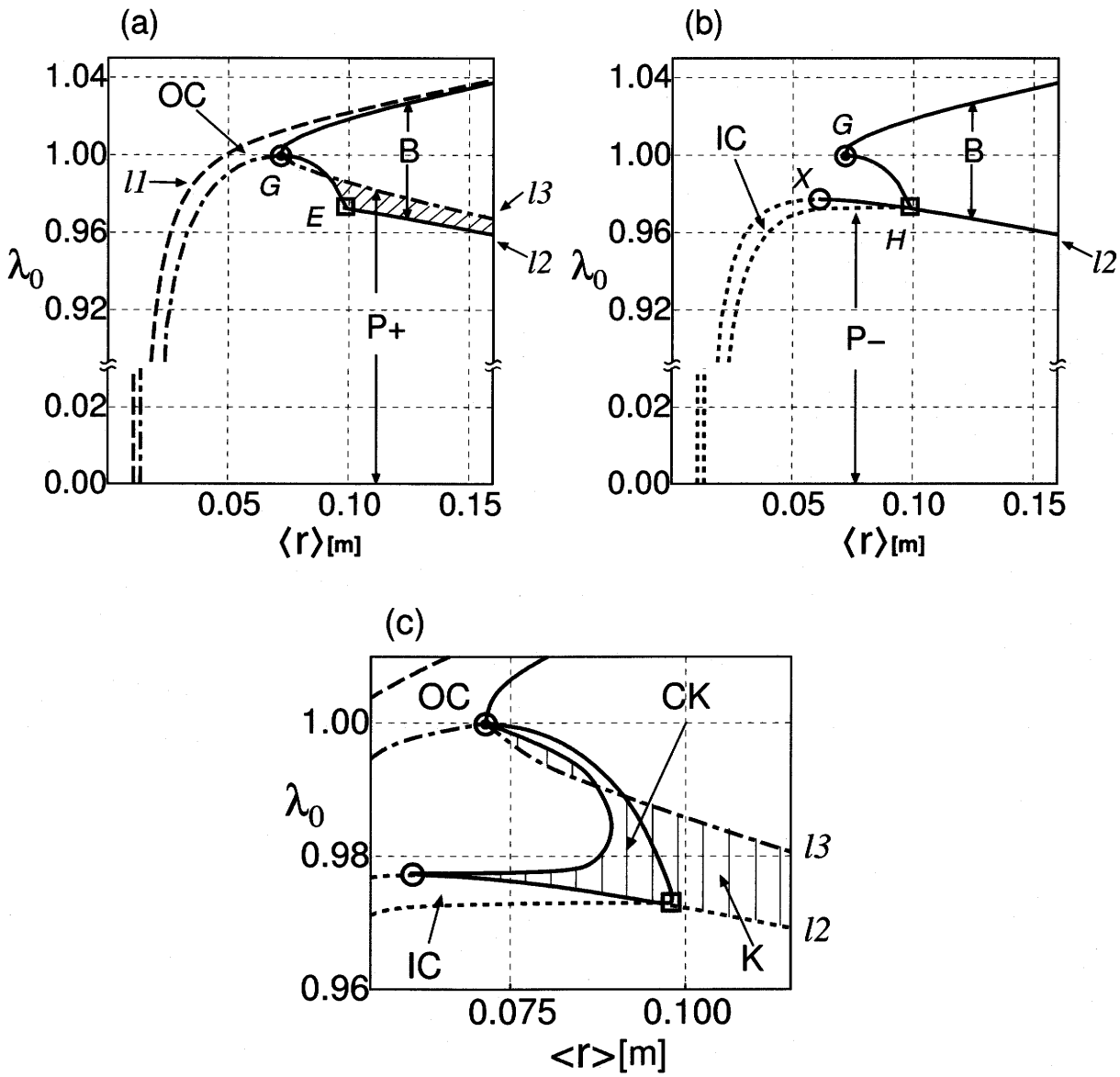

Figure 2.11: The regions and the boundaries for each type of orbit in the $(\langle r \rangle, \lambda_0)$ plane. Orbit types are abbreviated as B : banana, P+ : co-passing, P− : counter-passing, OC : outer-circulating, IC : inner-circulating, K : kidney, and CK : concave-kidney, respectively. Figures (a) and (b) show the regions for orbits with $\sigma_{\parallel} = +1$ and $\sigma_{\parallel} = -1$, respectively. In Fig. (c), the kidney region (the shaded region) and the concave-kidney region (enclosed by the boundary E-G-X) are shown. There is an overlap of orbit regions between co-passing and banana orbits in Fig. (a) (the shaded region). In Fig (c), the kidney region overlaps with the co-passing, banana, and concave-kidney regions. No particles can exist in the region above the boundary *l1*. The solid-line part of *l2* up to the X point in Fig. (b) is the transition boundary.

the dashed-line part of $l2$ (the left side from the circle mark in Fig. 2.11(b)), bifurcation of orbit types does not occur. This boundary corresponds to inner-circulating orbits with zero-width like outer-circulating particles at $l1$.

Though the overlapping of the regions is complicated, there are advantages in using the set of COM $(\mathcal{E}, \mu, \langle r \rangle)$. First, the physical meaning of the flux which is described in the Lagrangian formulation with $z_3 = \langle r \rangle$ (or $\langle \psi \rangle$) is more understandable than that with $z_3 = r_s$. In the $(\mathcal{E}, \mu, \langle r \rangle)$ space, particle flux in the $\langle r \rangle$-direction describes the change of the averaged position of particles. It is also practical to choose $\langle r \rangle$ as the position-like variable in that $\langle r \rangle$ is the most suitable value to represent the lowest-order approximation of the particle position. Second, in the collisionless limit, the change of COM is continuous in the $(\mathcal{E}, \mu, \langle r \rangle)$ space even when a particle crosses the transition boundary. This is because, as mentioned above, $\dot{\theta}$ becomes zero as a particle approaches the transition boundary $l2$, and then the averaged position of such a transit particle converges on the stagnation point $(r, \theta) = (\langle r \rangle, \pi)$. On the other hand, r_s changes discontinuously at the transition boundary as mentioned in §2.3. Last, any orbit is represented by a point in the $(\mathcal{E}, \mu, \langle r \rangle)$ space, while there are a pair of points for each orbit in the (v, ξ_s, r_s) space.

Finiteness of orbit width appears on the region of each orbit type. In the zero-width limit, banana particles exist in the range $1 - \langle \epsilon \rangle \leq \lambda_0 \leq 1 + \langle \epsilon \rangle$, where $\langle \epsilon \rangle = \langle r \rangle / R_0$. In reality, however, this simple analysis is not valid for the region $0 < \langle r \rangle \lesssim r_p$ in which potato orbits appear. Moreover, the existence of outer- and inner-circulating particles can be found only if the finiteness of orbit width is considered, and they have not been treated in the conventional neoclassical transport theory, nor in the recent studies treating the near-axis region. However, it will affect transport around the axis because some of them have large orbit width of $O(\Delta_p)$.

To illustrate the diffusion process of particle in the $(\langle r \rangle, \lambda_0)$ plane, images of particle loci in this plane are shown Figs. 2.13(a) and (b), where only the pitch-angle scattering is assumed as the effect of collisions. In Fig. 2.13(a), two ion particle loci are shown for the case away from the magnetic axis. One describes the change from co-passing (P+) to banana (B) through kidney (K), and the other is the locus from counter-passing (P−) to banana (B). Note that co-passing particles cannot change into banana particles directly. The diffusion process is more complicated for particles passing near the magnetic axis. In the $(\langle r \rangle, \lambda_0)$ plane, all particles which appear around $\langle r \rangle \sim (q^2 \rho^2 R_0)^{1/3}$ and $|\lambda_0 - 1| \sim (q\rho / R_0)^{2/3}$ (the region around the points E (=H), G, and X) have the same characteristic orbit width as potato orbits $\Delta_r \sim \langle r \rangle \sim (q^2 \rho^2 R_0)^{1/3}$. In Fig. 2.13(b),

three loci of ion particles passing through such a "potato region" are shown. A counter-passing particle (P–) enters the concave-kidney region (CK) via the inner-circulating region (IC). There are two ways for a concave-kidney particle to change into banana: (i) It changes into kidney (K) at the boundary G-X first, and then enters the banana region (B) at *l2*, or (ii) directly changes into banana by crossing the boundary G-E. It is also possible for a concave-kidney particle to enter the co-passing region (P+) via the kidney region like the locus (iii).

Concluding remarks.

The existence of potato particles will affect neoclassical transport largely. We show that potato particles consists of varied types of orbits, that is, banana, outer-circulating, inner-circulating, kidney, and concave-kidney particles. The orbital properties of potato orbits are correctly accounted only in the analysis with consideration of finiteness of orbit width of them. By Lagrangian approach, we construct a proper transport theory which can include the FOW effect of potato particles in the next chapter. In the formulation, the contribution of various types of orbit to neoclassical transport can be evaluated in a unified way.

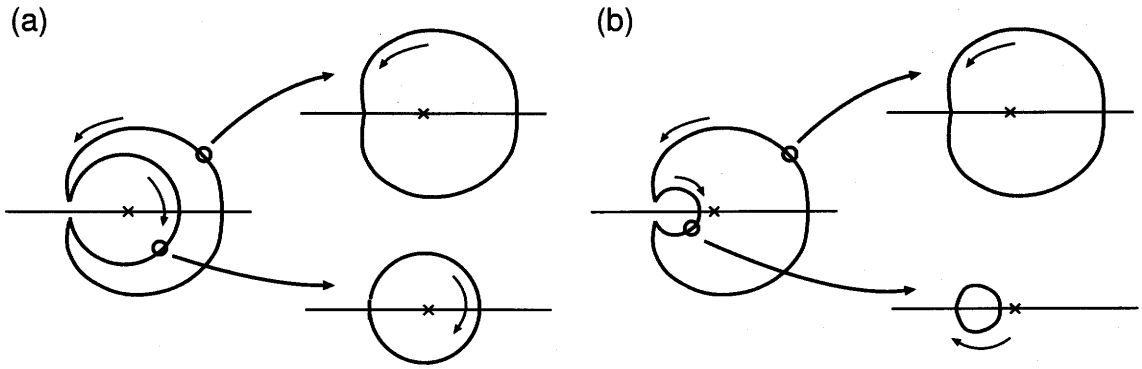

Figure 2.12: Transition in orbit types. (a) A banana orbit changes into a kidney or a counter-passing orbit according to the position on which the transition occurs. (b) Similarly, a concave-kidney changes into a kidney or an inner-circulating orbit.

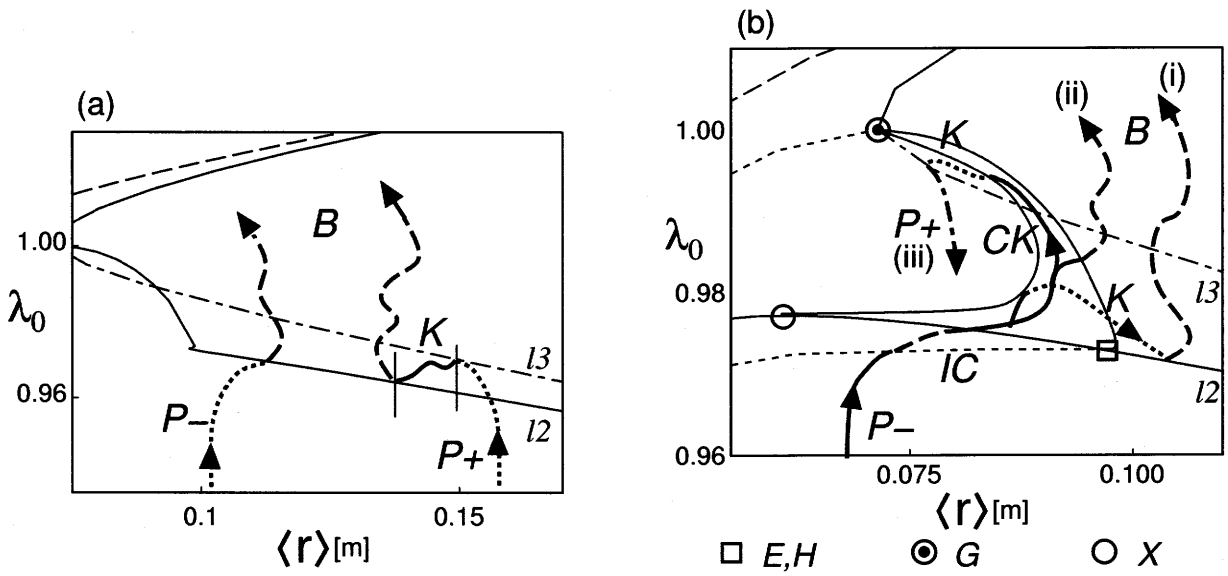

Figure 2.13: Particle loci (for case of ions) in the $(\langle r \rangle, \lambda_0)$ plane. Abbreviations of orbit types are the same as used in Figs 2.11. The change in orbit types for particles away from the magnetic axis is shown in Fig. (a), while Fig. (b) shows the change for particles passing near the axis, that is, for potato particles. In the $(\langle r \rangle, \lambda_0)$ plane, particle loci are essentially continuous on any boundaries of orbit types.

Chapter 3

Lagrangian transport theory

3.1 Introduction

As we have shown in §2, particle orbit properties are largely modified in the near-axis region from that predicted from conventional orbit analysis in the SOW limit. Since the standard neoclassical transport theory[8, 9] have been established based on the SOW limit analysis, it cannot be applied directly to the region near the magnetic axis. The main issue in modifying neoclassical transport theory is how to treat the FOW effect of potato orbits, of which width is as wide as $\Delta_r \sim (q^2\rho^2 R_0)^{1/3}$. Since the potato width is comparable to an instantaneous radial position of particle $r \sim \Delta_r$, the conventional technique to solve the drift kinetic equation is not valid, in which transport phenomena are assumed to be localized on each magnetic flux surface.

To treat neoclassical transport near the axis, one needs an ingenious method to reflect both the properties of wide-width particle orbits and information of the background field along each particle orbit in solving the drift kinetic equation. To deal with this problem, we adopt here a new approach; Lagrangian transport theory. It is based on a Lagrangian description rather than the conventional Euler description on which the standard neoclassical transport theory is based. Let us see briefly the history of progress in Lagrangian transport theory.

The innovative work on Lagrangian transport theory in magnetic confinement systems was first presented by Bernstein and Molvig in 1983[20]. They pointed out that neoclassical transport in the low-collisionality banana regime is essentially Lagrangian in nature, in which orbital properties of banana orbits with a finite width is the cause of enhancement of transport level in the direction across the flux surfaces over that of classical transport. In the Lagrangian point of view, a banana center position in an axisymmetric system is a constant of motion (COM) in the collisionless limit. The dif-

fusion process is described as a consequence of small perturbation of the banana center position by collisions. The Lagrangian formulation established by them contains the FOW effect by nature. It is because the diffusion rate of particles are evaluated with the consideration of real orbit, while in the standard Eulerian approach each particle orbit is approximated to be stuck on a magnetic surface. To demonstrate applicability of the Lagrangian formulation, they have derived the Lagrangian transport equation in a toroidally symmetric system with simple Lorentz approximation collision operator. The resultant Lagrangian transport equation have been shown to reproduce the transport coefficients obtained from the Eulerian neoclassical theory by Hinton and Hazeltine[8]. The formulation by Bernstein and Molvig has been established in a set of canonical variables of COM. Zaitsev *et al.*[21] and Wang[22] have developed the Lagrangian formulation in a non-canonical variables of COM. The sets of COM they adopted are shown in §2. Using non-canonical variables makes it convenient for numerical solution and physical interpretation than canonical variables.

An application of Lagrangian approach has been shown in analysis of resonance particle transport in weekly-asymmetric systems. Yavorskij *et al.*[30] have derived the Lagrangian formulation of ripple-trapped fast ions. Wang *et al.*[31] have applied Lagrangian approach for superbanana transport of a helical system in the ultralow collisionality regime. In these articles, the diffusion process in the COM space not only caused by collisions, but also by breaking of one of three invariants, have been discussed.

Though Lagrangian formulation has been found to be a useful tool to treat the FOW effect, there has been no practical application for a transport calculation in a case where the FOW effect really becomes important. Analytical solution for the Lagrangian transport coefficients has been obtained only in the case of the SOW limit. We show here an ingenious formulation of the Lagrangian approach in the case of near-axis region to treat the FOW effect of potato particles. The main difficulties lies in application of Lagrangian formulation are the treatment of orbit-averaged collision operator and the consideration of the region of each orbit type in the COM space (z_1, z_2, z_3). By introducing a model collision operator which is suitable to handle analytically, we derive the transport equation applicable both in the near-axis region and in the conventional SOW limit. In the next chapter, this formulation will be found to suitable for numerical calculation. By reflecting the results of the orbit analysis shown in §2, Lagrangian transport coefficients including the effect of potato particles are calculated properly.

3.2 Kinetic equation in Lagrangian formulation

3.2.1 Reduction of the kinetic equation

Consider an axisymmetric configuration. We use the magnetic coordinate system (ψ, θ, ζ), where ψ, θ, ζ are the poloidal flux, the poloidal angle, and the toroidal angle, respectively. The electromagnetic field is represented as $\mathbf{B} = I\nabla\zeta + \nabla\zeta \times \nabla\psi$ and $\mathbf{E} = -\nabla\Phi(\psi)$, where $I = RB_t$ and we assume that the field is time-independent. There are three constants of motion along a guiding-center orbit in an axisymmetric configuration : $\mathcal{E}$, μ, and P_ζ shown in Eqs. (2.7a-c). The start point of Lagrangian formulation of neoclassical transport theory is the drift kinetic equation in an Eulerian representation in the $(\mathbf{x}, \mathcal{E}, \mu)$ space,

$$\frac{\partial}{\partial t} f_a(\mathbf{x}, \mathcal{E}, \mu, t) + \dot{\mathbf{x}} \cdot \frac{\partial f_a}{\partial \mathbf{x}} = C_{ab}, \tag{3.1}$$

where $\dot{} = d/dt$, $\mathbf{x}$ is the guiding-center position and C_{ab} is the collision operator between particle species a and b. Note that Eq. (3.1) is independent of the gyrophase ϕ. We change the independent variables in Eq. (3.1) into three constants of motion in the collisionless limit (z_1, z_2, z_3), and the other three variables $(\tilde{z}_4, \tilde{z}_5, \tilde{z}_6)$. One can choose an arbitrary set of independent variables $(\mathbf{z}, \tilde{\mathbf{z}})$. In this paper, we choose $(\tilde{z}_4, \tilde{z}_5, \tilde{z}_6) = (\theta, \zeta, \phi)$ where ϕ is the gyrophase, while $z_1 = \mathcal{E}$, $z_2 = \mu$, and $z_3 = \langle\psi\rangle$ instead of P_ζ. $\langle\psi\rangle$ represents the averaged radial position of a particle orbit. The orbit average operator for any function $a(\mathbf{z}, \tilde{\mathbf{z}})$ is defined as

$$\langle a \rangle \equiv \frac{1}{4\pi^2 \tau_p} \oint \frac{d\theta}{\dot{\theta}} d\zeta d\phi \; a(\mathbf{z}, \tilde{\mathbf{z}}), \tag{3.2}$$

where

$$\tau_p \equiv \oint \frac{d\theta}{\dot{\theta}} \tag{3.3}$$

is the poloidal period of an particle orbit. Note that the integral is carried out along one poloidal circuit of the particle orbit. Note also that we can use $z_3 = \langle r \rangle$ as in §2.4 instead of $\langle\psi\rangle$ when it is convenient. By using the set of variables $(\mathbf{z}, \tilde{\mathbf{z}})$, Eq. (3.1) is transformed into

$$\frac{\partial}{\partial t} f_a(\mathbf{z}, \theta, t) + \dot{\theta} \frac{\partial f_a}{\partial \theta} = C_{ab}, \tag{3.4}$$

where the property $\partial/\partial\phi = \partial/\partial\zeta = 0$ is used.

We introduce here an ordering parameter δ_c as

$$\delta_c = \nu_c^{eff} \tau_p \ll 1, \tag{3.5}$$

where ν_c^{eff} is a typical collision frequency. This assumption corresponds to the condition that the plasma is in the low-collisionality banana regime. In Eq. (3.4), $\partial f/\partial t$ and C_{ab} are assumed to be $O(\delta_c)$ so that the variables $(\mathcal{E}, \mu, \langle\psi\rangle)$ can really be the constants of motion through the lowest order in δ_c. Expanding f_a with δ_c, the lowest part becomes

$$\dot{\theta}\frac{\partial f_0}{\partial \theta} = 0, \tag{3.6}$$

where we omit the subscript a. On the other hand, from the conservation of volume in the phase space, one has

$$\frac{1}{J_z}\frac{\partial}{\partial \mathbf{z}} \cdot \left(J_z \frac{d\mathbf{z}}{dt}\right) + \frac{1}{J_z}\frac{\partial}{\partial \tilde{\mathbf{z}}} \cdot \left(J_z \frac{d\tilde{\mathbf{z}}}{dt}\right) = 0, \tag{3.7}$$

where $J_z(\mathbf{z}, \theta)$ is the Jacobian of the transform $(\mathbf{x}, \mathbf{v}) \to (\mathbf{z}, \tilde{\mathbf{z}})$. Since $d\mathbf{z}/dt = 0$ to $O(\delta_c^0)$, one obtains

$$J_z|\dot{\theta}| = J_0(\mathcal{E}, \mu, \langle\psi\rangle), \tag{3.8}$$

$$f_0 = f_0(\mathcal{E}, \mu, \langle\psi\rangle). \tag{3.9}$$

Next, by using Eq. (3.7), $O(\delta_c^1)$ part of Eq. (3.4) can be written as

$$\frac{\partial}{\partial t} f_0(\mathbf{z}, t) + \frac{1}{J_z}\frac{\partial}{\partial \theta}\left(J_z \frac{d\theta}{dt} f_1\right) = \frac{1}{J_z}\frac{\partial}{\partial \mathbf{z}} \cdot \left(J_z \frac{\partial \mathbf{z}}{\partial \mathbf{v}} \cdot \mathbf{\Gamma}(f_0)\right), \tag{3.10}$$

where the right hand side is derived from the fact that the collision term can be written in the divergence form in the velocity space $C(f) = \nabla_{\mathbf{v}} \cdot \mathbf{\Gamma}(f)$. The last procedure is to take the orbit average of Eq. (3.10). It yields

$$\frac{\partial \bar{f}}{\partial t} = \frac{1}{J_c}\frac{\partial}{\partial \mathbf{z}} \cdot \left(J_c \left\langle \frac{\partial \mathbf{z}}{\partial \mathbf{v}} \cdot \mathbf{\Gamma}(\bar{f}) \right\rangle\right) = \bar{C}, \tag{3.11}$$

where $\bar{f} = f_0$ is used to emphasize that $\bar{f}$ is a function of $(\mathcal{E}, \mu, \langle\psi\rangle, t)$, and

$$J_c(\mathcal{E}, \mu, \langle\psi\rangle) \equiv 4\pi^2 J_0 \tau_p \tag{3.12}$$

is the Jacobian in the $(\mathcal{E}, \mu, \langle\psi\rangle)$ space. The collision term is also averaged over a particle orbit. Thus we obtain a reduced drift-kinetic equation in the $(\mathcal{E}, \mu, \langle\psi\rangle)$ space.

3.2.2 Jacobian

Here, we derive the explicit form of the Jacobian J_c defined in Eq. (3.12). First, consider the transform from Cartesian coordinate system $(\mathbf{x}, \mathbf{v})$ to the guiding-center variables $(\psi, \theta, \zeta, \mathcal{E}, \mu, \phi)$. The Jacobian of the transform is[32]

$$J = \frac{1}{(\mathbf{B} \cdot \nabla\theta)} \cdot \frac{B_*}{m^2|v_\parallel|}, \tag{3.13}$$

where $B_* = B[1 + (v_\parallel/\Omega)\mathbf{b}\cdot\nabla\times\mathbf{b}]$. By changing ψ to its orbit averaged value $\langle\psi\rangle$, we obtain the set of variables $(\mathbf{z}, \tilde{\mathbf{z}}) = (\mathcal{E}, \mu, \langle\psi\rangle, \theta, \zeta, \phi)$. Therefore, the Jacobian J_z can be written as $J_z = J|\partial\psi/\partial\langle\psi\rangle|$. To determine J_z, we use the conservation of P_ζ. Taking orbit average of both sides of Eq. (2.7c), it becomes

$$\psi - \frac{I}{\Omega}v_\parallel = \langle\psi\rangle - \left\langle\frac{I}{\Omega}v_\parallel\right\rangle. \tag{3.14}$$

Differentiating both sides by $\langle\psi\rangle$, we have

$$\left[1 - \frac{\partial}{\partial\psi}\left(\frac{I}{\Omega}v_\parallel\right)\right]\frac{\partial\,\psi}{\partial\langle\psi\rangle} = 1 - \frac{\partial}{\partial\langle\psi\rangle}\left\langle\frac{I}{\Omega}v_\parallel\right\rangle. \tag{3.15}$$

Note that all partial derivatives in Eq. (3.15) are taken with $\mathcal{E}$, μ, and θ being kept constant. Next, by using the equation of guiding-center motion[32], one obtains

$$\dot{\theta} = \mathbf{v}\cdot\nabla\theta = \frac{v_\parallel\mathbf{B}\cdot\nabla\theta}{B_*}\left[1 - \frac{\partial}{\partial\psi}\left(\frac{I}{\Omega}v_\parallel\right)\right]. \tag{3.16}$$

Then, combining Eqs. (3.13), (3.15) and (3.16) yields

$$J_z = \frac{1}{m^2|\dot{\theta}|}|1 - \delta_*|, \tag{3.17}$$

where

$$\delta_* \equiv \frac{\partial}{\partial\langle\psi\rangle}\left\langle\frac{I}{\Omega}v_\parallel\right\rangle. \tag{3.18}$$

Thus one can confirm that $J_z|\dot{\theta}| = J_0$ in Eq. (3.8) is independent of θ. Finally, combining Eqs. (3.12) and (3.17), we obtain the Jacobian in the $(\mathcal{E}, \mu, \langle\psi\rangle)$ space

$$J_c = \frac{4\pi^2}{m^2}\tau_p|1 - \delta_*|. \tag{3.19}$$

In a numerical calculation, the poloidal period τ_p can easily be determined. As concerns δ_*, it should be noted that, from Eq. (3.14),

$$\left\langle\frac{I}{\Omega}v_\parallel\right\rangle = \left.\frac{Iv_\parallel}{\Omega}\right|_{(\langle\psi\rangle,\theta^*)}, \tag{3.20}$$

where $(\psi, \theta) = (\langle\psi\rangle, \theta^*)$ is the position at which a particle crosses its averaged flux surface $\psi = \langle\psi\rangle$. We call it "the averaging point" of an orbit. Then, Eq. (3.18) is interpreted as

$$\delta_* = \left(\frac{\partial}{\partial\psi} + \frac{\partial\theta^*}{\partial\langle\psi\rangle}\frac{\partial}{\partial\theta}\right)\left.\frac{Iv_\parallel}{\Omega}\right|_{(\langle\psi\rangle,\theta^*)}, \tag{3.21}$$

where $\partial\theta^*/\partial\langle\psi\rangle$ represents the displacement of the averaging point. Fortunately, it can be estimated that $1 - \delta_* \simeq 1$ for almost all particles as shown in Appendix A.

Though we retain the term $1-\delta_*$ in the derivation of transport equation hereafter, it is approximated to be unity in the numerical calculations.

An important property of J_c arises from the factor τ_p for particles which are stagnated on $Z=0$ plane. Remember that there are two types of stagnated orbits. One type is the outer-circulating orbit stagnated at $(\psi,\theta)=(\langle\psi\rangle,0)$ (on the $l1$ boundary in Fig. 2.11(a)), and the other is stagnated orbit at $(\psi,\theta)=(\langle\psi\rangle,\pi)$ (on the transition boundary $l2$ in Fig. 2.11(b)). Approaching the $l1$ boundary, orbits resemble a pendulum motion in the Z direction with a infinitesimal oscillation. Therefore, τ_p remains finite on $l1$. On the other hand, τ_p goes infinity when approaching the transition boundary. Then, we have

$$\lim_{\mu\to l1} J_c = \text{finite}, \tag{3.22a}$$

$$\lim_{\mu\to l2} J_c = \infty. \tag{3.22b}$$

We have shown that, in the $(\mathcal{E},\mu,\langle\psi\rangle)$ space, there are some overlaps in regions of orbit types. Then, $J_c(\mathbf{z})$ and $\bar{f}(\mathbf{z})$ are generally multi-valued functions of $\mathbf{z}$ depending on the orbit types. We introduce the sign σ_t to indicate the orbit type of each particle. The notation $J_c(\mathbf{z})$ and $\bar{f}(\mathbf{z})$ implicitly mean that they also depend on σ_t; $J_c=J_c(\mathbf{z};\sigma_t)$, etc.

3.2.3 Collision operator

To obtain transport equations in the $(\mathcal{E},\mu,\langle\psi\rangle)$ space, we need to evaluate the change rate of COM by collisions. First, consider the collision term in Eulerian representation[33]

$$C_{ab}=K_{ab}\frac{\partial}{\partial\mathbf{v}}\cdot\int d^3v'\mathsf{U}(\mathbf{v}-\mathbf{v}')\cdot\left[\frac{\partial f_a(\mathbf{v})}{\partial\mathbf{v}}f_b(\mathbf{v}')-\frac{m_a}{m_b}f_a(\mathbf{v})\frac{\partial f_b(\mathbf{v}')}{\partial\mathbf{v}'}\right], \tag{3.23}$$

where

$$\begin{aligned}\mathsf{U}(\mathbf{v}) &= \frac{\mathsf{I}}{|\mathbf{v}|}-\frac{\mathbf{v}\mathbf{v}}{|\mathbf{v}|^3},\\ K_{ab} &= \frac{e_a^2e_b^2\ln\Lambda}{8\pi\epsilon_0^2m_a^2}.\end{aligned}$$

Substituting Eq. (3.23) into the averaging operator Eq. (3.2), we obtain the exact description of the orbit-averaged collision term[22]

$$\bar{C}_{ab}=\frac{1}{J_c}\frac{\partial}{\partial\mathbf{z}}\cdot\left[J_c\left(\mathbf{A}\bar{f}_a(\mathbf{z})+\mathsf{D}\cdot\frac{\partial}{\partial\mathbf{z}}\bar{f}_a(\mathbf{z})\right)\right], \tag{3.24}$$

where

$$\mathbf{A} = -K_{ab}\frac{m_a}{m_b}\left\langle \frac{\partial \mathbf{z}}{\partial \mathbf{v}} \cdot \int d^3\mathbf{v}'\mathsf{U}(\mathbf{v}-\mathbf{v}') \cdot \frac{\partial}{\partial \mathbf{v}'}\bar{f}_b(\mathbf{z}')\right\rangle, \tag{3.25a}$$

$$\mathsf{D} = K_{ab}\left\langle \frac{\partial \mathbf{z}}{\partial \mathbf{v}} \cdot \int d^3\mathbf{v}'\bar{f}_b(\mathbf{z}')\mathsf{U}(\mathbf{v}-\mathbf{v}') \cdot \frac{\partial \mathbf{z}}{\partial \mathbf{v}}\right\rangle, \tag{3.25b}$$

Note that $\mathbf{z}'$ in Eq. (3.25) is a functional depending on θ

$$\mathbf{z}' = (\mathcal{E}', \mu', \langle\psi\rangle') = (\mathcal{E}', \mu', \langle\psi\rangle + \tilde{\psi}'(\mathbf{z}, \mathcal{E}', \mu', \theta)),$$

where $\tilde{\psi}'$ arises from the finiteness of particle orbit width. In this sense, the averaged collision term Eq. (3.24) has a non-locality. Moreover, since Eq. (3.24) is a integro-differential function, it is not suitable to solve analytically or calculate numerically. Cohen *et al.*[34] have examined a general procedure to use the averaged collision operator in a form like Eq. (3.24). In this approach, however, it has been shown that the implicit part of transport coefficients, which are associated with the perturbed distribution function g_k(defined later in Eq. (3.53)), can be solved only approximately by using a variational principle. Then, we need an approximated collision operator in the Lagrangian formulation which is suitable to solve the perturbed distribution function g_k easily.

From here on, we consider only the ion transport because the FOW effect near the magnetic axis is important for ions. We neglect the ion-electron term C_{ie} since it is smaller than the ion-ion term C_{ii} by a factor $\sqrt{m_e/m_i}$. An easy approximation for collision term is the Lorentz operator, which had been used in the fundamental study of the Lagrangian formulation by Bernstein and Molvig[20], but it does not conserve momentum. It is well-known that the momentum conservation property of like-species collisions plays an important role in transport theory. Therefore, we use here a model collision operator which conserves the parallel momentum locally so that the transport equation may reproduce the result obtained from the Eulerian formulation in the SOW limit.

The model collision operator is given in the following form [35]

$$C_i(f_i) = \frac{\nu_i}{2}\frac{\partial}{\partial \mathbf{v}} \cdot (v^2\mathsf{I} - \mathbf{v}\mathbf{v}) \cdot \frac{\partial}{\partial \mathbf{v}} f_i + \nu_i \frac{m_i v_\parallel u_{i\parallel}}{T_i} f_{iM}, \tag{3.26}$$

where $u_{i\parallel}$ is a functional of f_i, and f_{iM} is a local Maxwellian. Collision frequency ν_i is defined as

$$\nu_i = \frac{3\sqrt{\pi}}{4\tau_i c_i^3} y(c_i), \tag{3.27}$$

where $c_i = v/v_{thi}$ and

$$\tau_i^{-1} = \frac{n_i Z_i^4 e^4 \ln \Lambda}{3\pi^{3/2}\epsilon_0^2 m_i^2 v_{thi}^3}, \tag{3.28a}$$

$$y(c) = \left(1 - \frac{1}{2c^2}\right)\Psi(c) + \frac{1}{2c}\Psi'(c), \tag{3.28b}$$

$$\Psi(c) = \frac{2}{\sqrt{\pi}}\int_0^c dx e^{-x^2}. \tag{3.28c}$$

Here, $u_{i\|}$ is determined in order to conserve the parallel momentum

$$\int d^3v v_\| C_i(f_i) = 0. \tag{3.29}$$

Then, substituting Eq. (3.26) into this equation yields

$$u_{i\|} = \frac{\tau_i}{2n_i\mathcal{K}_1}\int d^3v \nu_i v_\| f_i, \tag{3.30}$$

where

$$\mathcal{K}_n \equiv \int_0^\infty dc e^{-c^2} c^n y(c). \tag{3.31}$$

It is convenient to rewrite Eq. (3.26) in the divergence form, by noting $\partial f_M/\partial \mathbf{v} = -(m\mathbf{v}/T)f_M$,

$$C_i(f_i) = \frac{\nu_i}{2}\frac{\partial}{\partial \mathbf{v}} \cdot \left[\left(\mathsf{V}(\mathbf{v}) \cdot \frac{\partial}{\partial \mathbf{v}} f_i - \frac{m_i u_{i\|}}{T_i}\mathbf{w} f_{iM}\right)\right], \tag{3.32}$$

where $\mathsf{V}(\mathbf{v}) = v^2\mathsf{I} - \mathbf{v}\mathbf{v}$ and $\mathbf{w} = v^2\mathbf{b} - v_\|\mathbf{v}$. Since $\mathsf{V}\cdot\mathbf{v} = 0$ and $\mathbf{w}\cdot\mathbf{v} = 0$, the model collision operator Eq. (3.32) also conserves particle number and energy.

Finally, by taking the orbit average of Eq. (3.32), we obtain the orbit-averaged model collision operator

$$\bar{C}_i(\bar{f}_i) = \frac{1}{J_c}\frac{\partial}{\partial \mathbf{z}} \cdot J_c \frac{\nu_i(c_i, \langle\psi\rangle)}{2}\left[\left\langle \frac{\partial \mathbf{z}}{\partial \mathbf{v}} \cdot \mathsf{V} \cdot \frac{\partial \mathbf{z}}{\partial \mathbf{v}}\right\rangle \frac{\partial \bar{f}_i}{\partial \mathbf{z}} - \left\langle \frac{m_i u_{i\|}}{T_i}\frac{\partial \mathbf{z}}{\partial \mathbf{v}} \cdot \mathbf{w} f_{iM}\right\rangle\right]. \tag{3.33}$$

We neglect here the variation of ν_i along an ion orbit because, though typical ion orbit width becomes as large as $\Delta_r \sim r_p$ there, experiments show that density and temperature profiles near the axis are flat. Note also that we neglect the variation of v along a particle orbit in averaged collision terms. To ensure this approximation, it it assumed that

$$\mathcal{E} \gg \left|\Delta_r e_i \frac{d\Phi}{d\langle r\rangle}\right|, \tag{3.34}$$

where $e_i = Z_i e$, and v is evaluated as

$$v = \sqrt{\frac{2}{m_i}[\mathcal{E} - e_i\Phi(\langle\psi\rangle)]}. \tag{3.35}$$

In Eq. (3.33), we need to evaluate $\partial \mathbf{z}/\partial \mathbf{v}$. It is immediately shown that

$$\begin{aligned}\frac{\partial \mathcal{E}}{\partial \mathbf{v}} &= m\mathbf{v}, \\ \frac{\partial \mu}{\partial \mathbf{v}} &= \frac{m\mathbf{v}_\perp}{B}.\end{aligned}$$

We also need the expression of $\partial\langle\psi\rangle/\partial\mathbf{v}$. This factor is important in the Lagrangian formulation, because it measures the rate of excursion in average radial position of a particle by a scattering in the velocity space. $\partial\langle\psi\rangle/\partial\mathbf{v}$ can be obtained by taking partial derivative on both sides of Eq. (3.14). It gives

$$\begin{aligned}\frac{\partial\langle\psi\rangle}{\partial\mathbf{v}} &= -\frac{I}{\Omega}\mathbf{b} + \frac{\partial}{\partial\mathbf{v}}\left\langle\frac{Iv_\parallel}{\Omega}\right\rangle \\ &= -\frac{I}{\Omega}\mathbf{b} + \left(\frac{\partial\mathcal{E}}{\partial\mathbf{v}}\frac{\partial}{\partial\mathcal{E}} + \frac{\partial\mu}{\partial\mathbf{v}}\frac{\partial}{\partial\mu} + \frac{\partial\langle\psi\rangle}{\partial\mathbf{v}}\frac{\partial}{\partial\langle\psi\rangle}\right)\left\langle\frac{Iv_\parallel}{\Omega}\right\rangle. \qquad (3.36)\end{aligned}$$

In a previous work[22], this factor is treated approximately as a step-function

$$\begin{cases}\dfrac{\partial\langle\psi\rangle}{\partial\mathbf{v}} = -\dfrac{I}{\Omega}\mathbf{b} & \text{(Banana)}, \\ \dfrac{\partial\langle\psi\rangle}{\partial\mathbf{v}} = 0 & \text{(Passing)},\end{cases} \qquad (3.37)$$

in the SOW limit. However, the estimation above needs some explanations. Note that $\partial\langle\psi\rangle/\partial\mathbf{v}$ can be decomposed as $a_1\mathbf{v} + a_2\mathbf{b}$. Since $\mathsf{V}\cdot\mathbf{v} = \mathbf{w}\cdot\mathbf{v} = 0$, we need to retain only the $\mathbf{b}$ component of the derivative. Noting Eqs. (3.18) and (3.20), we obtain

$$(1-\delta_*)\frac{\partial\langle\psi\rangle}{\partial\mathbf{v}} = -\frac{I}{\Omega}(1-\Delta_c)\mathbf{b}, \qquad (3.38)$$

where

$$\Delta_c = -\frac{ev_\parallel}{I}\frac{\partial}{\partial\mu}\left\langle\frac{Iv_\parallel}{\Omega}\right\rangle. \qquad (3.39)$$

For the convenience of notation, we introduce a factor γ as follows

$$\frac{\partial\langle\psi\rangle}{\partial\mathbf{v}} = -\gamma(\mathbf{z},\theta;\sigma_t)\frac{I}{\Omega}\mathbf{b}. \qquad (3.40)$$

Later, it is shown that we do not need the explicit form of Δ_c to calculate transport coefficients as pointed out in Ref. [20], and the estimation in Eq. (3.37) works well in the SOW limit.

3.3 Neoclassical transport equation in Lagrangian formulation

3.3.1 Derivation of transport equation

We now expand the reduced drift kinetic equation (3.11) by a small ordering parameter

$$\delta_b \equiv \frac{\Delta_r}{L} \ll 1, \tag{3.41}$$

where Δ_r is a typical orbit width and L is a typical gradient scale length of plasma pressure. Though Δ_r for ions becomes larger in the near-axis region, the condition (3.41) can be satisfied since L also becomes large there.

The orderings we put in Eq. (3.11) is as follows. $\partial \bar{f}/\partial t$ is assumed to be $O(\delta_b^2)$ as is often called "transport-ordering". For the parallel flow, we put a plausible ordering that $u_{i\parallel}/v_{thi} \sim O(\delta_b)$. Concerning partial derivatives $\partial/\partial \mathbf{z}$, $\partial/\partial \mathcal{E}$ and $\partial/\partial \mu$ are treated as $O(\delta_b^0)$, while $\partial/\partial\langle\psi\rangle \sim O(\delta_b^1)$. Collision operator is then expanded in δ_b as $\bar{C} = \bar{C}^{(0)} + \delta_b \bar{C}^{(1)} + \delta_b^2 \bar{C}^{(2)} \cdots$. With the expansion $\bar{f} = \bar{f}_0 + \delta_b \bar{f}_1 + \delta_b^2 \bar{f}_2 \cdots$, the $O(\delta_b^0)$ part of Eq. (3.11) for ion becomes

$$\bar{C}_i^{(0)}(\bar{f}_{i0}) = \frac{1}{J_c}\frac{\partial}{\partial \mu}\frac{J_c \nu_i}{2}\left[\left\langle \frac{\partial \mu}{\partial \mathbf{v}} \cdot \mathsf{V} \cdot \frac{\partial \mu}{\partial \mathbf{v}} \right\rangle \cdot \frac{\partial \bar{f}_{i0}}{\partial \mu}\right] = 0. \tag{3.42}$$

Because $(\partial \mathcal{E}/\partial \mathbf{v}) \cdot \mathsf{V} = 0$, only μ-derivative appears in Eq. (3.42). Then, any distribution function $\bar{f}_{i0}$ independent of μ is the solution of this equation. However, we adopt here the averaged collision operator of its exact form shown in Eq. (3.24) for $\bar{C}_i^{(0)}$. The details of calculation is shown in Appendix B. The solution of $\bar{f}_{i0}$ becomes the local Maxwellian

$$\bar{f}_{i0} = \bar{n}_i \left(\frac{m_i}{2\pi T_i}\right)^{3/2} \exp\left[-\frac{\mathcal{E} - e_i \Phi}{T_i}\right], \tag{3.43}$$

where $\bar{n}_i$, T_i and Φ are defined as functions of $\langle\psi\rangle$.

The definition of $\bar{n}_i$ is not equal to the flux-surface averaged density $n_i(\psi)$ used in the Eulerian transport theory. First, consider the particle number per unit $\langle\psi\rangle$ as follows

$$\mathcal{N}_i(\langle\psi\rangle) = \sum_{\sigma_t} \int d\mathcal{E} d\mu J_c \bar{f}_{i0}(\mathcal{E}, \mu, \langle\psi\rangle; \sigma_t). \tag{3.44}$$

Then, $\bar{n}_i(\langle\psi\rangle)$ is defined as

$$\bar{n}_i = \left.\frac{d\psi}{dV}\right|_{\psi=\langle\psi\rangle} \mathcal{N}_i(\langle\psi\rangle)\lambda_n(\langle\psi\rangle), \tag{3.45}$$

where V is the volume enclosed by a $\psi = const$ surface, and the numerical factor λ_n is given by

$$\lambda_n(\langle\psi\rangle) = \frac{dV}{d\psi}\left(\frac{2\pi T_i}{m_i}\right)^{3/2} \Bigg/ \sum_{\sigma_t}\int d\mathcal{E}d\mu J_c \exp\left[-\frac{\mathcal{E}-e_i\Phi}{T_i}\right] \tag{3.46}$$

If $\langle\psi\rangle$ is away from the magnetic axis and the orbit width is narrow, $\lambda_n \to 1$ and then one can easily find that $\bar{n}_i(\langle\psi\rangle) \simeq n_i(\psi)$ there. When approaching $\langle\psi\rangle \to 0$, however, λ_n becomes large because the integral region in the $(\mathcal{E},\mu)$ plane is small there. Note that $\mathcal{N}_i$ is nearly proportional to λ_n^{-1} near the axis, assuming that the density profile in the real space is flat in the range $r < r_p$. This assumption is valid when considering the core region with ITB. Then, it is a simple and plausible assumption that $\bar{n}_i(\langle\psi\rangle) \simeq n_i(\psi = \langle\psi\rangle)$, even in the near-axis region. We check the validity of this assumption in Appendix E.

Before proceeding to the $O(\delta_b^1)$ equation, let us consider the order expansion of the momentum-restoring term in Eq. (3.33). Since $u_{i\|}$ and f_{iM} vary along a particle orbit, we expand it as

$$\left.\frac{u_{i\|}f_{iM}}{T_i}\right|_{(\psi,\theta,\mathbf{v})} \equiv \frac{I}{B}\frac{B_0\overline{u_i}_\|}{I_0T_i(\langle\psi\rangle)}\bar{f}_{i0}(\mathbf{z}) + \Delta_\|(\mathbf{z},\theta)\bar{f}_{i0}(\mathbf{z}). \tag{3.47}$$

Here, $\overline{u_i}_\|(\langle\psi\rangle)$ is the lowest-order approximation of $u_{i\|}$ chosen properly so that $\Delta_\|$ becomes $O(\delta_b^2)$. The reason why we expand it in this way is an analogy with the fact that, in Eulerian representation, the neoclassical flux in the radial direction is proportional not to $\langle u_{i\|}\rangle_\psi$, but to $\langle Iu_{i\|}/B\rangle_\psi$ known as the flux-friction relation[9], where $\langle\cdots\rangle_\psi$ means the flux-surface average. Then, substituting Eq. (3.47) into Eq. (3.33) yields

$$\begin{aligned}\bar{C}_i(\bar{f}_i) &= \frac{1}{J_c}\frac{\partial}{\partial\mathbf{z}}\cdot\frac{J_c\nu_i}{2}\left[\left\langle\frac{\partial\mathbf{z}}{\partial\mathbf{v}}\cdot\mathsf{V}\cdot\frac{\partial\mathbf{z}}{\partial\mathbf{v}}\right\rangle\frac{\partial\bar{f}_i}{\partial\mathbf{z}} - \frac{m_iB_0\overline{u_i}_\|}{I_0T_i}\left\langle\frac{I}{B}\frac{\partial\mathbf{z}}{\partial\mathbf{v}}\cdot\mathbf{w}\right\rangle\bar{f}_{i0}\right.\\ &\qquad\left. -m_i\left\langle\frac{\partial\mathbf{z}}{\partial\mathbf{v}}\cdot\mathbf{w}\Delta_\|\right\rangle\bar{f}_{i0}\right].\end{aligned} \tag{3.48}$$

Now consider the $O(\delta_b^1)$ equation of the reduced drift kinetic equation $\bar{C}_i^{(0)}(\bar{f}_{i1}) = -\bar{C}_i^{(1)}(\bar{f}_{i0})$, or written it down explicitly,

$$\begin{aligned}\frac{\nu_i}{J_c}\frac{\partial}{\partial\mu}\left[J_c\mu\left\langle\frac{m_iv_\|^2}{B}\right\rangle\frac{\partial\bar{f}_{i1}}{\partial\mu}\right] &= -\frac{\nu_i}{J_c}\frac{\partial}{\partial\mu}J_c\mu\left[\left\langle\frac{I\gamma}{\Omega_i}v_\|\right\rangle\frac{\partial\bar{f}_{i0}}{\partial\langle\psi\rangle}\right.\\ &\qquad\left. +\frac{m_i\Omega_{i0}\overline{u_i}_\|}{I_0T_i}\left\langle\frac{Iv_\|}{\Omega_i}\right\rangle\bar{f}_{i0}\right].\end{aligned} \tag{3.49}$$

To solve Eq. (3.49) for $\bar{f}_{i1}$, it is rewritten in terms of driving forces F_k as

$$\bar{C}_i^{(0)}(\bar{f}_{i1}) = \frac{\bar{f}_{i0}}{J_c}\sum_{k=1}^{3}F_k\frac{\partial\alpha_k}{\partial\mu}, \tag{3.50}$$

where

$$F_1 = \frac{d\ln\bar{n}_i}{d\langle\psi\rangle} + \frac{e_i}{T_i}\frac{d\Phi}{d\langle\psi\rangle}, \tag{3.51a}$$

$$F_2 = \frac{d\ln T_i}{d\langle\psi\rangle}, \tag{3.51b}$$

$$F_3 = \frac{m_i\Omega_{i0}\overline{u_{i\|}}}{I_0 T_i}, \tag{3.51c}$$

and

$$\alpha_1 = -J_c\nu_i\mu\left\langle\frac{I\gamma}{\Omega_i}v_\|\right\rangle, \tag{3.52a}$$

$$\alpha_2 = -\left(c_i^2 - \frac{3}{2}\right)J_c\nu_i\mu\left\langle\frac{I\gamma}{\Omega_i}v_\|\right\rangle, \tag{3.52b}$$

$$\alpha_3 = -J_c\nu_i\mu\left\langle\frac{Iv_\|}{\Omega_i}\right\rangle. \tag{3.52c}$$

Introducing the perturbed distribution function $g_k(\mathcal{E},\mu,\langle\psi\rangle)$ which satisfies

$$\bar{C}_i^{(0)}(g_k) = \frac{\bar{f}_{i0}}{J_c}\frac{\partial\alpha_k}{\partial\mu}, \tag{3.53}$$

$\bar{f}_{i1}$ can be expressed as

$$\bar{f}_{i1} = \sum_{k=1}^{3} g_k F_k. \tag{3.54}$$

Thus the first order equation is found to have a similar form to that by Bernstein *et al.*[20], though we successfully include the momentum-restoring term by introducing an additional driving force F_3.

Next, consider $O(\delta_b^2)$ part of the reduced kinetic equation

$$\begin{aligned}
&\frac{\partial\bar{f}_{i0}}{\partial t} - \left[\bar{C}_i^{(2)}(\bar{f}_{i0}) + \bar{C}_i^{(1)}(\bar{f}_{i1}) + \bar{C}_i^{(0)}(\bar{f}_{i2})\right] = 0 \\
\Leftrightarrow\ &\frac{\partial\bar{f}_{i0}}{\partial t} - \frac{1}{J_c}\frac{\partial}{\partial\langle\psi\rangle}J_c\nu_i\frac{\mu}{e_i}\left[\left\langle\frac{I^2}{\Omega_i}\gamma^2\right\rangle\frac{\partial\bar{f}_{i0}}{\partial\langle\psi\rangle} + \frac{m_i\Omega_{i0}\overline{u_{i\|}}}{I_0T_i}\left\langle\frac{I^2\gamma}{\Omega_i}\right\rangle\bar{f}_{i0}\right. \\
&\quad + \left.\left\langle\frac{I\gamma}{\Omega_i}v_\|\right\rangle e_i\frac{\partial\bar{f}_{i1}}{\partial\mu}\right] - \frac{1}{J_c}\frac{\partial}{\partial\mu}J_c\nu_i\mu\left[\left\langle\frac{m_i}{B}v_\|^2\right\rangle\frac{\partial\bar{f}_{i2}}{\partial\mu}\right. \\
&\quad + \left.\left\langle\frac{I\gamma}{\Omega_i}v_\|\right\rangle\frac{\partial\bar{f}_{i1}}{\partial\langle\psi\rangle} + m_i\left\langle v_\|\Delta_\|\right\rangle\bar{f}_{i0}\right] = 0.
\end{aligned} \tag{3.55}$$

By taking a moment with $\mathcal{E}$ and μ, we obtain the continuity equation in the $\langle\psi\rangle$ direction

$$\frac{\partial}{\partial t}\mathcal{N}_i + \frac{\partial}{\partial\langle\psi\rangle}J_1^i = 0, \tag{3.56}$$

where the ion particle flux J_1^i is given as

$$J_1^i = \sum_{k=1}^{3} (S_{1k}^{ex} + S_{1k}^{im}) F_k. \tag{3.57}$$

In deriving Eq. (3.56), the boundary condition in the $(\mathcal{E}, \mu)$ plane explained in Appendix C is used. An important feature is that the transport coefficients are separated into the explicit and implicit parts, S_{jk}^{ex} and S_{jk}^{im}, respectively. They are given as follows

$$S_{11}^{ex} = -\left\{ \nu_i \frac{\mu}{e_i} \left\langle \frac{I^2}{\Omega_i} \gamma^2 \right\rangle, \bar{f}_{i0} \right\}, \tag{3.58a}$$

$$S_{12}^{ex} = -\left\{ \nu_i \frac{\mu}{e_i} \left\langle \frac{I^2}{\Omega_i} \gamma^2 \right\rangle, \left(c_i^2 - \frac{3}{2} \right) \bar{f}_{i0} \right\}, \tag{3.58b}$$

$$S_{13}^{ex} = -\left\{ \nu_i \frac{\mu}{e_i} \left\langle \frac{I^2 \gamma}{\Omega_i} \right\rangle, \bar{f}_{i0} \right\}, \tag{3.58c}$$

$$S_{1k}^{im} = \left\{ \frac{\alpha_1}{J_c}, \frac{\partial g_k}{\partial \mu} \right\}, \tag{3.58d}$$

where the inner-product is defined as $\{a, b\} \equiv \sum_{\sigma_t} \int d\mathcal{E} d\mu J_c \, ab$. The explicit part can be obtained only from the lowest-order distribution function $\bar{f}_0$. This is totally different from the situation in the conventional Eulerian approach, in which the lowest-order local Maxwellian f_M bears no flux. For the implicit part, one need the solution of Eq. (3.53) for g_k. The solution is shown in the next subsection. The physical meaning of the implicit part is interpreted as a correlation between test particles disposed according to $\bar{f}_0$ and the field particles $\bar{f}_1$ which represents the deviation of background distribution from $\bar{f}_0$. On the other hand, the explicit part represents the transport caused by collisions of two particles both of which are disposed according to $\bar{f}_0$ but have different density and temperature corresponding to the averaged position $\langle \psi \rangle$ of each particle. Thus the separation of the explicit and implicit part reflects physical mechanics of transport phenomena. A more detailed discussion can be found in Ref. [20, 34]. In the next subsection, however, it will be shown that we can calculate the transport coefficients only in the form of the total ones : $S_{jk} \equiv S_{jk}^{ex} + S_{jk}^{im}$.

To obtain the energy transport equation, the moment to be taken is $\int d\mathcal{E} d\mu J_c W$, where $W = \mathcal{E} - e_i \Phi(\langle \psi \rangle)$. Define here

$$\mathcal{Q}_i \equiv \sum_{\sigma_t} \int d\mathcal{E} d\mu J_c W \bar{f}_{i0}, \tag{3.59}$$

which is the sum of the kinetic energy of particles with the same $\langle \psi \rangle$. The use of partial integrals yields the energy conservation equation

$$\frac{\partial}{\partial t} \mathcal{Q}_i + \frac{\partial}{\partial \langle \psi \rangle} \left[J_2^i + \frac{3}{2} J_1^i T_i \right] = -e_i J_1^i \frac{d\Phi}{d\langle \psi \rangle}, \tag{3.60}$$

where J_2^i represents the conductive ion heat flux

$$\frac{J_2^i}{T_i} = \sum_{k=1}^{3}(S_{2k}^{ex} + S_{2k}^{im})F_k, \tag{3.61}$$

where

$$S_{21}^{ex} = -\left\{\nu_i \frac{\mu}{e_i}\left\langle \frac{I^2}{\Omega_i}\gamma^2 \right\rangle, \left(c_i^2 - \frac{3}{2}\right)\bar{f}_{i0}\right\}, \tag{3.62a}$$

$$S_{22}^{ex} = -\left\{\nu_i \frac{\mu}{e_i}\left\langle \frac{I^2}{\Omega_i}\gamma^2 \right\rangle, \left(c_i^2 - \frac{3}{2}\right)^2\bar{f}_{i0}\right\}, \tag{3.62b}$$

$$S_{23}^{ex} = -\left\{\nu_i \frac{\mu}{e_i}\left\langle \frac{I^2\gamma}{\Omega_i} \right\rangle, \left(c_i^2 - \frac{3}{2}\right)\bar{f}_{i0}\right\}, \tag{3.62c}$$

$$S_{2k}^{im} = \left\{\frac{\alpha_2}{J_c}, \frac{\partial g_k}{\partial \mu}\right\}. \tag{3.62d}$$

The right hand side of Eq. (3.60) describes work done by the radial ion current.

3.3.2 Properties of transport coefficients

An important property of the transport coefficients S_{jk} is the symmetry of the implicit part $S_{jk}^{im} = S_{kj}^{im}$. This can be shown by as follows. First, integrating both sides of Eq. (3.53) by μ yields

$$\alpha_j = \frac{J_c \nu_i}{\bar{f}_{i0}}\left\langle \frac{mv_\parallel^2}{B} \right\rangle \mu \frac{\partial g_j}{\partial \mu}, \tag{3.63}$$

where the integral constant is zero from the boundary condition. Then, one obtains

$$\begin{aligned} S_{jk}^{im} &= \sum_{\sigma_t}\int d\mathcal{E}d\mu\alpha_j\frac{\partial g_k}{\partial \mu} \\ &= \sum_{\sigma_t}\int d\mathcal{E}d\mu J_c\frac{\nu_i}{\bar{f}_{i0}}\left\langle \frac{mv_\parallel^2}{B} \right\rangle \mu\frac{\partial g_j}{\partial \mu}\frac{\partial g_k}{\partial \mu}. \end{aligned} \tag{3.64}$$

This equation is symmetric in j and k, therefore implicit coefficients are symmetric.

One can also find that the explicit part has a symmetry $S_{12}^{ex} = S_{21}^{ex}$. Then, it is natural to seek the third flux which satisfies the symmetry $S_{3k}^{ex} = S_{k3}^{ex}$;

$$J_3^i \equiv \sum_{k=1}^{3}(S_{3k}^{ex} + S_{3k}^{im})F_k. \tag{3.65}$$

Now we show that the proper definition of the third flux is

$$J_3^i \equiv \frac{2\bar{n}_i\mathcal{K}_1}{\tau_i}\left\langle \frac{Iu_{i\parallel}}{\Omega} \right\rangle_\psi \frac{dV}{d\psi}. \tag{3.66}$$

Noting that $\langle \cdots \rangle_\psi$ means the flux-surface average, we have

$$
\begin{aligned}
J_3^i &= 4\pi^2 \int_0^{2\pi} \frac{d\theta}{\mathbf{B}\cdot\nabla\theta}\frac{I}{\Omega_i}\int d\mathcal{E}' d\mu' \frac{B_*}{m_i^2|v_\parallel'|}\nu_i(v')v_\parallel' f_i \Bigg|_{\psi=\langle\psi\rangle} \\
&= \frac{4\pi^2}{m_i^2}\int_0^{2\pi} \frac{d\theta}{\mathbf{B}\cdot\nabla\theta}\frac{I}{\Omega_i}\int d\mathcal{E}' d\mu' d\psi' \delta(\langle\psi\rangle - \psi')\sigma_\parallel' B_* f_i \frac{\partial}{\partial\mu'}(\nu_i\mu') \\
&= -\frac{4\pi^2}{m_i^2}\int_0^{2\pi} \frac{d\theta}{\mathbf{B}\cdot\nabla\theta}\frac{I}{\Omega_i}\int d\mathcal{E}' d\mu' d\langle\psi\rangle' \left|\frac{\partial\psi}{\partial\langle\psi\rangle}\right| \sigma_\parallel' B_* \nu_i\mu' \frac{\partial}{\partial\mu'} f_i.
\end{aligned}
$$

Next, distribution function is expanded as

$$
\frac{\partial f_i}{\partial\mu} \simeq \frac{\partial}{\partial\mu}\left[\bar{f}_{i0} - \Delta_\psi \frac{\partial \bar{f}_{i0}}{\partial\langle\psi\rangle} + \bar{f}_{i1}\right] = \frac{I\gamma}{e_i v_\parallel}\frac{\partial \bar{f}_{i0}}{\partial\langle\psi\rangle} + \frac{\partial \bar{f}_{i1}}{\partial\mu}, \tag{3.67}
$$

where

$$
\Delta_\psi \equiv \psi - \langle\psi\rangle = \frac{Iv_\parallel}{\Omega_i} - \left\langle \frac{Iv_\parallel}{\Omega_i}\right\rangle \tag{3.68}
$$

represents the deviation from an instantaneous particle position to its averaged flux-surface, and we use the relation $\partial\Delta_\psi/\partial\mu = -\partial\langle\psi\rangle/\partial\mu$. Using Eqs. (3.15) and (3.16), and changing the order of integrals, we have

$$
\begin{aligned}
J_3^i &= -\sum_{\sigma_t}\int d\mathcal{E} d\mu \frac{4\pi^2\tau_p}{m_i^2}|1-\delta_*|\frac{\nu_i\mu}{\tau_p}\oint \frac{d\theta}{\dot{\theta}}\frac{Iv_\parallel}{\Omega_i}\frac{\partial}{\partial\mu}\bar{f}_i \\
&= -\sum_{\sigma_t}\int d\mathcal{E} d\mu J_c \left[\frac{\nu_i\mu}{e_i}\left\langle\frac{I^2\gamma}{\Omega_i}\right\rangle \frac{\partial\bar{f}_{i0}}{\partial\langle\psi\rangle} + \nu_i\left\langle\frac{Iv_\parallel}{\Omega_i}\right\rangle \mu\frac{\partial f_{i1}}{\partial\mu}\right].
\end{aligned} \tag{3.69}
$$

Note here that the implicit coefficients S_{3k}^{im} are written as follows, by its definition,

$$
S_{3k}^{im} \equiv \left\{\frac{\alpha_3}{J_c}, \frac{\partial g_k}{\partial\mu}\right\} = -\sum_{\sigma_t}\int d\mathcal{E} d\mu J_c \nu_i \left\langle\frac{Iv_\parallel}{\Omega_i}\right\rangle \mu\frac{\partial g_k}{\partial\mu}. \tag{3.70}
$$

Then, comparing Eqs. (3.69) and (3.70), one finds that the explicit coefficients for J_3^i are given as follows

$$
S_{31}^{ex} = -\left\{\nu_i\frac{\mu}{e_i}\left\langle\frac{I^2\gamma}{\Omega_i}\right\rangle, \bar{f}_{i0}\right\} = S_{13}^{ex}, \tag{3.71a}
$$

$$
S_{32}^{ex} = -\left\{\nu_i\frac{\mu}{e_i}\left\langle\frac{I^2\gamma}{\Omega_i}\right\rangle, \left(c_i^2 - \frac{3}{2}\right)\bar{f}_{i0}\right\} = S_{23}^{ex}, \tag{3.71b}
$$

$$
S_{33}^{ex} = 0. \tag{3.71c}
$$

Thus we obtain the 3×3 symmetric coefficients for both explicit and implicit parts.

To close transport equations, we must eliminate the additional driving force F_3 introduced to include the parallel momentum balance. For this purpose, we choose $\overline{u_{i\parallel}}$ as follows

$$
\overline{u_{i\parallel}} \equiv \frac{\Omega_{i0}}{I_0\langle h^2\rangle_\psi}\left\langle\frac{Iu_{i\parallel}}{\Omega}\right\rangle_\psi. \tag{3.72}
$$

The factor $\langle h^2\rangle_\psi$, where $h \equiv B_0/B$, is needed to retain the ambipolarity in the SOW limit, as shown in Appendix D. By using this definition, Eq. (3.65) can be solved for F_3. It yields

$$F_3 = -\beta(S_{13}F_1 + S_{23}F_2), \tag{3.73}$$

$$\beta = -\left(\frac{\bar{n}_i\mathcal{K}_1}{\tau_i}I_0^2\rho_{i0}^2\frac{dV}{d\psi}\langle h^2\rangle_\psi - S_{33}^{im}\right)^{-1}, \tag{3.74}$$

where $S_{jk} = S_{jk}^{ex} + S_{jk}^{im}$ is the total transport coefficients. Finally, neoclassical fluxes are rewritten in the following form

$$\begin{bmatrix} J_1^i \\ J_2^i/T_i \end{bmatrix} = \begin{bmatrix} A_{11} & A_{12} \\ A_{21} & A_{22} \end{bmatrix} \cdot \begin{bmatrix} F_1 \\ F_2 \end{bmatrix}, \tag{3.75}$$

where

$$A_{11} = S_{11} - \beta S_{13}^2, \tag{3.76a}$$

$$A_{12} = A_{21} = S_{12} - \beta S_{13}S_{23}, \tag{3.76b}$$

$$A_{22} = S_{22} - \beta S_{23}^2. \tag{3.76c}$$

Thus the resulting transport matrix A_{jk} in the Lagrangian formulation is shown to be Onsagar-symmetry as in the Eulerian formulation.

Next, let us calculate the total coefficients S_{jk}. The perturbed distribution functions g_k are needed to calculate the implicit part. From Eq. (3.63), we obtain

$$\frac{\partial g_1}{\partial \mu} = -\frac{\langle I\gamma v_\parallel/\Omega_i\rangle}{\langle m_i v_\parallel^2/B\rangle}\bar{f}_{i0}, \tag{3.77a}$$

$$\frac{\partial g_2}{\partial \mu} = -\left(c_i^2 - \frac{3}{2}\right)\frac{\langle I\gamma v_\parallel/\Omega_i\rangle}{\langle m_i v_\parallel^2/B\rangle}\bar{f}_{i0}, \tag{3.77b}$$

$$\frac{\partial g_3}{\partial \mu} = -\frac{\langle I v_\parallel/\Omega_i\rangle}{\langle m_i v_\parallel^2/B\rangle}\bar{f}_{i0}. \tag{3.77c}$$

From here on, we use the approximation $I(\psi) = I_0 = R_0B_0$, which corresponds to the low-β plasma. For j ,$k = 1$ or 2, using Eq. (3.39) yields

$$\begin{aligned} S_{jk} &= -\frac{I_0^2}{e_i\Omega_{i0}}\left\{\frac{\nu_i\mu}{(1-\delta_*)^2}\left(\langle h(1-\Delta_c)^2\rangle - \frac{\langle hv_\parallel(1-\Delta_c)\rangle^2}{\langle hv_\parallel^2\rangle}\right), \left(c_i^2 - \frac{3}{2}\right)^{j+k-2}\bar{f}_{i0}\right\} \\ &= -\frac{3\pi I_0^2\bar{n}_i\rho_{i0}^2qR_0}{8\tau_iB_0}\sum_{\sigma_t}\int dxd\lambda_0\frac{\bar{\tau}_p}{(1-\delta_*)}c_i\left(c_i^2 - \frac{3}{2}\right)^{j+k-2}y(c_i)\lambda_0\left(\langle h\rangle - \frac{\langle hv_\parallel\rangle^2}{\langle hv_\parallel^2\rangle}\right) \\ &\equiv \frac{3\pi I_0^2\bar{n}_i\rho_{i0}^2qR_0}{8\tau_iB_0}\bar{S}_{jk}. \end{aligned} \tag{3.78}$$

where $x = \exp(-\mathcal{E}/T_i)$, $\lambda_0 = \mu B_0/\mathcal{E}$, and $\bar{\tau}_p = \tau_p v_{thi}/qR_0$, respectively. We call $\bar{S}_{jk}$ the normalized transport coefficients. In the equation above, the terms which are proportional to Δ_c and Δ_c^2 are exactly canceled. In a similar way, one has

$$\bar{S}_{j3} = -\sum_{\sigma_t} \int dx d\lambda_0 \bar{\tau}_p c_i \left(c_i^2 - \frac{3}{2}\right)^{j-1} y(c_i)\lambda_0 \left(\langle h\rangle - \frac{\langle hv_\parallel\rangle^2}{\langle hv_\parallel^2\rangle}\right), \tag{3.79}$$

$$\bar{S}_{33}^{im} = \sum_{\sigma_t} \int dx d\lambda_0 \bar{\tau}_p c_i y(c_i)\lambda_0 \frac{\langle hv_\parallel\rangle^2}{\langle hv_\parallel^2\rangle}. \tag{3.80}$$

Note that Eq. (3.78) differs from Eq. (3.79) only by the factor $(1-\delta_*)^{-1} \simeq 1$. Therefore, this difference is neglected in the final calculations, and the approximation $S_{13} = S_{11}$ and $S_{23} = S_{12}$ are used. As a complement, we define

$$\bar{\beta} = -\left(\frac{8B_0\mathcal{K}_1}{3\pi qR_0}\frac{dV}{d\psi}\langle h^2\rangle_\psi - \bar{S}_{33}\right)^{-1} \tag{3.81}$$

so that Eq. (3.73) can be rewritten as $F_3 = -\bar{\beta}(\bar{S}_{13}F_1 + \bar{S}_{23}F_2)$.

In the SOW limit, $\langle hv_\parallel\rangle^2 = 0$ for banana particles, while $\langle hv_\parallel\rangle^2 \simeq \langle hv_\parallel^2\rangle$ for passing ones. Therefore transport coefficients other than S_{33} are determined mainly by the banana part. Because of this separation of the contribution to transport between banana and passing, the approximation of $\partial\langle\psi\rangle/\partial\mathbf{v}$ as in Eq. (3.37) used in Ref. [22] ends up in the same result as the SOW limit of Eqs. (3.78) to (3.80). However, by using the exact solution for S_{jk}, we can include the contribution for neoclassical transport not qualitatively, but quantitatively, from all the orbit-types of particles appearing in the near-axis region. The magnitude of contribution of each particle is evaluated by the factor $\langle h\rangle - \langle hv_\parallel\rangle^2/\langle hv_\parallel^2\rangle$.

In the present analysis, we improved the treatment of collision term to retain the momentum conservation low. Since we consider only the ion-ion self-collisions here, J_1^i must vanish in the SOW limit. It is shown in Appendix D that A_{11} and A_{12} become zero in this limit, and therefore J_1^i vanishes intrinsically. Thus the Lagrangian transport theory applied to the region away from the axis, where potato particles do not appear and the SOW limit is valid, reproduces the results of the conventional Eulerian transport theory.

3.3.3 Comparison with Eulerian transport theory

The representation of fluxes in Eqs. (3.56) and (3.60) from the Lagrangian formulation are different from those in the standard neoclassical transport theory based on the Eulerian representation. The former describes the change in $\mathcal{N}_i$ and $\mathcal{Q}_i$ which are functions of averaged particle position $\langle\psi\rangle$, while the latter describes the change in n_i and

$p_i = n_i T_i$ through radial fluxes averaged on a magnetic surface ψ. Then, the comparison of the neoclassical fluxes between these two representations is not straightforward. Let us consider this problem here.

As a preparation, we introduce a normalizing factor for $\mathcal{Q}_i$ as follows

$$\begin{aligned}\lambda_q(\langle\psi\rangle) &\equiv \frac{3}{2}\bar{n}_i T_i V' \mathcal{Q}_i^{-1} \\ &= \frac{3T_i}{2}\left(\frac{2\pi T_i}{m_i}\right)^{3/2} V' \Big/ \sum_{\sigma_t}\int d\mathcal{E}\, d\mu J_c W \exp\left[-\frac{W}{T_i}\right], \end{aligned} \tag{3.82}$$

where $V' = dV/d\psi(\psi = \langle\psi\rangle)$. λ_q has a similar property to λ_n appearing in Eq. (3.45). The particle flux and the heat flux are redefined as

$$\Gamma_i \equiv J_1^i/V', \tag{3.83a}$$

$$q_i \equiv J_2^i/V', \tag{3.83b}$$

so that they represent fluxes per unit cross-section. Note that q_i differs from its general definition in Eulerian representation by $\Gamma_i T_i$ since we adopt $F_2 = d\ln T_i/d\langle\psi\rangle$ as a driving force rather than the pressure gradient. Then the conservation equations of particle and energy are rewritten as follows

$$\frac{\partial \bar{n}_i}{\partial t} + \frac{\lambda_n}{V'}\frac{\partial}{\partial\langle\psi\rangle}(V'\Gamma_i) = 0, \tag{3.84}$$

$$\frac{\partial}{\partial t}\left(\frac{3}{2}\bar{n}_i T_i\right) + \frac{\lambda_q}{V'}\frac{\partial}{\partial\langle\psi\rangle}\left[V'\left(q_i + \frac{3}{2}\Gamma_i T_i\right)\right] = -\lambda_q e_i \Gamma_i \frac{d\Phi}{d\langle\psi\rangle}, \tag{3.85}$$

where we assume that the time variation of λ_n and λ_q are slow compared with those of $\mathcal{N}_i$ and $\mathcal{Q}_i$. These equations have the same dimensions as those of a standard Eulerian representation[8]. In the SOW limit, λ_n and λ_q becomes unity, and Eqs. (3.84) and (3.85) reduce to the Eulerian representation.

As will be shown in §4.3 , λ_n and λ_q is nearly unity around the region $\langle r\rangle \sim r_p$ though the finiteness of the potato width significantly affects the transport coefficients there. Only in the region $\langle r\rangle \lesssim q\rho_{i0}$ they become much larger than unity. Then, the qualitative difference in Γ_i and q_i between two representations are not so much significant as far as we are interested in the neoclassical transport around $\langle r\rangle \sim r_p$.

3.3.4 Ion heat flux

As the end of this chapter, we define here the ion thermal conductivity to compare the result with the standard Eulerian theory. In Eulerian transport theory, the ion heat flux is expressed as follows

$$\frac{q_i}{T_i} = -n_i \chi_i^r \frac{d}{dr}\ln T_i, \tag{3.86}$$

where χ_i^r is the ion thermal conductivity in the r direction. Here, q_i in the form as above is the result of (i) neglecting ion-electron collisions, and (ii) $\Gamma_i = 0$ because of the momentum conservation in ion-ion self-collisions. In the Lagrangian approach, however, the condition $\Gamma_i = 0$ is not intrinsic. In reality, the momentum-restoring term $S_{13}F_3$ in J_1^i cannot exactly cancel $S_{11}F_1 + S_{12}F_2$, especially in the region near the magnetic axis. This is because of the non-local nature of the Lagrangian formulation, and partially because only the lowest order expansion of $\overline{u_{i\|}}$ is included. In the present calculation, we rewrite the transport equation in Eq. (3.75) to eliminate F_1

$$\frac{q_i^{\langle r\rangle}}{T_i} = \frac{\bar{S}_{12}}{\bar{S}_{11}}\Gamma_i^{\langle r\rangle} - \bar{n}_i\chi_i^{\langle r\rangle}\frac{d}{d\langle r\rangle}\ln T_i, \tag{3.87}$$

$$\chi_i^{\langle r\rangle} = -\frac{3q^2\rho_{i0}^2}{32\pi\langle\epsilon\rangle^2\tau_i}\left[\bar{S}_{22} - \frac{\bar{S}_{12}^2}{\bar{S}_{11}}\right], \tag{3.88}$$

where q, ρ_{i0}, and τ_i are evaluated at $r = \langle r\rangle$, and we change here the radial coordinate from $\langle\psi\rangle$ to $\langle r\rangle$. The ion heat conductivity $\chi_i^{\langle r\rangle}$ defined in this way is to be compared to χ_i^r in the next chapter, though $\Gamma_i^{\langle r\rangle}$ does not vanish here.

It is well-known that $\chi_i^r \propto q^2\rho_{i0}^2/(\epsilon^{3/2}\tau_i)$ in the Eulerian theory, while the apparent dependence of $\chi_i^{\langle r\rangle}$ is $q^2\rho_{i0}^2/(\langle\epsilon\rangle^2\tau_i)$. However, $\bar{S}_{jk}$ away from the magnetic axis is found to be proportional to $\sqrt{\langle\epsilon\rangle}$, and $\chi_i^{\langle r\rangle}$ has the same dependency as χ_i^r there.

Chapter 4

Numerical calculation of ion thermal conductivity

4.1 Definition of collisionless regime

In this chapter, we calculate the ion thermal conductivity in the near-axis region. As a preparation, let us reconsider the definition of the collisionless regime in which Lagrangian approach is valid.

Usually, the collisionless (or banana) regime is defined as follows

$$\begin{aligned} \tau_b \sim \frac{qR_0}{v_{thi}\sqrt{\epsilon}} \quad &, \quad \nu_c^{eff} \sim \frac{\nu_i}{\epsilon}, \\ \Rightarrow \ \delta_c \ \sim \ &\frac{\nu_i q R_0}{v_{thi}\epsilon^{3/2}} \ll 1, \end{aligned} \tag{4.1}$$

since banana particles exist in the range $|v_\parallel| \lesssim v\sqrt{\epsilon}$. In an Eulerian representation, collisions cause diffusion only in the velocity space, and then the collisionless regime can be defined as above. In Lagrangian representation, however, collisions bring about diffusion directly in the $\langle\psi\rangle$ direction through the factor $\partial\langle\psi\rangle/\partial v_\parallel$. This fact means that the effect of scattering on each particle differs according to this factor.

Remember here that, as mentioned in §3.3.2, transport coefficients can be obtained by using the estimation that

$$\frac{\partial\langle\psi\rangle}{\partial v_\parallel} \sim \begin{cases} -\dfrac{I}{\Omega} & \text{(banana)}, \\ 0 & \text{(well} - \text{passing)}. \end{cases} \tag{4.2}$$

In the near-axis region, potato particles can be assumed to have $\partial\langle\psi\rangle/\partial v_\parallel \sim -I/\Omega$ like bananas. The transition of orbit topology of a potato particle occurs when their

averaged radial position changes as large as its orbit width $\Delta_r \sim r_p$, or

$$\Delta_\psi \sim \frac{I}{\Omega_0}\left(\frac{q\rho_{i0}}{R_0}\right)^{1/3}. \tag{4.3}$$

To change $\langle\psi\rangle$ as large as Δ_ψ, pitch-angle scattering of the magnitude

$$\Delta v_\parallel \sim \Delta_\psi \Big/ \frac{\partial\langle\psi\rangle}{\partial v_\parallel} = \left(\frac{q\rho_{i0}}{R_0}\right)^{1/3} v_{thi}$$

is needed. Therefore, on the analogy of Eq. (4.1), the effective collision frequency for potato ions can be defined as

$$\nu_c^{eff} = \frac{1}{\tau_i}\left(\frac{R_0}{q\rho_{i0}}\right)^{2/3}. \tag{4.4}$$

On the other hand, τ_p for potato particles is estimated as

$$\tau_p^{pot} \sim \frac{qR_0}{v_{thi}}\left(\frac{R_0}{q\rho_{i0}}\right)^{1/3}. \tag{4.5}$$

From Eq. (4.4) and (4.5), we obtain

$$\begin{aligned} \delta_c^{pot} &= \nu_c^{eff}\tau_p^{pot} \ll 1 \\ \Leftrightarrow\ T_i &\gg \frac{Z_i^2(\bar{n}_i B_0 R_0^2)^{2/5}}{(m_i/m_p)^{1/5}} \end{aligned} \tag{4.6}$$

where T_i (keV), $\bar{n}_i$ ($10^{20}\mathrm{m}^{-3}$) and m_p is the mass of proton. For example, if $B_0 = 4$T, $R_0 = 4$m and $\bar{n}_i = 1 \times 10^{20}\mathrm{m}^{-3}$ for hydrogen ion, then $T_i \gg 5$keV is needed for the collisionless assumption. Note that the criterion Eq. (4.6) corresponds to that from the usual definition of δ_c in Eq. (4.1) evaluated at $r \simeq r_p$ as mentioned in Ref. [18].

In reality, barely-transit potato particles have much longer τ_p than the estimation in Eq. (4.5). Then, particles around the transition boundary $l2$ in Fig. 2.11 may break the collisionless assumption $\delta_c \ll 1$. Treating these collisional particles in the Lagrangian transport theory like the banana-plateau transition in the standard Eulerian theory[8] is not considered here. Therefore, our calculation corresponds to the collisionless limit of neoclassical transport.

4.2 Numerical method

Numerical calculation of transport coefficients in Eqs. (3.78) to (3.80) is implemented by using a Monte Carlo integration method. We developed a numerical calculation code "NEO" in order to obtain transport coefficients in the Lagrangian formulation. In

the calculation, test particles are generated randomly and uniformly in the phase space (x, λ_0), where x and λ_0 are defined in §3.3.2. The particles are distributed in the range $x_{min} \leq x \leq x_{max}$ and $\lambda_{0min} \leq \lambda_0 \leq \lambda_{0max}$, where the upper and lower boundaries are chosen so that test particles cover the whole region in which orbits can exist. Next, the orbit of each test particle is traced from a guess starting point $r_s = \langle r \rangle + \delta_r$ and $\theta = 0$ or π, and adjust δ_r so that the calculated averaged position of all test particles lie on the same magnetic surface $r = \langle r \rangle$. Remember here that there are some overlaps in the region of each orbit type in the COM space as discussed in §2.3. Therefore, if there are two or three types of orbit for a given set of $(x, \lambda_0, \langle r \rangle)$, we must find all these orbits by varying the guess starting point around $\langle r \rangle$ and $\sigma_\parallel$. Then these orbits are counted separately. Finally, all the functions in the integrand of the normalized transport coefficients $\bar{S}_{jk}$, which we write $F_{jk}(x, \lambda_0, \langle r \rangle; \sigma_t)$ here, are calculated by tracing each particle orbit, and transport coefficients at $\langle r \rangle$ are given as

$$\bar{S}_{jk}(\langle r \rangle) = \lim_{N \to \infty} \frac{(x_{max} - x_{min})(\lambda_{0max} - \lambda_{0min})}{N} \sum_{n=1}^{N} \sum_{\sigma_t} F_{jk}(x_n, \lambda_{0n}, \langle r \rangle; \sigma_{tn}), \tag{4.7}$$

where N is total number of test particles and $(x_n, \lambda_{0n}, \langle r \rangle; \sigma_{tn})$ is the position of n-th test particle in the phase space. If there is no particle orbit corresponds to $(x_n, \lambda_{0n}, \langle r \rangle)$, then F_{jk} is evaluated as zero for such particles. (Note that the total number N includes such miss-shot particles.) The functions F_{jk} consist of the poloidal period τ_p, and averaged functions such as $\langle h \rangle$, $\langle h v_\parallel \rangle^2$, and $\langle h v_\parallel^2 \rangle$. These values are easily calculated numerically. Note that we approximate $1 - \delta_* = 1$ so that $\bar{S}_{11} = \bar{S}_{13}$ and $\bar{S}_{12} = \bar{S}_{23}$.

To reduce the numerical error in transport coefficients, we adopt a technique of the stratified sampling in the implementation of Monte Carlo integration. The (x, λ_0) plane is divided into several cells, and the integration is carried out in each cell. Because the main contribution to transport coefficients comes from banana and kidney particles, more particles are distributed to the cells in the range $1 - \langle \epsilon \rangle \leq \lambda_0 \leq 1 + \langle \epsilon \rangle$.

High-performance computing using parallelized cluster system is an interesting topic in recent numerical science. We use a 12-node PC cluster system with MPI (Message Passing Interface) programming to reduce the calculation time. Since Monte Carlo method is suitable to parallelized calculation, the parallelization efficiency of the NEO code is as good as 95% of the theoretical maximum. To obtain transport coefficients on a given $\langle r \rangle$ with the relative error lower than 10^{-3}, it takes about 1×10^6 test particles and about one day in this system.

In Figs. 4.1 and 4.2, examples of test particle distribution in the (x, λ_0) plane for $\langle r \rangle = 0.105$m and $\langle r \rangle = 0.25$m are shown. One finds a similarity between Figs. 4.1 and

2.11 though the scale of the horizontal axis are different between these figures. This apparent similarity can be understood by noticing the dependence of potato width $\Delta_r \sim (q^2\rho^2 R_0)^{1/3}$ on particle energy. Figure 4.1(a) correspond to the situation that Δ_r for thermal energy particles ($x \sim 0.4$) becomes $0.1\mathrm{m}$. For lower energy particles ($x \sim 1$), $\Delta_r \propto \rho^{2/3}$ is smaller than $\langle r \rangle = 0.105\mathrm{m}$, and then the banana region lies in the range $1 - \langle \epsilon \rangle \leq \lambda_0 \leq 1 + \langle \epsilon \rangle$ like in the conventional SOW limit analysis. On the other hand, for energetic particles ($x \sim 0$), $q\rho$ is comparable to their averaged position $\langle r \rangle = 0.105\mathrm{m}$, and then energetic particles appear as inner- and outer-circulating particles.

In the case of away from the axis as in Fig. 4.2, Δ_r becomes comparable to $\langle r \rangle = 0.25\mathrm{m}$ only for very high-energy particles, and most part of particles in the range $1-\langle \epsilon \rangle \leq \lambda_0 \leq 1 + \langle \epsilon \rangle$ is the conventional banana particles. However, it should be noted that, even in the region away from the axis, the kidney region exists between the boundaries of the passing and banana regions. Kidney orbit can be considered as a transition state between banana and passing. Since such transition particles will significantly contribute to radial transport, one cannot neglect the existence of kidney in a transport calculation. The adoption of Monte Carlo integration method enables the NEO code to evaluate correctly all the types of orbit to transport coefficients in any configuration.

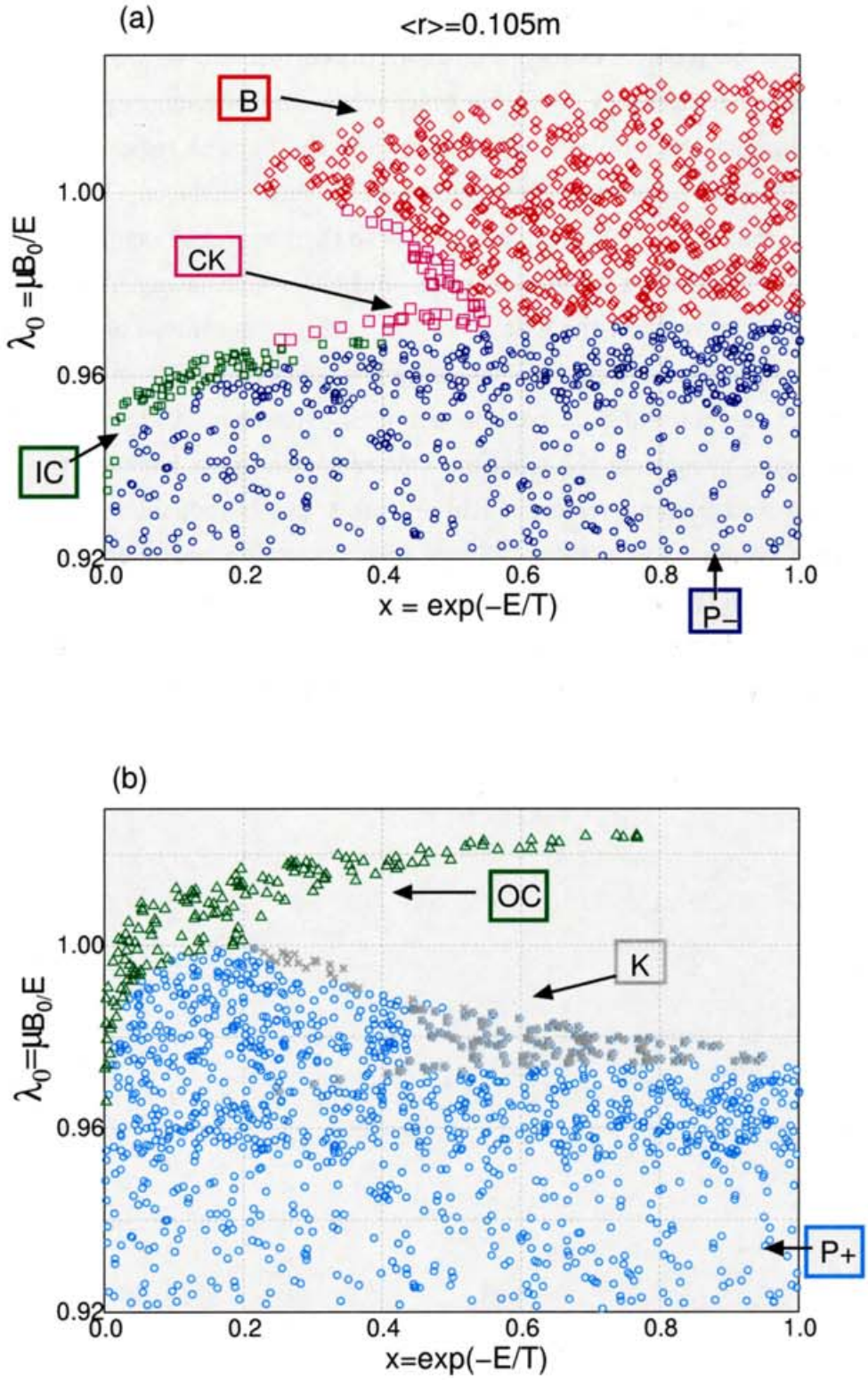

Figure 4.1: The marker distribution in the (x, λ_0) plane at $\langle r \rangle = 0.105\mathrm{m}$. Abbreviations of orbit types are the same as in Fig. 2.11. Note that the kidney region is overlapped with the co-passing region in Fig. (b).

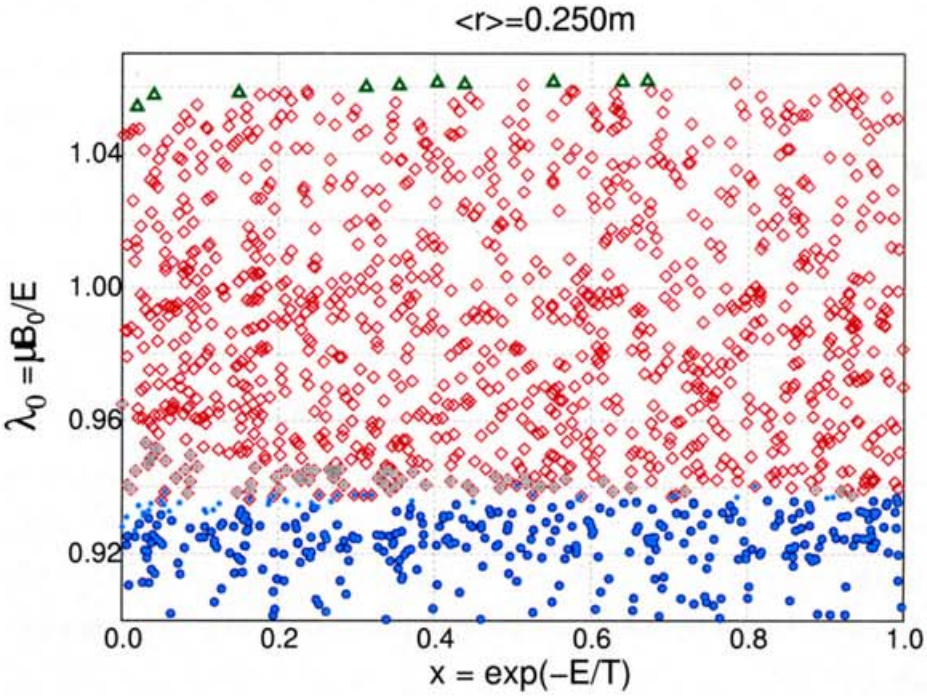

Figure 4.2: The marker distribution in the (x, λ_0) plane at $\langle r \rangle = 0.25\mathrm{m}$. The mark of each orbit type is the same as in Fig. 4.1.

4.3 Numerical results of χ_i

As a example, we calculate the ion thermal conductivity $\chi_i^{\langle r\rangle}$ under the conditions $B_0 = 4\mathrm{T}$, $q = 3$, $T_i = 20\mathrm{keV}$ and $\bar{n}_i = 1 \times 10^{20}\mathrm{m}^{-3}$. The radial electric field $d\Phi/dr$ is neglected. In this case, typical potato particles appear in the region $\langle r\rangle \lesssim r_p = 0.246\mathrm{m}$. According to Eq. (4.6), the plasma is well in the collisionless regime. The calculation result of $\chi_i^{\langle r\rangle}$, which is defined by Eq. (3.88), is plotted in Fig. 4.3. For a comparison, χ_i^r by a standard Eulerian theory in the banana regime[8] is also plotted. Note that χ_i^r is plotted by regarding r as $\langle r\rangle$.

A significant reduction in $\chi_i^{\langle r\rangle}$ can be seen in the region $\langle r\rangle \lesssim r_p$. The main reason of the reduction of $\chi_i^{\langle r\rangle}$ in Lagrangian approach is that potato particles, which mainly contribute to the radial transport, cannot exist in the region $\langle r\rangle \ll r_p$ when observed in the COM space $(\mathcal{E}, \mu, \langle r\rangle)$ as is shown in Figs. 2.11 and 4.1. The FOW effect is thus included in the calculation by reflecting the real population of potato particles neat the magnetic axis.

In Fig. 4.4, λ_q defined in Eq. (3.82) is plotted. One can see that λ_q becomes much larger than unity only on the inner-most point $\langle r\rangle = 2q\rho_{i0} = 0.03\mathrm{m}$ in this case. As mentioned in §3.3.3, simple comparison of χ_i between Lagrangian and Eulerian formulations is possible as long as $\lambda_q \simeq 1$. Then it can be said that the reduction of the ion thermal conductivity occur not only when it is observed in the $\langle r\rangle$-coordinate, but also in the real space around $r \sim r_p$. On the other hand, it can be an underestimation that $\chi_i\tau_i/q^2\rho_{i0}^2 \sim 0.1$ at $\langle r\rangle = 0.03\mathrm{m}$ because it is almost the same level as the classical transport $\chi_i \sim \rho_{i0}^2/\tau_i$, and also because of $\lambda_q \gg 1$ there.

In Fig. 4.4, we also plot A_{11}/A_{22} which is approximately the ratio of Γ_i to q_i. Away from the axis it is almost zero and then Γ_i can be neglected, while it becomes finite around $\langle r\rangle \sim r_p/2$. It is the FOW effect that cause the finite particle flux by ion-ion collisions. Since the electron particle flux is negligible compared to the ion flux, radial electric field E_r will develops to satisfy ambipolarity $\Gamma_i = 0 + O(\sqrt{m_e/m_i})$ [17]. In our present calculation, however, the ambipolar electric field cannot be calculated correctly, because it requires to solve dE_r/dt from the particle flux equation, which in turn affects transport coefficients $A_{jk}(\langle r\rangle, t)$ through the orbit-squeezing effect of potato particles[36]. It is a future work to determine neoclassical E_r in the core region.

Next, to investigate the degree of contribution from each orbit type to transport coefficients, we plot in Figs. 4.5(a) and (b) the factor $H_\parallel = \langle h\rangle - \langle hv_\parallel\rangle^2/\langle hv_\parallel^2\rangle$ for $\mathcal{E} = 20\mathrm{keV}$ ions at $\langle r\rangle = 0.12\mathrm{m}$ and $\langle r\rangle = 0.30\mathrm{m}$, respectively. Since the normalized transport coefficients $\bar{S}_{jk}$ contains $H_\parallel$, one can see that not only banana particles but also

all the potato particles, that is, kidney, concave-kidney, outer-circulating, and inner-circulating particles appearing around the transition boundary, contribute the radial transport to the same degree at $\langle r \rangle = 0.12$m in Fig.4.5(a), where all the particles above have a potato nature. On the other hand, in the region away from the magnetic axis as in Fig. 4.5(b), $H_{\parallel}$ is almost unity for banana particles, and zero for passing particles. In such a case the approximation shown in Eq. (3.37) by Wang[22] works well. In the numerical calculation used here, the factor $H_{\parallel}$ is evaluated without any approximation by using the Monte Carlo integration method.

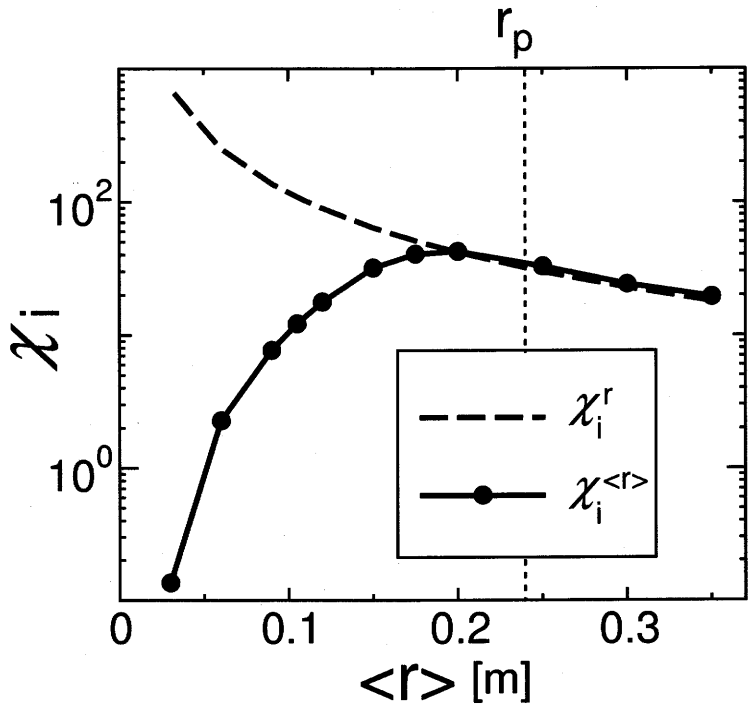

Figure 4.3: The ion thermal conductivity normalized by $q^2\rho_{i0}^2/\tau_i$, in the case $T_i = 20\text{keV}$, $q = 3$, and $n_i = 1\times10^{20}m^{-3}$. Solid line is the calculation result of the NEO code. Dashed line is from the standard Eulerian theory by Hinton and Hazeltine[8].

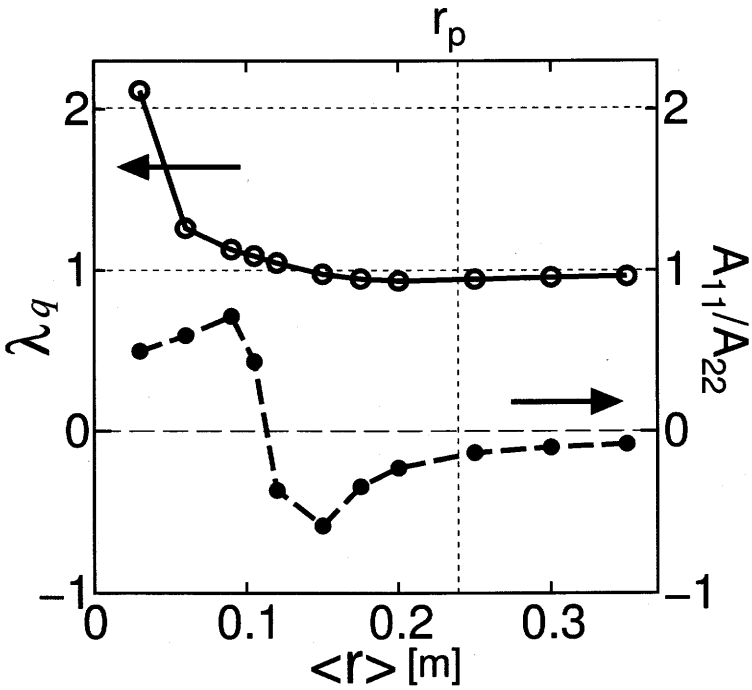

Figure 4.4: Dependence of λ_q defined in eq. (3.82) (solid line) and the ratio of transport matrix components A_{11}/A_{22} (dashed line) on $\langle r\rangle$.

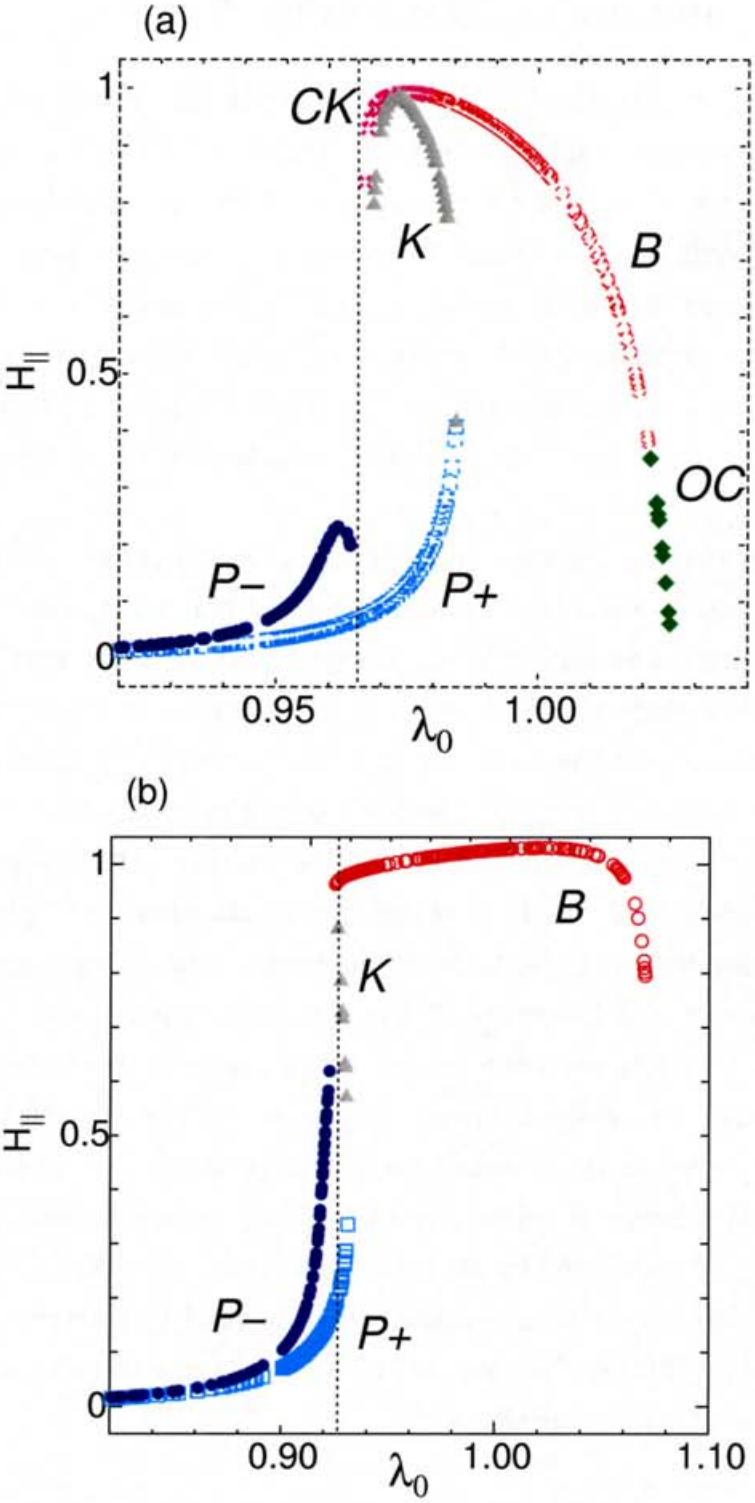

Figure 4.5: $H_{\parallel} = \langle h \rangle - \langle h v_{\parallel} \rangle^2 / \langle h v_{\parallel}^2 \rangle$ vs. λ_0 for ions with $\mathcal{E} = 20$keV at (a) : $\langle r \rangle = 0.12$m, and (b) : $\langle r \rangle = 0.30$m, respectively. The dotted lines are the position of the transition boundary $\lambda_0 = 1 - \langle \epsilon \rangle$. Abbreviations of the orbit types are the same as used in Fig. 2.11.

4.4 Dependency on the safety factor q

As mentioned previously, the FOW effect on neoclassical transport is expected to be significant in a reversed magnetic shear configuration because the potato width $\Delta_r \sim (q^2\rho^2 R_0)^{1/3}$ becomes large in this configuration. To examine the dependency of the ion thermal conductivity on the q-profile, we calculate $\chi_i^{\langle r \rangle}$ in two case, normal and reversed shear configurations. The profiles of q, $\bar{n}_i$, and T_i given in the calculation are shown in Fig. 4.6. In these cases, the potato width r_p cannot be given by the analytical solution in Eq. (2.43), and then it is numerically obtained by searching the widest orbit which passes on the magnetic axis. The numerical results of $\chi_i^{\langle r \rangle}$ and the position of r_p are shown in Fig. 4.7.

One can see that r_p becomes larger in the reversed shear configuration, and the radial position within which the reduction of $\chi_i^{\langle r \rangle}$ from the standard neoclassical level is seen moves outward according to r_p. Therefore, we conclude that r_p well represents the radial position where the FOW effect of potato orbits becomes important.

In recent experiments, the q-factor sometimes becomes very large, $q \sim 100$ for example, around the magnetic axis[37]. The NEO code can be applied to any configuration like such an extreme case. As concerning the validity of the Lagrangian transport theory, the situation is favorable in reversed magnetic shear configurations, which are often accompanied with ITB. Because the ion temperature is high and the plasma pressure profile is almost flat inside the ITB in general, two parameters δ_c and δ_b given by Eqs. (3.5) and (3.41) respectively, satisfy the assumption that they should be much smaller than unity. Therefore, Lagrangian approach will be a useful tool to considering neoclassical transport in the reversed shear configuration. Note that however, simple comparison of χ_i between Eulerian and Lagrangian representations is not valid in the region $\langle r \rangle < q\rho_{i0}$ as mentioned in the previous section. Therefore, if $q\rho_{i0}$ is comparable to r_p, or $q\rho_{i0} \sim R_0$, more consideration must be paid to interpret the result of the Lagrangian theory. This is the case for the transport of energetic alpha particles in a strongly reversed shear configuration.

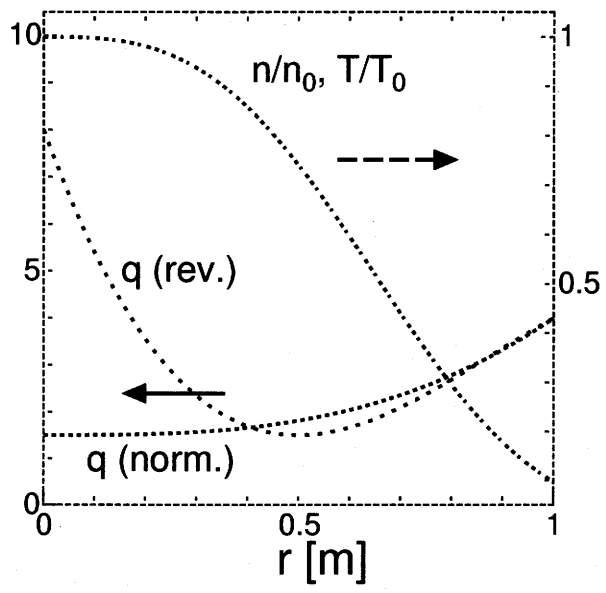

Figure 4.6: Profiles of the safety factor q, the ion density n, and the ion temperature T used in the calculation of $\chi_i^{\langle r \rangle}$ in Fig. 4.7. The value on the magnetic axis are $n_0 = 5.0 \times 10^{19} m[-3]$, and $T_0 = 5.0keV$, respectively.

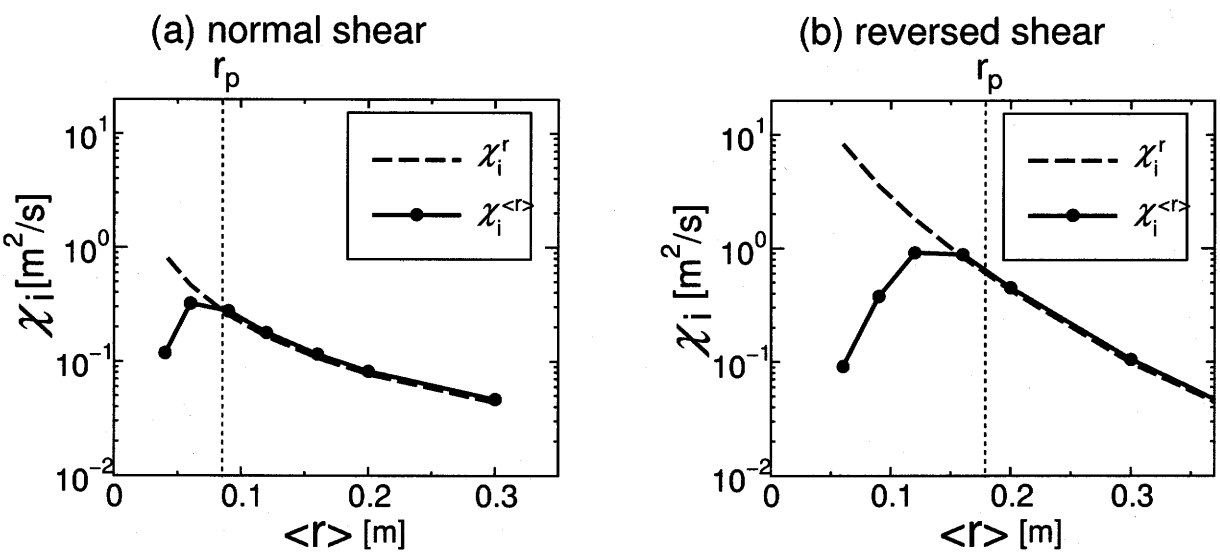

Figure 4.7: The ion thermal conductivity calculated by the NEO code in a normal shear configuration (a) and in a reversed shear configuration (b). The widest banana orbit width r_p in Fig.(a) is about $0.08m$, while it becomes $0.18m$ in Fig. (b).

Chapter 5

Comparison with other experiments and simulations

The reductive tendency of χ_i around the magnetic axis is the common feature in recent simulation results and also in recent tokamak experiments. Our $\chi_i^{\langle r \rangle}$ also shows a similar dependence on $\langle r \rangle$ to these simulations as shown in §4. Here, we compare our result with these results.

Let us make a brief review for the δf method here. The δf Monte Carlo simulation has been developed as an ingenious method to study kinetic phenomena in plasmas. It has been first proposed as a numerical method of solving nondiffusive, nonlinear gyrokinetic problems such as ion-temperature-gradient (ITG) driven instability[38]. In the δf method, particle distribution function is separated as $f = f_0 + \delta f$, where f_0 is set as a known function and only the δf part is to be solved numerically. Comparing with the full-f particle simulation, the numerical noise level is reduced by a factor of $|\delta f / f_0|^2$.

Chen and White[39] established the rigorous formalism of the δf method in collisional systems. In the formalism, the particle weight w satisfies the relation

$$wg = \delta f, \tag{5.1}$$

where g is the marker particle distribution function. The weight is recognized as a new dimension of an extended phase space $(\mathbf{x}, \mathbf{v}, w)$. The time development of δf is described by calculating dw/dt along each marker orbit. With the use of linearized collision operator for δf algorithm in which f_0 is set as a local Maxwellian f_M [40, 41], the δf method has first been applied to neoclassical transport simulation by Lin *et al.*[15]. However, they used the nonlinear weighting scheme[42] which is not suitable in diffusive systems where the assumption $g \approx f$ is not a good approximation.

To resolve this problem, Hu and Krommes[43], and Wang *et al.*[16] have extended the formalism of Chen and White by using the two-weight scheme which is accurate in collisional systems. The marker phase space is extended to $(\mathbf{x}, \mathbf{v}, w, p)$, where the new weight p satisfies

$$pg = f_M \tag{5.2}$$

in the two-weight scheme. The evolution of δf is then described by calculating both dw/dt and dp/dt along each marker orbit.

A further development of the δf method has been made by Brunner *et al.*[44], who pointed out the problem of weight spreading. It is caused by the implementation of collision operator in Monte Carlo simulation, and leads to an increasing noise in evaluating δf. They proposed a solution to reduce the weight spreading, which have been applied in recent nonlocal neoclassical transport simulations in the near-axis region by Wang *et al.*[17] and Bergmann *et al.*[18].

The linearized kinetic equation for weights w and p are given as follows[16],

$$\frac{Dw}{Dt} = \frac{p}{f_M}\left[-\mathbf{v}_d \cdot \nabla f_M + P f_M\right], \tag{5.3a}$$

$$\frac{Dp}{Dt} = \frac{p}{f_M}\mathbf{v}_d \cdot \nabla f_M, \tag{5.3b}$$

where

$$\frac{D}{Dt} = \frac{\partial}{\partial t} + (\mathbf{v}_\parallel + \mathbf{v}_d) \cdot \nabla - C_{TP}(\ \ , f_M) \tag{5.4}$$

represents the time derivative along each marker orbit and C_{TP} is the test particle collision operator, which is implemented numerically as a random kick in the velocity space. In Eq. (5.3a), Pf_M represents the field particle collision operator which is defined so as to satisfy the conservation lows for collision operator as follows

$$\int (C_{TP} + P f_M) d\mathbf{v} = 0, \tag{5.5a}$$

$$\int (C_{TP} + P f_M) \mathbf{v} d\mathbf{v} = 0, \tag{5.5b}$$

$$\int (C_{TP} + P f_M) v^2 d\mathbf{v} = 0. \tag{5.5c}$$

In the δf method, the FOW effect on neoclassical transport is correctly included by retaining the drift term $\mathbf{v}_d \cdot \nabla$ in Eq. (5.4).

We show in Figs. 5.1 and 5.2 the ion thermal conductivity obtained from the δf simulations in Ref. [16] and in Refs. [15, 18], respectively. In Fig. 5.1, the potato width r_p, $2r_p$, and $3r_p$ are also plotted. In Fig. 5.2, the result by Lin *et al.*is plotted by

using a analytic formula based on a simple random-walk model which represents well the tendency of their simulation,

$$\frac{\chi}{\chi_{thin}} = 1 - \left[1 + \left(\frac{r}{r_p}\right)^3\right] \exp\left[-\left(\frac{r}{r_p}\right)^3\right], \tag{5.6}$$

where χ_{thin} is from the standard neoclassical transport theory by Chang and Hinton[45]. Bergmann *et al.*also make a fitting formula for their simulation result,

$$\frac{\chi}{\chi_{thin}} = 1 - \left[1 - \left(\frac{r}{3r_p}\right)^2\right] \tag{5.7}$$

in the range $r < 3r_p$. A slight difference of the definition of r_p between ours by Eq. (2.43) and in Ref. [18] is negligible in evaluating r_p.

One can see in Figs. 5.1 and 5.2 the reductive tendency of resultant χ_i in the near-axis region from the level of the standard neoclassical transport theory. Comparing these δf simulations with our result using the Lagrangian transport theory shown in Figs. 4.3 and 4.7, however, there is a difference in that the reduction of χ_i compared to the standard neoclassical value begins at $r \sim r_p$ in our calculation, while it begins from somewhat more outer position $r \sim 2r_p$ in the other simulations. It must be noted here that the radial coordinate is not equivalent between the Lagrangian approach which describes fluxes as a function of averaged radial position $\langle r \rangle$, and the δf simulation which uses the minor radius r in the real space. However, we have already shown in §3.3.3 that Lagrangian and Eulerian representations of transport coefficients are almost equivalent as long as λ_n and λ_q are close to unity. Therefore, it can be said that the difference in the dependency of χ_i on r_p is not caused mainly by the difference of these two representations. This may be caused by the differences of the profiles, of the treatment of collision terms, and of the numerical algorithms used in each calculation. More detailed comparison between the Lagrangian formulation and δf simulations will be done in a future work.

Note also here that, in Fig. 5.2, the theoretical evaluation of χ_i in the Eulerian approach by Shaing *et al.*[10], which was proposed to extend standard theory to the region near the magnetic axis, yields a contradicting result which goes infinity at the magnetic axis. As we will see below, it has been shown that the ion thermal conductivity becomes lower in the near-axis region than the standard neoclassical level in many experiments. Then, usual Eulerian approach to include the FOW effect of potato orbits near the magnetic axis is found to fail in explaining the experimental results. An insufficiency in Eulerian approach is in the treatment of particle orbit near the axis,

in which they only consider orbits which intersect the magnetic axis when solving the drift-kinetic equation. (See Appendix of Ref. [10].)

Recently, Wang *et al.* have carried out a δf simulation including the self-consistent radial electric field[17]. In the simulation, the time development of the radial electric field $E_\psi = -d\Phi/d\psi$ has been solved simultaneously according to the governing equation from Poisson's equation and the continuity equation,

$$\left[\langle|\nabla\psi|^2\rangle + 4\pi n_i m_i c^2 \left\langle \frac{|\nabla\psi|^2}{B^2} \right\rangle\right] \frac{\partial E_\psi}{\partial t} = -4\pi e \Gamma_i. \tag{5.8}$$

The intrinsic ambipolarity well-known in the standard neoclassical transport theory in tokamaks breaks by the FOW effect of ions, and E_ψ converges to the solution for Eq. (5.8) with $\Gamma_i = 0$ which gives the self-consistent ambipolar electric field[46]. In Fig. 5.3(a), the heat and energy fluxes (q_i and $q_i + 2.5\Gamma_i T_i$, respectively) calculated with or without radial electric field are shown. In both cases, one can see that the calculated energy flux is smaller than that from the standard neoclassical theory in the near-axis region $r < r_p$ as in the Lagrangian transport theory. In the case with E_ψ, the particle flux Γ_i converges to zero, and then the heat flux and the energy flux becomes almost the same value. Another effect of E_ψ is significant in a large density gradient case shown in Fig. 5.3(b). In the presence of large sheared electric field, each particle orbit is modified strongly, which is known as the orbit squeezing[36, 47]. The calculated heat flux seems to be well estimated by the standard neoclassical theory modified by the orbit squeezing factor S in Fig. 5.3(b), which represents the orbit squeezing effect on transport for conventional banana orbits. Note that the deviation of the calculation result from the modified neoclassical theory becomes large in the region $r < r_p$ as in a small gradient case. It is because the squeezing factor does not adequately express the squeezing effect of potato orbits. It is a future work to examine whether the Lagrangian transport theory can properly show the ambipolar electric field and the orbit squeezing effect or not, which is important to apply the Lagrangian transport theory for a large density gradient case as in the ITB layer.

Next, Let us see the results of experimental diagnostics of the ion thermal conductivity near the magnetic axis. The reductive tendency of χ_i in the near-axis region has already been found in the early experiments of reversed magnetic shear discharges to investigate the formation of ITB. The formation of ITB is believed to be a consequence of the suppression of microinstability and its accompanied anomalous transport by sheared $\mathbf{E} \times \mathbf{B}$ flows formed around the magnetic surface on which q-profile has a minimum point[48, 49]. When anomalous transport is suppressed, the radial transport will drop to the level predicted by neoclassical transport theory which gives the mini-

mum transport level in toroidal confinement systems. As one can see in Figs. 5.4 – 5.6, however, the observed ion thermal conductivity sometimes becomes lower than that of the standard neoclassical theory. In these figures, the position of the widest potato width r_p evaluated from the experimental data is plotted. Observed χ_i goes below the standard neoclassical level within the region $r \lesssim 1 \sim 1.5r_p$, which is the same tendency found in both the calculation using the Lagrangian transport theory in §4 and the δf simulations shown here. Note that, as one can see from Figs. 5.4 – 5.6, there seems no correlation between the position of the q_{min} surface and the position where χ_i becomes lower than the standard neoclassical level. This fact is natural because the mechanism of ITB formation is irrelevant to the modification of neoclassical transport by potato particles. It can be said that it is the factor r_p that separates the core plasma into two characteristic region concerning neoclassical transport: one is the region in which conventional neoclassical transport theory in the SOW limit is valid, and other is the region in which potato particles and its finiteness of orbit widths affect the transport. Lagrangian transport theory has proved the reductive tendency of χ_i near the magnetic axis by considering the FOW effect of potato orbits around the axis.

(W. X. Wang *et al.*, Plasma Phys. Control. Fusion **41**, 1091 (1999), Fig. 5)

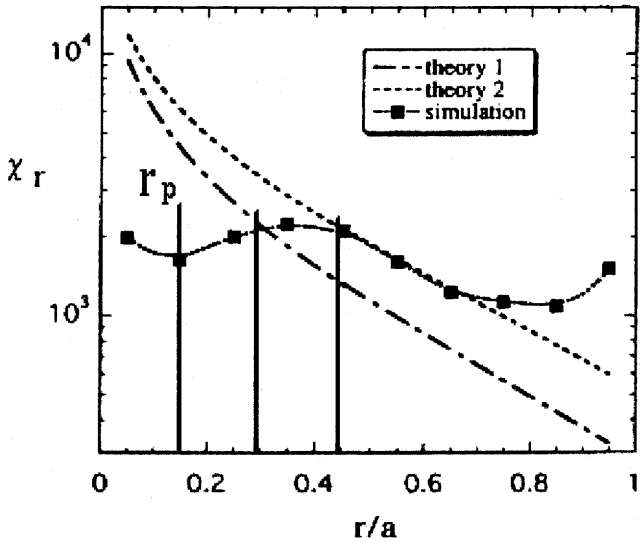

Figure 5.1: The ion thermal conductivity profile calculated by δf simulation in Ref. [16]. The blue lines are the position of r_p, $2r_p$, and $3r_p$. Two analytical evaluations of χ_i are also shown (theory 1 : Ref. [8], theory 2 : Ref. [45]).

(A. Bergmann *et al.*, Phys. Plasmas 8, 5192 (2001), Fig. 5)

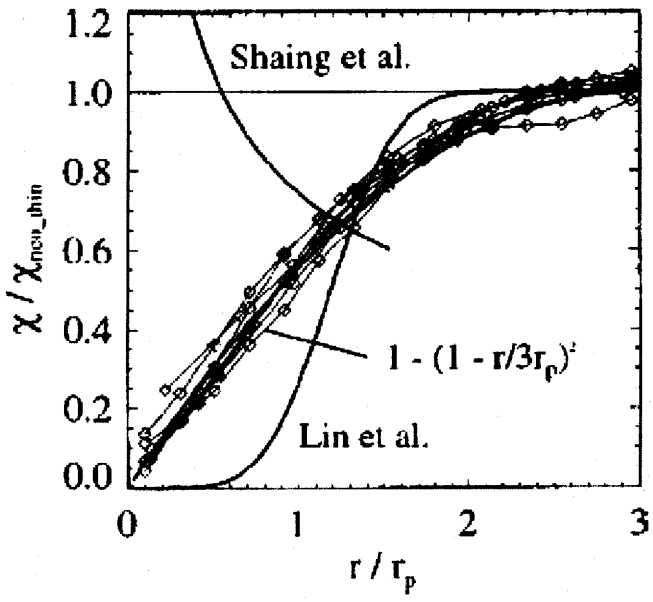

Figure 5.2: The comparison of χ_i obtained from δf simulations by Bergmann *et al.*[18] and the fitting formula for the result of Lin *et al.*[15], and the analytic solution by Shaing *et al.*[10]. χ_i is normalized by the value from the standard neoclassical theory[45], and the minor radius is normalized by r_p.

(W. X. Wang *et al.*, Phys. Rev. Lett. 87, 055002 (2001), Figs. 4 and 5)

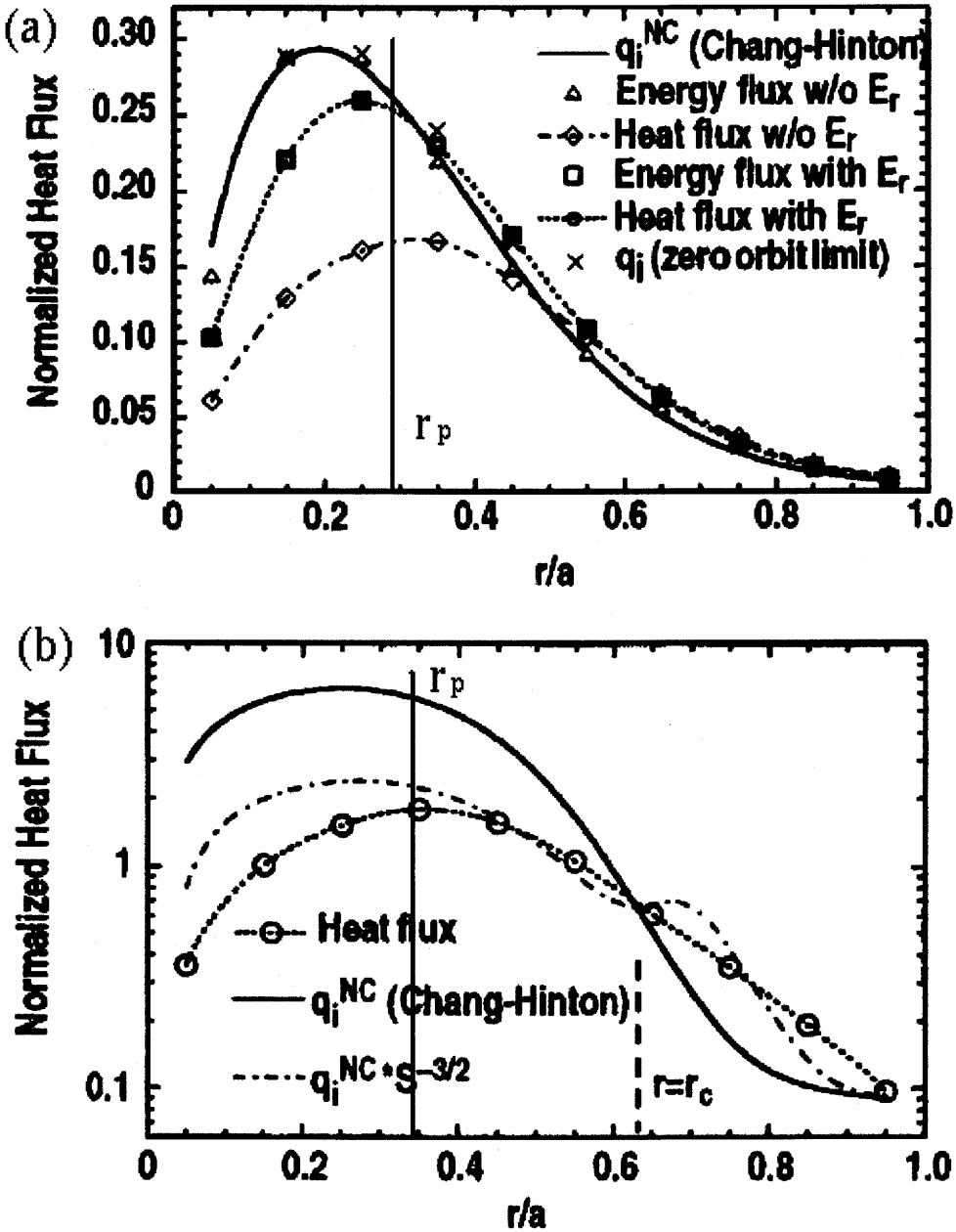

Figure 5.3: (a): Ion heat and energy fluxes obtained by the δf simulation with or without the self-consistent radial electric field for the small density gradient plasma[17]. (b): Ion heat flux for the large density gradient plasma with the radial electric field. The solid lines in the both figures are from the standard neoclassical transport theory[45], and the dotted-dashed line in Fig. (b) is the modified standard neoclassical heat flux which takes account of the orbit squeezing effect[47].

(F. M. Levinton *et al.*, Phys. Rev. Lett. 75, 4417 (1995), Fig. 5(b))

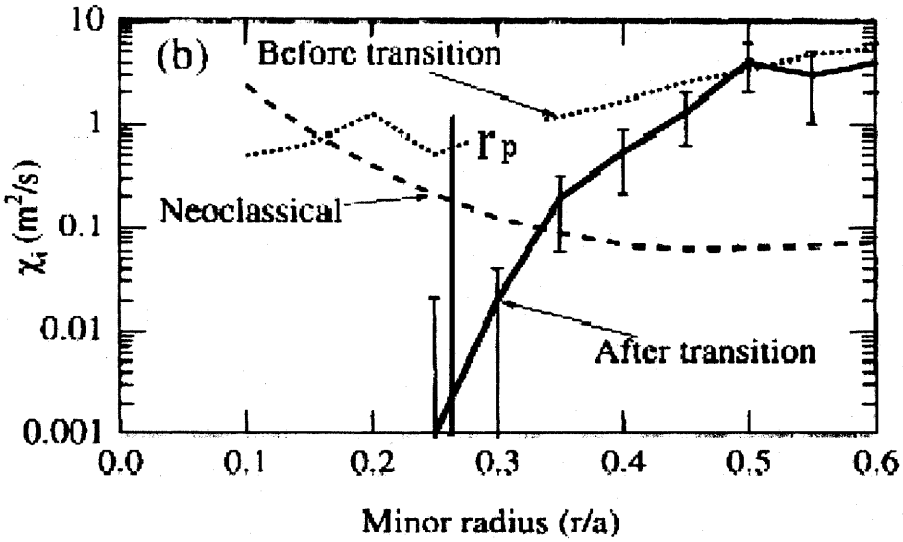

Figure 5.4: The ion thermal diffusivity profile before and after a transition into the ERS (Enhanced Reversed Shear) mode in TFTR[2]. The position of r_p is estimated by assuming $q = 3 = const$ though $q(0) \simeq 4$ and $q_{min} \simeq 2$ at $r/a = 0.35$ from the diagnostics. The dashed line is from the standard neoclassical transport theory[45].

(D. R. Baker *et al.*, Phys. Plasmas 8, 1565 (2001), Fig. 12 (c))

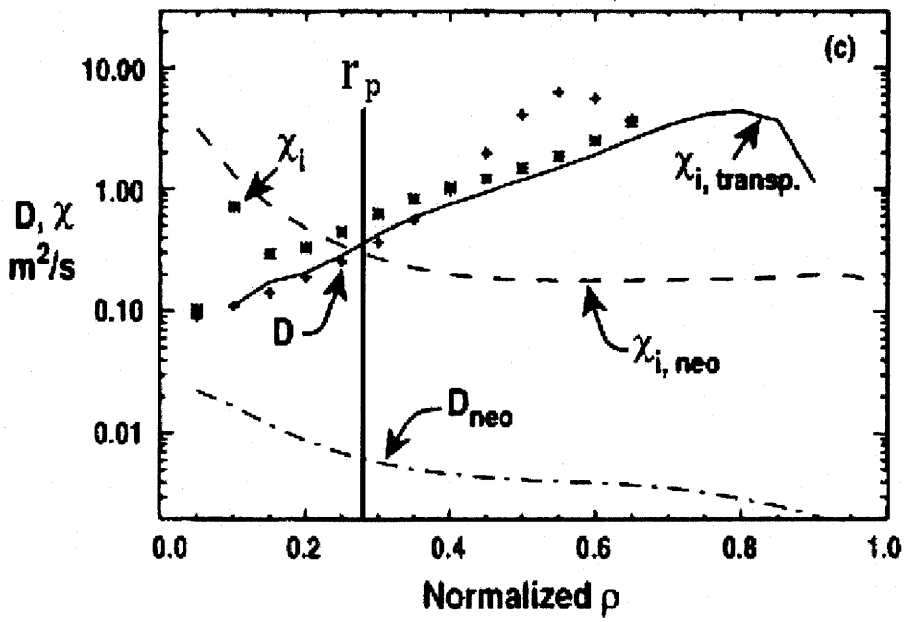

Figure 5.5: The ion thermal conductivity profile from a experiment in NCS (Negative Central magnetic Shear) discharge in DIII-D[7], which is evaluated by the TRANSP code[50]. The q-profile is almost flat in the NCS region $\rho < 0.4$, and r_p is evaluated by the approximation $q = 2$. The dashed line is from the standard neoclassical transport theory[45].

(C. M. Greenfield *et al.*, Phys. Plasmas 7, 1959 (2000), Fig. 10)

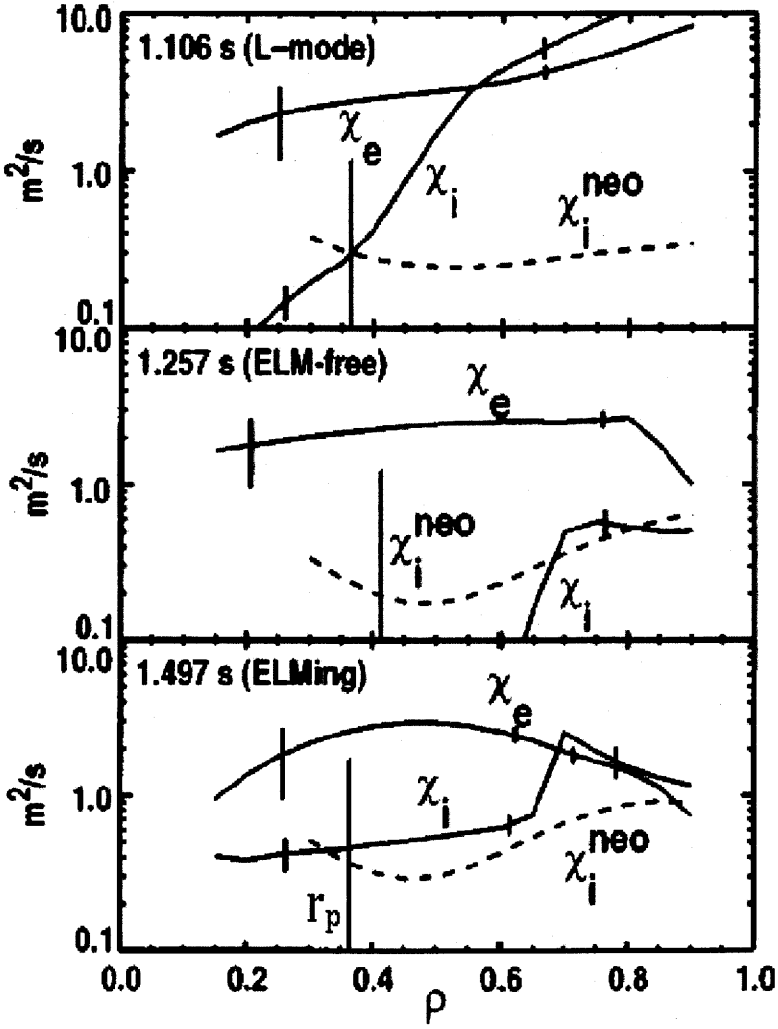

Figure 5.6: The ion thermal conductivity profile from a experiment in NCS (Negative Central magnetic Shear) discharge in DIII-D[51]. The q-profile is weakly reversed-sheared with $q(r=0) \simeq 2$ and the q_{min} surface being at $\rho \simeq 0.5$. The dashed line is from the standard neoclassical transport theory[45]. The positions of r_p plotted by the blue lines are evaluated according to the ion temperature on each time.

Chapter 6

Summary

Neoclassical transport phenomena in the region near the magnetic axis of a tokamak have been studied. First, we have shown that there appear various types of particle orbits near the magnetic axis (fat banana, kidney, inner-circulating, and outer-circulating orbits), which had not been treated properly in the conventional neoclassical transport theory. They are often called potato orbits in a generic term, which have a relatively wider orbit width $\Delta_r \sim (q^2\rho^2 R_0)^{1/3}$ than that of banana orbits appears away from the magnetic axis. We have investigated the precise properties of particle orbits and have made a clear classification for those orbits appearing around the axis.

In the near-axis region, standard neoclassical transport theory based on the small-orbit-width (SOW) approximation is not valid because the finiteness of potato orbits affects significantly the transport near the magnetic axis in a low-collisionality plasma. To construct a new transport theory applicable to this region, we have adopted Lagrangian approach of neoclassical transport analysis. Comparing to the conventional Eulerian approach, the Lagrangian formulation contains the finite-orbit-width (FOW) effect by nature, in which both the properties of wide-width particle orbits and information of the background field along each orbit are reflected.

Though the Lagrangian transport theory had been proposed to treat nonlocal transport phenomena in a low-collisionality plasma, the previous works had only proved that the Lagrangian transport theory could reproduce the result of the standard Eulerian transport theory away from the axis. It is because there had been a difficulty in application of this approach in practice to a case in which the FOW effect is really important as in the near-axis region. Then, we have improved the treatment of the orbit-averaged self-collision term by introducing a model collision operator which is suitable to both analytical formulation and numerical calculation. By using the model collision operator, we have solved the reduced drift kinetic equation in the phase space of the constants of

motion (COM) $(\mathcal{E}, \mu, \langle\psi\rangle)$, and have obtained the Lagrangian transport equations which is valid both in the regions near and away from the magnetic axis.

To utilize the Lagrangian formulation to calculate transport coefficients near the magnetic axis, we have developed the numerical calculation code (the NEO code) using a Monte Carlo integration method which can correctly evaluate the transport coefficients with the FOW effect. It has been shown that the resultant ion thermal conductivity χ_i is smaller than that obtained from the standard neoclassical transport theory in the region $\langle r\rangle < r_p = 2(2q^2\rho^2 R_0)^{1/3}$ in a constant-q configuration. We have also shown that the direct comparison of χ_i between Eulerian and Lagrangian representations is possible as long as the factor λ_q is nearly unity, which is the case in the region $\langle r\rangle > q\rho$. As concerning the q-profile, we have demonstrated that the region in which the reduction of χ_i from the standard neoclassical level is seen becomes broader as the typical potato orbit width r_p becomes wider in a reversed magnetic shear configuration, in which q-factor near the magnetic axis is larger than in a normal shear configuration. We have found that the reductive tendency of χ_i in the range $\langle r\rangle < r_p$ is consistent with the results of recent tokamak experiments and other transport simulations using δf method. Thus it has been shown that the Lagrangian neoclassical transport theory gives one a correct and useful method to treat the transport phenomena including the FOW effect in the near-axis region.

Finally, let us remark on some subjects on the Lagrangian approach of the transport analysis in future. First, in the calculation of transport coefficients shown in this thesis, we have neglected the radial electric field. However, it has been shown in the recent δf simulations that the FOW effect produces non-vanishing ion particle flux in the radial direction even if only the ion-ion self-collisions are considered, and the ambipolar radial electric field can be determined as in non-axisymmetric systems such as stellarators. On the other hand, the presence of the radial electric field affects the transport by modifying the population of each orbit type and the orbit width by the orbit-squeezing effect. Therefore, an iterative calculation is needed to obtain the self-consistent radial electric field in the NEO code, which takes much calculation time. In this point of view, the direct simulation using δf method is convenient to calculate neoclassical fluxes with the self-consistent electric field. However, one advantage in the Lagrangian approach over δf simulation is that one can evaluate separately the contribution of the diagonal and off-diagonal components of the transport matrix on the neoclassical fluxes. Therefore, the Lagrangian transport theory will help our understanding of neoclassical transport phenomena in a realistic configuration in which both the density and temperature gra-

dients are present.

Another point is the consideration of the external sources of the particle, momentum, and energy. In the formation of the reversed shear configuration with ITB in experiments, it is known that some strong heatings on the core plasma are needed. Therefore, for utilizing the Lagrangian formulation to analyze the core transport of plasma with ITB, the source terms must be considered for completeness.

We will further investigate transport phenomena near the magnetic axis by using both the Lagrangian transport analysis and the δf method, and then contribute to a more comprehensive understanding of neoclassical transport with the FOW effect.

Appendix A

Estimation of δ_*

From the definition of δ_*, we have to evaluate

$$\delta_* = \left(\frac{\partial}{\partial \psi} + \frac{\partial \theta^*}{\partial \langle \psi \rangle} \frac{\partial}{\partial \theta} \right) \alpha_*, \tag{A.1}$$

where $\alpha_* = I v_\parallel / \Omega$ evaluated at the averaging point $(\psi, \theta) = (\langle \psi \rangle, \theta^*)$. The difficulty lies in the evaluation of $\partial \theta^* / \partial \langle \psi \rangle$. First, let us consider the case for orbits which have the turning points of $\dot{\theta}$, that is, for banana, concave-kidney, outer-circulating, and inner-circulating orbits. The averaging point of these orbits can be approximated by the turning points. Therefore, from the equation of $\dot{\theta}$ in Eq. (3.16), $\partial \alpha_* / \partial \psi = 1$ must be satisfied on the averaging point. Then, we have

$$\frac{\partial \theta^*}{\partial \langle \psi \rangle} \simeq - \frac{\dfrac{\partial}{\partial \psi} \left(\dfrac{\partial \alpha_*}{\partial \psi} \right)}{\dfrac{\partial}{\partial \theta} \left(\dfrac{\partial \alpha_*}{\partial \psi} \right)}. \tag{A.2}$$

Substituting Eq. (A.2) into (A.1), we have

$$\delta_* = \frac{m v_\parallel^2 \left(\dfrac{\partial B}{\partial \psi} \dfrac{\partial^2 B}{\partial \psi \partial \theta} - \dfrac{\partial B}{\partial \theta} \dfrac{\partial^2 B}{\partial \psi^2} \right)}{m v_\parallel^2 \dfrac{\partial B}{\partial \psi} \dfrac{\partial^2 B}{\partial \psi \partial \theta} + \mu \dfrac{\partial B}{\partial \theta} \left(\dfrac{\partial B}{\partial \psi} \right)^2 \left(\dfrac{\mu B}{\mu B + m v_\parallel^2} - \dfrac{2 m v_\parallel^2}{\mu B} \right)}. \tag{A.3}$$

Note that Eq. (A.3) is evaluated at the averaging point. Since $v_\parallel \simeq 0$ at the turning point of $\dot{\theta}$, one can see that $\delta_* \simeq 0$ for banana and outer-, inner-circulating orbits. As concerns kidney orbits, we can evaluate $\partial \theta^* / \partial \langle \psi \rangle$ by approximating the averaging point by the turning point of $v_\parallel$. Then one also finds that δ_* can be neglected for kidney orbits.

For passing particles, we cannot determine the averaging point θ^* in a simple way as above. However, for well-passing particles, $\partial \theta^* / \partial \langle \psi \rangle$ in Eq. (A.1) can be negligible,

and one can estimate

$$\delta_* \simeq \frac{\partial \alpha_*}{\partial \psi} \sim \alpha_* \frac{1}{B} \frac{\partial B}{\partial \psi} \sim \frac{q\rho}{\langle r \rangle}, \tag{A.4}$$

which is negligible when considering $\langle r \rangle \sim r_p \gg q\rho$.

Thus the approximation $1 - \delta_* \simeq 1$ is ensured for all types of orbit.

Appendix B

Derivation of the lowest order distribution function

Here, the procedure of deriving the $O(\delta_b^0)$-th distribution function $\bar{f}_0$ is explained. This is an intelligible example for readers to understand how to take a moment in the $(\mathcal{E}, \mu)$ space.

Instead of the model collision operator Eq. (3.33), the exact operator (3.24) is used in the reduced drift kinetic equation of the $O(\delta_b^0)$ part,

$$\bar{C}^{(0)}(\bar{f}_0) = \frac{1}{J_c}\frac{\partial}{\partial \mathbf{z}} \cdot \left[J_c \left(\mathbf{A}\bar{f}_0(\mathbf{z}) + \mathsf{D} \cdot \frac{\partial}{\partial \mathbf{z}} \bar{f}_0(\mathbf{z}) \right) \right] = 0, \tag{B.1}$$

where $\mathbf{A}$ and D are defined in Eq. (3.25). Note that the derivative $\partial/\partial \mathbf{z}$ is treated as $\partial/\partial\mathcal{E}$ or $\partial/\partial\mu$ here and hereafter, because $\partial/\partial\langle\psi\rangle$ is assumed to be $O(\delta_b^1)$. Multiplying $J_c \ln \bar{f}_0$ and integrating in the $(\mathcal{E}, \mu)$ plane, one has

$$\begin{aligned} 0 \;=\; & \sum_{\sigma_t} \int d\mathcal{E} d\mu \frac{\partial}{\partial \mathbf{z}} \cdot \left[J_c \ln \bar{f}_0 \left(\mathbf{A}\bar{f}_0 + \mathsf{D} \cdot \frac{\partial}{\partial \mathbf{z}} \bar{f}_0 \right) \right] \\ & - \frac{2\pi K}{m^2} \sum_{\sigma_t} \int \tau_p |1 - \delta_*| d\mathcal{E} d\mu J_c \frac{\partial}{\partial \mathbf{z}} \ln \bar{f}_0 \frac{1}{\tau_p} \int d\phi \oint_{orb} \frac{d\theta}{\dot{\theta}} \int d^3v' \bar{f}_0(\mathbf{z}) \bar{f}_0'(\mathbf{z}') \\ & \times \frac{\partial \mathbf{z}}{\partial \mathbf{v}} \cdot \mathsf{U}(\mathbf{v} - \mathbf{v}') \cdot \left(\frac{\partial \mathbf{z}}{\partial \mathbf{v}} \cdot \frac{\partial}{\partial \mathbf{z}} \ln \bar{f}_0 - \frac{\partial \mathbf{z}'}{\partial \mathbf{v}'} \cdot \frac{\partial}{\partial \mathbf{z}'} \ln \bar{f}_0' \right), \end{aligned} \tag{B.2}$$

where the partial integral has been performed, and the orbit averaging operator and the Jacobian J_c are explicitly written down in the second term.

Physically, collisions bring about random scatterings of particles in the $(\mathcal{E}, \mu, \langle\psi\rangle)$ space. We should note here that there is a limitation in $(\mathcal{E}, \mu, \langle\psi\rangle)$ space within which particles can exist. Then, the random-walk of particles by collisions is limited within this existence region, and no particle can cross the boundary. Therefore, the vector $\mathbf{A}\bar{f}_0 + \mathsf{D} \cdot \partial\bar{f}_0/\partial\mathbf{z}$ in the first term of Eq. (B.2) must be parallel to the boundary in

the $(\mathcal{E}, \mu, \langle\psi\rangle)$ space, and thus the first term vanishes. (See also Appendix. C for more details of the integral region in the $(\mathcal{E}, \mu)$ plane.)

As mentioned in §3.2.3, $\mathbf{z}'$ can be written as $\mathbf{z}' = (\mathcal{E}', \mu', \langle\psi\rangle' = \langle\psi\rangle + \tilde{\psi}')$. In the lowest order, the deviation $\tilde{\psi}'$ can be neglected. By using this approximation, the integral $\int d^3v'$ is transformed to the $(\mathbf{z}, \tilde{\mathbf{z}})$ space as

$$\int d^3v' = \mathbf{b} \cdot \nabla\theta \int d\mathcal{E}' d\mu' d\phi' d\theta' d\zeta' d\langle\psi\rangle' \frac{|1-\delta_*'|}{m^2|\dot{\theta}'|} \delta(\theta'-\theta)\delta(\zeta'-\zeta)\delta(\langle\psi\rangle'-\langle\psi\rangle), \quad \text{(B.3)}$$

where we have used Eq. (3.17) for the Jacobian in the $(\mathbf{z}, \tilde{\mathbf{z}})$ space.

Substituting Eq. (B.3), and changing the order of integration $\int d\theta$, we have

$$\begin{aligned} &\int_0^{2\pi} d\theta \sum_{\sigma_t, \sigma_t'} \int \mathbf{b} \cdot \nabla\theta d\mathcal{E} d\mu d\phi \\ &\times \int d\mathcal{E}' d\mu' d\phi' \frac{|1-\delta_*|}{|\dot{\theta}|} \frac{|1-\delta_*'|}{|\dot{\theta}'|} \bar{f}_0 \bar{f}_0' \frac{\partial}{\partial \mathbf{z}} \ln \bar{f}_0 \cdot \frac{\partial \mathbf{z}}{\partial \mathbf{v}} \cdot \mathsf{U} \cdot \mathbf{F} = 0, \end{aligned} \quad \text{(B.4)}$$

where

$$\mathbf{F}(\mathbf{v}, \mathbf{v}', \langle\psi\rangle) \equiv \frac{\partial \mathbf{z}}{\partial \mathbf{v}} \cdot \frac{\partial}{\partial \mathbf{z}} \ln \bar{f}_0(\mathbf{z}) - \frac{\partial \mathbf{z}'}{\partial \mathbf{v}'} \cdot \frac{\partial}{\partial \mathbf{z}'} \ln \bar{f}_0'(\mathbf{z}'). \quad \text{(B.5)}$$

Interchanging $(\mathcal{E}, \mu)$ with $(\mathcal{E}', \mu')$ in Eq. (B.4) and combining the resultant equation with the original one, we have

$$0 = \int_0^{2\pi} d\theta \sum_{\sigma_t, \sigma_t'} \int \mathbf{b} \cdot \nabla\theta d\mathcal{E} d\mu d\phi \int d\mathcal{E}' d\mu' d\phi' \frac{|1-\delta_*|}{|\dot{\theta}|} \frac{|1-\delta_*'|}{|\dot{\theta}'|} \bar{f}_0 \bar{f}_0' \mathbf{F} \cdot \mathsf{U} \cdot \mathbf{F}. \quad \text{(B.6)}$$

From the definition of U one finds

$$\mathbf{F} \cdot \mathsf{U}(\mathbf{w}) \cdot \mathbf{F} = \frac{1}{w^3} \left[(Fw)^2 - (\mathbf{F} \cdot \mathbf{w})^2 \right] \geq 0, \quad \text{(B.7)}$$

where $\mathbf{w} = \mathbf{v} - \mathbf{v}'$. The equality is satisfied only when $\mathbf{F}$ and $\mathbf{w}$ are parallel. Therefore, from Eq. (B.6), $\mathbf{F}$ must satisfy

$$\mathbf{F} \times (\mathbf{v} - \mathbf{v}') = 0 \quad \text{(B.8)}$$

for any $(\mathbf{v}, \mathbf{v}')$. Considering the case of $\mathbf{v}' = 0$ yields

$$\begin{aligned} \mathbf{F} \times \mathbf{v} &= m \left(\mathbf{v} \frac{\partial}{\partial \mathcal{E}} - \frac{\mathbf{v}_\perp}{B} \frac{\partial}{\partial \mu} \right) \ln \bar{f}_0 \times \mathbf{v} = 0 \\ &\Leftrightarrow \frac{\partial}{\partial \mu} \ln \bar{f}_0 = 0. \end{aligned} \quad \text{(B.9)}$$

Then $\bar{f}_0$ is independent of μ. Returning to Eq. (B.8), one has

$$
\begin{aligned}
& (\mathbf{v}-\mathbf{v}') \times (\mathbf{v}\frac{\partial}{\partial \mathcal{E}} \ln \bar{f}_0 - \mathbf{v}'\frac{\partial}{\partial \mathcal{E}'} \ln \bar{f}_0') = 0 \\
\Leftrightarrow \quad & (\mathbf{v} \times \mathbf{v}')(\frac{\partial}{\partial \mathcal{E}} \ln \bar{f}_0 - \frac{\partial}{\partial \mathcal{E}'} \ln \bar{f}_0') = 0 \\
\Leftrightarrow \quad & \frac{\partial}{\partial \mathcal{E}} \ln \bar{f}_0 = -\frac{1}{T(\langle\psi\rangle)}.
\end{aligned}
\tag{B.10}
$$

Therefore, one finds $\bar{f}_0 = N(\langle\psi\rangle)\exp(-\mathcal{E}/T)$. By considering radial electric field $\Phi(\psi)$, we must change integral variable $\mathcal{E}$ with $W = \mathcal{E} - e\Phi(\psi = \langle\psi\rangle)$. The same procedure from Eq. (B.2) yields the zero-th order distribution function

$$
\bar{f}_0(\mathcal{E}, \mu, \langle\psi\rangle) = \bar{n}(\langle\psi\rangle)\left(\frac{m}{2\pi T(\langle\psi\rangle)}\right)^{3/2} \exp\left[-\frac{\mathcal{E} - \Phi(\langle\psi\rangle)}{T(\langle\psi\rangle)}\right], \tag{B.11}
$$

where the normalized factor $N = \bar{n}(m/2\pi T)^{3/2}$ is defined so that Eq. (B.11) reproduce the local Maxwellian f_M in the SOW limit of the standard Eulerian theory.

Appendix C

Integral in the $(\mathcal{E}, \mu)$ plane

In the derivation of transport equations, integrals in the $(\mathcal{E}, \mu)$ plane appear. We prove some properties used in the integral here. Consider an integral of a function F

$$\sum_{\sigma_t} \int d\mathcal{E} \int d\mu J_c(\mathcal{E}, \mu, \langle\psi\rangle; \sigma_t) F(\mathcal{E}, \mu, \langle\psi\rangle; \sigma_t), \tag{C.1}$$

where J_c and F also depend on the orbit type σ_t. Integral region in the μ direction is shown in Fig. C.1. μ_1, μ_2 and μ_3 correspond to the boundaries $l1$, $l2$ and $l3$ in Fig. 2.11, respectively. The kidney region is laid between μ_2 and μ_3, and it is overlapped with a part of the banana and co-passing regions. The integral path in μ is taken in the direction of arrows in Fig.C.1.

To use Gauss's theorem to take moments of the reduced kinetic equation (3.55), some boundary conditions are needed. First, consider the boundary $\mu = 0$. Here, noting that all the integrand having the form $\partial/\partial\mu$ in Eq. (3.55) are proportional to μ. Then the surface integral vanishes there. Second, consider the boundary μ_3, where a co-passing particle moves into a kidney region. This transition occurs continuously, since the difference between kidney and co-passing orbits is only that the former has turning point of $v_\parallel$ and the latter does not. Then, we have

$$\lim_{\mu \to \mu_3} J_c(\mu; \sigma_t = P+) = \lim_{\mu \to \mu_3} J_c(\mu; \sigma_t = K). \tag{C.2}$$

Therefore, the surface integral is canceled at μ_3 between co-passing and kidney, since any physical value in the integrand F is also continuous on the boundary.

On the boundary μ_2, a banana particle bifurcates into a kidney or a counter-passing particle as shown in Fig. 2.12. At the limit $\mu = \mu_2$, the particle is stagnated at $(r, \theta) = (\langle r\rangle, \pi)$. All the values contained in the integrand F are then evaluated at the stagnation point. On the other hand, Jacobian J_c becomes infinity at μ_2 as is pointed

out in Sec. §3.2. Noting that the kidney and counter-passing orbit at the boundary correspond to outer- and inner-sections of a banana orbit and $J_c \propto \tau_p$, we have

$$\lim_{\mu\to\mu_2} J_c(\mu;\sigma_t = B) = \lim_{\mu\to\mu_2} \left[J_c(\mu;\sigma_t = K) + J_c(\mu;\sigma_t = P-)\right]. \tag{C.3}$$

Therefore, the integrand F for each orbit type are required to be continuous on the boundary so that the surface integral on the boundary μ_2 can be canceled between banana, counter-passing and kidney, otherwise the integral will diverge.

The last condition is on the $\mu = \mu_1$ corresponding to stagnated outer-circulating orbits. In Eq. (3.55), one can see that all the terms within the $\partial/\partial\mu$ operator have $v_\parallel$ in the averaged operator $\langle\cdots\rangle$. As mentioned in §2.2, $v_\parallel$ is not exactly zero for the stagnated outer-circulating orbits when particle orbits are solved strictly. Then, there remains a small contribution from the surface integral in the μ direction when one takes the moment of Eq. (3.55) to obtain Eqs. (3.56) and (3.60). Strictly speaking, however, this contribution must be vanished since no particle can go across the boundary μ_1 in the COM space as pointed out in Appendix. B, and in fact it vanishes in the SOW limit, since stagnated condition is $v_\parallel = 0$ in this limit. The small contribution on the μ_1 boundary may remain because we solve the drift kinetic equation order by order. Therefore, the contribution from the surface integral to $\partial\mathcal{N}_i/\partial t$ and $\partial\mathcal{Q}_i/\partial t$ is considered to be of the order higher than $O(\delta_b^2)$, and then it is negligible.

As a consequence, the perturbed distribution function g_k must have continuous derivative $\partial g_k/\partial\mu$ on the boundary μ_2 and μ_3. This fact is used in Eq. (3.77).

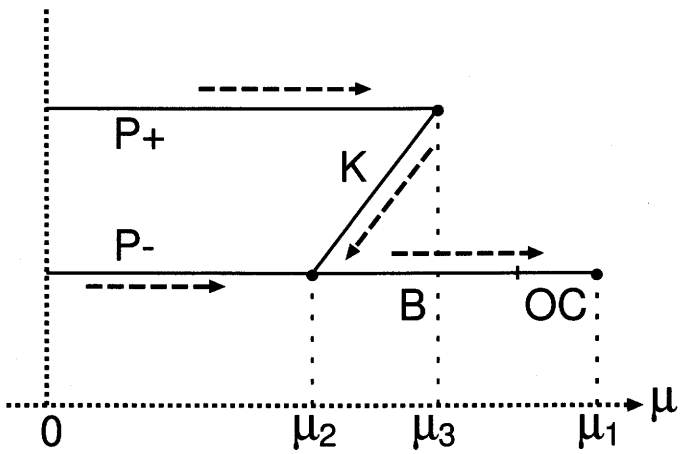

Figure C.1: Integral path in the μ direction. Abbreviations of orbit types are the same as used in Fig. 2.11.

Appendix D

Transport coefficients in the SOW limit

To show that the particle flux J_1^i vanishes in the SOW limit, consider the transport coefficients $\bar{S}_{11}$ and $\bar{S}_{33}^{im}$ away from the magnetic axis. We assume a model magnetic field $B = B_0(1 - \epsilon\cos\theta)$ as in Sec. II. Orbit types considered here are passing and banana in a usual sense, and the factor $|1 - \delta_*|$ becomes unity in this limit. From the definition of the normalized transport coefficients Eqs. (3.78) and (3.80), one has

$$\bar{S}_{33} = \bar{S}_{11} + \sum_{\sigma_t} \int dx d\lambda_0 \bar{\tau}_p c_i y(c) \lambda_0 \langle h \rangle. \tag{D.1}$$

Since $\dot{\theta} = v_\parallel \mathbf{b} \cdot \nabla\theta$ in the SOW limit, the integral above can be calculated as

$$\begin{aligned} \sum_{\sigma_t} \int dx d\lambda_0 \bar{\tau}_p c_i y(c) \lambda_0 \langle h \rangle &= \sum_{\sigma_t} \frac{2v_{thi}}{qR_0} \int_0^\infty dc c_i^2 \exp^{-c_i^2} y(c) \int_0^{1+\langle\epsilon\rangle} d\lambda_0 \lambda_0 \oint \frac{d\theta}{v_\parallel \mathbf{b} \cdot \nabla\theta} \frac{B_0}{B} \\ &= \sum_{\sigma_\parallel} \frac{2B_0}{qR_0} \mathcal{K}_1 \int_0^{2\pi} \frac{d\theta}{\mathbf{B} \cdot \nabla\theta} \int_0^h d\lambda_0 \frac{\lambda_0}{\sqrt{1 - \lambda_0/h}}. \end{aligned}$$

Therefore, we obtain

$$\bar{S}_{33} = \bar{S}_{11} + \frac{8B_0\mathcal{K}_1}{3\pi qR_0} \frac{dV}{d\psi} \langle h^2 \rangle_\psi, \tag{D.2}$$

where we have used the flux-surface average

$$\langle h^2 \rangle_\psi = \frac{1}{2\pi} \frac{dV}{d\psi} \int_0^{2\pi} \frac{d\theta}{\mathbf{B} \cdot \nabla\theta} h^2.$$

Combining Eqs. (3.81) and (D.2) yields

$$\bar{\beta} = \bar{S}_{11}^{-1}. \tag{D.3}$$

Since $A_{11} \propto \bar{S}_{11}(1-\bar{\beta}\bar{S}_{11})$ and $A_{12} \propto \bar{S}_{12}(1-\bar{\beta}\bar{S}_{11})$, the transport matrix components A_{jk} other than A_{22} vanish intrinsically. Therefore, ion particle flux does not appear in the Lagrangian formulation in the SOW limit when only the ion-ion collision is considered.

Note here that, in the SOW limit, Eq.(3.78) for $\bar{S}_{jk}$ becomes the same form as Eq. (80) in Ref. [52] since $\langle hv_{\|}\rangle = 0$ for bananas in this limit. Then, the ion thermal conductivity obtained from our formulation reproduces the result from the Eulerian formulation in the SOW limit. Though this property has already been proved by Bernstein *et* al, we succeed in introducing the momentum-conservation nature in the Lagrangian formulation.

Appendix E

Relation between the particle distributions in Lagrangian and Eulerian representations

In Lagrangian formulation, definitions of the particle density and the temperature are different from those in Eulerian representation. In §3.3.1, it is that $\bar{n}_i(\langle\psi\rangle) \simeq n_i(\psi)$ even in the near-axis region. Here we discuss the relation between two representations and show some examples of the density and the temperature profiles by numerical calculation.

The distribution function in the COM space $\bar{f}(\mathcal{E}, \mu, \langle\psi\rangle)$ can be understood as[53]

$$\begin{aligned} \bar{f}(\mathcal{E}, \mu, \langle\psi\rangle) &= \langle f(\mathcal{E}, \mu, \psi, \theta)\rangle \\ &= \frac{1}{\tau_p} \oint \frac{d\theta}{\dot{\theta}} f[\mathcal{E}, \mu, \psi(\mathcal{E}, \mu, \langle\psi\rangle, \theta), \theta], \end{aligned} \tag{E.1}$$

where $f(\mathcal{E}, \mu, \psi, \theta)$ is the usual distribution function in the Eulerian representation. By differentiating the both sides along the particle orbit, one easily finds the inverse relation

$$f(\mathcal{E}, \mu, \psi, \theta) = \bar{f}[\mathcal{E}, \mu, \psi - \Delta_\psi], \tag{E.2}$$

where Δ_ψ is defined in Eq. (3.68).

In the Lagrangian transport theory, the lowest-order distribution function $\bar{f}_0$ is given by Maxwellian in the COM space

$$\bar{f}_0 = \bar{n} \left(\frac{m}{2\pi T}\right)^{3/2} \exp\left[-\frac{\mathcal{E} - e\Phi}{T}\right], \tag{E.3}$$

where $\bar{n}$, T, and Φ are given as functions of $\langle\psi\rangle$. Using Eq. (E.2), we can calculate the particle density $n_E(\psi, \theta)$ and the temperature $T_E(\psi, \theta)$ in the usual Eulerian representation when the plasma particles are loaded according to the distribution function in

the COM space. They are given as

$$n_E(\psi,\theta) = \int d^3v \bar{f}_0(\mathcal{E},\mu,\psi-\Delta_\psi), \tag{E.4a}$$

$$T_E(\psi,\theta) = \frac{2}{3n_E}\int d^3v \mathcal{E}\bar{f}_0(\mathcal{E},\mu,\psi-\Delta_\psi), \tag{E.4b}$$

where we neglect the perturbed distribution $\bar{f}_1$, $\bar{f}_2$, $\cdots$ for the simplicity. From these equations, it is expected that

$$\left.\frac{n_E(\psi,\theta)}{\bar{n}(\langle\psi\rangle)}\right|_{\psi=\langle\psi\rangle} \sim \left.\frac{T_E(\psi,\theta)}{T(\langle\psi\rangle)}\right|_{\psi=\langle\psi\rangle} \sim O(\delta_b^0) \tag{E.5}$$

with δ_b being the ordering parameter of the gradient scale length of $\bar{n}$ and T defined in Eq. (3.41). Therefore, as we assumed in the main text, the the differences of the density and the temperature between Lagrangian and Eulerian representations are expected to be small as long as the assumption $\delta_b \ll 1$ is valid.

Now we show some numerical calculation results of n_E and T_E. The numerical method used here is similar to the Monte Carlo integration shown in §4. Test particles are randomly generated in the phase space $(\mathcal{E},\mu,r,\theta)$, and then the averaged position $\langle r\rangle$ of each particle is calculated by tracing the orbit. From given $\bar{n}(\langle r\rangle)$ and $T(\langle r\rangle)$, the integrand in Eqs. (E.4a) and (E.4b) are evaluated.

The first example is for the small gradient case $\delta_b \ll 1$ with a constant-q profile($q = 3$). The profiles of $\bar{n}_i$ and T_i are given as the same as in Fig. 4.6 with $\bar{n}_i(0) = 5\times10^{19}m^{-3}$ and $T_i(0) = 10keV$. The typical potato width r_p defined in Eq. (2.43) is about $0.20m$ in this profile. Figure E.1 is the numerical calculation results of n_E and T_E. Only a slight difference can be seen in the density and temperature profiles between the Eulerian and the Lagrangian representations, that is, $\bar{n}(\langle r\rangle) \simeq n_E(r = \langle r\rangle,\theta)$ and $T(\langle r\rangle) \simeq T_E(r = \langle r\rangle,\theta)$. Then, the assumption made in §3.3.1 on $\bar{n}_i(\langle\psi\rangle)$ is confirmed, even in the region $r \sim q\rho_i$ where λ_n and λ_q becomes much larger than unity.

We also check the particle distribution in the velocity space $(v_\parallel, v_\perp)$ in the Eulerian representation. In the small gradient case, the calculated distribution function $f(r,\theta,v_\parallel,v_\perp)$ almost resembles the local Maxwellian. A distinctive feature can be seen as the gradient becomes steeper. We calculate the particle distribution in a reversed magnetic shear configuration as in Fig. 4.6 with more steep gradients for $\bar{n}$ and T than those given in the previous case. In this case, δ_b for typical potato particles is about 0.5. Even in this case, calculated n_E and T_E are almost the same as given $\bar{n}$ and T. However, as shown in Fig. E.2, the distribution function shows a remarkable asymmetry with $v_\parallel$. In Fig. E.2(a), negative-$v_\parallel$ particles in the range $|v_\parallel/v| \lesssim \sqrt{\epsilon}$ draw banana orbit with $\langle r\rangle > r$, while $\langle r\rangle < r$ for positive-$v_\parallel$ bananas. Then particle density in the negative-$v_\parallel$

region becomes smaller than that in the positive-$v_{\|}$ region. A similar explanation can be given for the asymmetry in Fig. E.2(b) by considering the average position for co- and counter-passing orbits.

The asymmetry of the particle distribution in the velocity space shows the non-locality essentially contained in Lagrangian representation, and gives the physical description how the explicit part of transport is driven in the Lagrangian formulation. In the conventional Eulerian transport theory, the lowest order distribution function is given by a local Maxwellian, and then it bears no particle and thermal fluxes. On the other hand, in the Lagrangian formulation, the lowest order distribution function $\bar{f}_0$, which is Maxwellian in the COM space, gives an asymmetric distribution in the velocity space on a local point. Then the pitch-angle scattering term in the model collision operator (the first term in Eq. (3.26)) brings about a flux in the velocity space which flows from the high-density side toward the low-density side. In Fig. E.2(a) for example, the positive-$v_{\|}$ banana particles diffuse into the negative-$v_{\|}$ region and consequently change their averaged position $\langle\psi\rangle$ outward. Thus the explicit part of the fluxes in the $\langle\psi\rangle$ direction are arisen from the lowest order distribution $\bar{f}_0$.

Note here that we have neglected the perturbation of the particle distribution $\bar{f}_1$ in the numerical calculation of n_E and T_E, and that there also exist the implicit part of the fluxes which are determined from $\bar{f}_1$. The main role of the implicit part in the Lagrangian formulation is to cancel the particle flux Γ_i through S_{33}^{im}, which acts as the momentum restoring term for the pitch angle scattering operator.

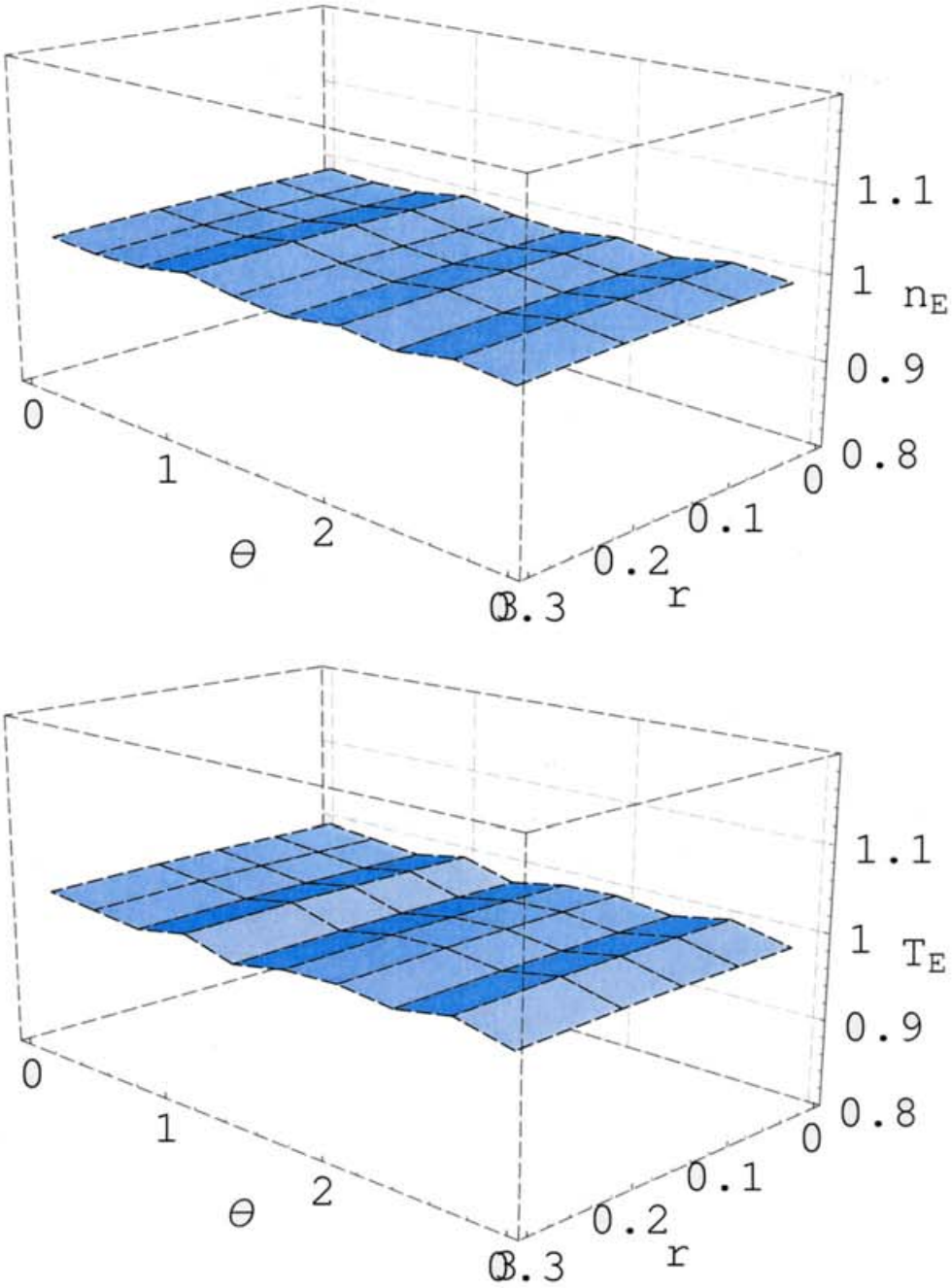

Figure E.1: Profiles of the ion density n_E and the temperature T_E in the usual Eulerian representation for a small gradient configuration. n_E and T_E are normalized by $\bar{n}(0)$ and $T(0)$, respectively.

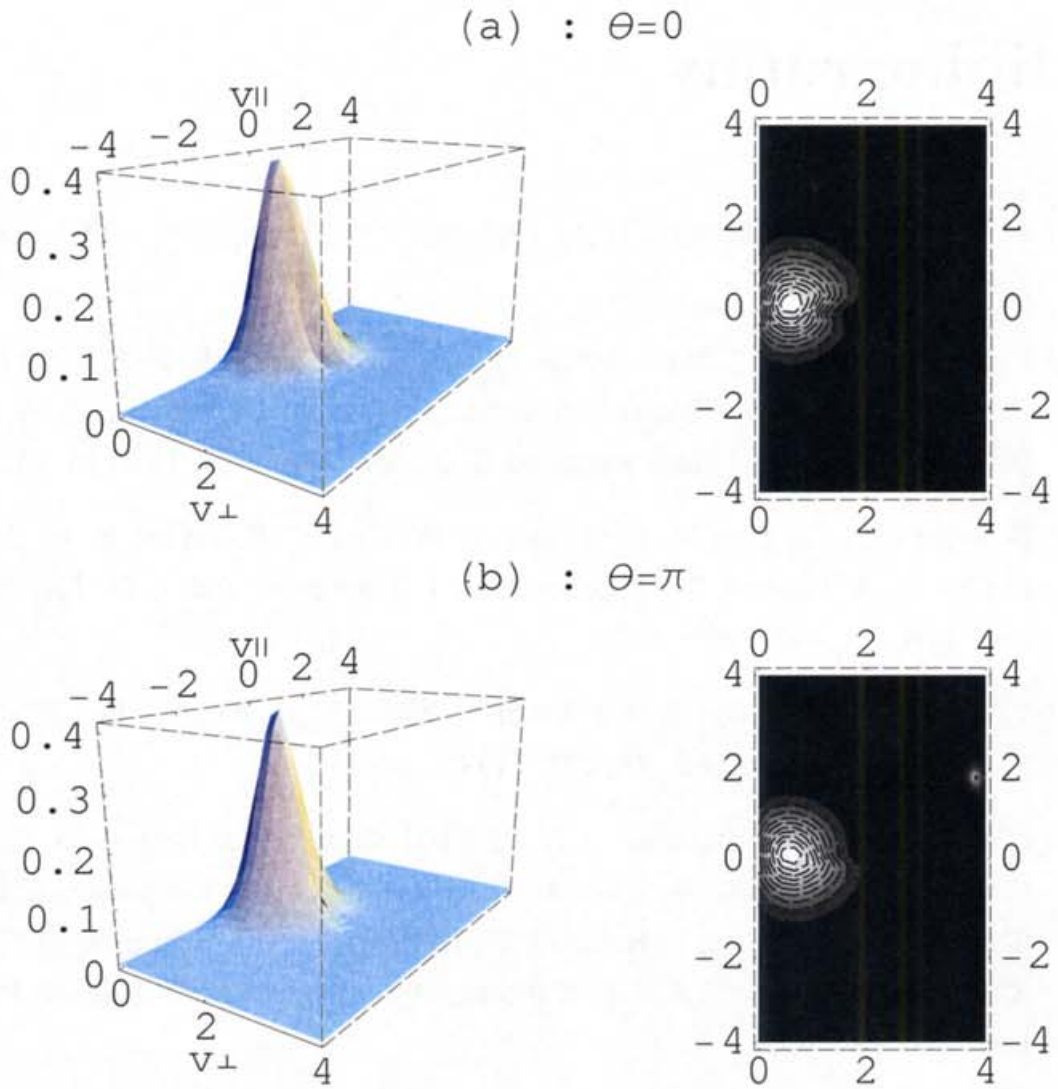

Figure E.2: Particle distribution function $f(v_\parallel, v_\perp)$ at (a) : $\theta = 0$ and (b) : π on $r = 0.10m$ in a large gradient configuration. The scales $v_\parallel$ and $v_\perp$ are normalized by v_{th}. A remarkable asymmetry can be seen in the range $|v_\parallel/v| < \sqrt{r/R_0}$ in which particles are bananas.

Bibliography

[1] F. Porcelli, R. Stankiewicz, H. L. Berk and Y. Z. Zhang, Phys. Fluids B **4**, 3017 (1992).

[2] F. M. Levinton, M. C. Zarnstorff, S. H. Batha, M. Bell, R. E. Bell, R. V. Budny, C. Bush, Z. Chang, E. Fredrickson, A. Jones, J. Manickam, A. Ramsey, S. A. Sabbagh, G. L. Schmidt, E. J. Synakowski, and G. Taylor, Phys. Rev. Lett. **75**, 4417 (1995).

[3] E. J. Strait, L. L. Lao, M. E. Manuel, B. W. Rice, T. S. Taylor, K. H. Burrell, M. S. Chu, E. A. Lazarus, T. H. Osborne, S. J. Thompson, and A. D. Turnbull, Phys. Rev. Lett. **75**, 4421 (1995).

[4] T. Fujita, S. Ide, H. Shirai, M. Kikuchi, O. Naito, Y. Koide, S. Takeji, H. Kubo, and S. Ishida, Phys. Rev. Lett. **78**, 2377 (1997).

[5] C. Gormenazo, Y. F. Baranov, C. D. Challis, I. Coffey, G. A. Cottrell, A. C. Ekedahl, C. M. Greenfield, A. C. Howman, G. T. A. Huysmans, M. Keilhacker, X. Litaudon, T. C. Luce, B. W. Rice, F. Rochard, G. J. Sadler, P. A. J. Schild, A. C. C. Sips, F. X. Söldner, E. J. Strait, B. J. D. Tubbing, M. R. Wade, and D. J. Ward, Phys. Rev. Lett. **80**, 5544 (1998).

[6] JET Team, Nuclear Fusion **39**, 1743 (1999).

[7] D. R. Baker, C. M. Greenfield, J. C. DeBoo, M. R. Wade, and B. W. Stallard, Phys. Plasmas **8**, 1565 (2001).

[8] F. L. Hinton and R. D. Hazeltine, Rev. Mod. Phys. **48**, 239 (1976).

[9] S. P. Hirshman and D. J. Sigmar, Nuclear Fusion **21**, 1079 (1981).

[10] K. C. Shaing, R. D. Hazeltine, and M. C. Zarnstorff, Phys. Plasmas **4**, 771 (1997).

[11] K. C. Shaing and R. D. Hazeltine, Phys. Plasmas **5**, 953 (1998).

[12] P. Helander, Phys. Plasmas **7**, 2878 (2000).

[13] Z. Wang, Plasma Phys. Control. Fusion **41**, A679 (1999).

[14] M. Taguchi, Journal of Plasma and Fusion Research **77**, 153 (2001).

[15] Z. Lin, W. M. Tang, and W. W. Lee, Phys. Plasmas **4**, 1707 (1997).

[16] W. X. Wang, N. Nakajima, M. Okamoto and S. Murakami, Plasma Phys. Control. Fusion **41**, 1091 (1999).

[17] W. X. Wang, F. L. Hinton, and S. K. Wong, Phys. Rev. Lett. **87**, 055002 (2001).

[18] A. Bergmann, A. G. Peeters, and S. D. Pinches, Phys. Plasmas **8**, 5192 (2001).

[19] M. Okamoto, N. Nakajima, S. Satake, and W. Wang, Journal of Plasma and Fusion Research **78** , 1344 (2002).

[20] I. B. Bernstein and K. Molvig, Phys. Fluids **26**, 1488 (1983).

[21] F. S. Zaitsev , M. R. O'Brien, and M. Cox, Phys. Fluids B **5**, 509 (1993).

[22] S. Wang, Phys. Plasmas **6**, 1393 (1999).

[23] S. Satake, H. Sugama, M. Okamoto and M. Wakatani, Journal of Plasma and Fusion Research **77**, 573 (2001).

[24] S. Satake, M. Okamoto, and H. Sugama, Phys. Plasmas **9**, 3946 (2002).

[25] P. Helander and D. J. Sigmar, *Collisional Transport in Magnetised Plasmas* (Cambridge University Press, 2002)

[26] T. H. Stix, Plasma Phys. **14**, 367 (1972).

[27] R. D. Hazeltine and J. D. Meiss, *Plasma Confinement* (Addison-Wesley Publishing Co., 1992)

[28] T. K. Chu, Phys. Plasmas **3**, 3397 (1996).

[29] J. Egedal, Nuclear Fusion **40**, 1597 (2000).

[30] V. A. Yavorskij, Zh. N. Andrushchenko, J. W. Edenstrasser, and V. Ya Goloborod'ko, Phys. Plasmas **6**, 3853 (1999).

[31] S. Wang, H. Sanuki, and H. Sugama, Phys. Plasmas **7**, 963 (2000).

[32] A. H. Boozer, Phys. Fluids **23**, 904 (1980).

[33] F. L. Hinton, in *Handbook of Plasma Physics*, Vol. 1 (North-Holland, Amsterdam, 1983), pp. 147-197.

[34] R. H. Cohen, K. Hizanidis, K. Molvig, and I. B. Bernstein, Phys. Fluids **27**, 377 (1984).

[35] J. W. Connor, R. C. Grimm, R. J. Hastie, and P. M. Keeping, Nuclear Fusion **13**, 211 (1973).

[36] R. D. Hazeltine, Phys. Fluids B **1**, 2031 (1989).

[37] T. Fujita, T. Oikawa, T. Suzuki, S. Ide, Y. Sakamoto, Y. Koide, T. Hatae, O. Naito, A. Isayama, N. Hayashi, and H. Shirai, Phys. Rev. Lett. **87**, 245001 (2001).

[38] M. Kotschenreuther, Bull. Am. Phys. Soc. **34**, 2107 (1988).

[39] Y. Chen and R. B. White, Phys. Plasmas **4**, 3591 (1997).

[40] X. Q. Xu and M. N. Rosenbluth, Phys. Fluids B **3**, 627 (1991).

[41] Z. Lin, W. M. Tang, and W. W. Lee, Phys. Plasmas **2**, 2975 (1995).

[42] S. Parker and W. W. Lee, Phys. Fluids B **5**, 77 (1993).

[43] G. Hu and J. A. Krommes, Phys. Plasmas **1**, 863 (1994).

[44] S. Brunner, E. Valeo, and J. A. Krommes, Phys. Plasmas **6**, 4504 (1999).

[45] C. S. Chang and F. L. Hinton, Phys. Fluids **29**, 3314 (1986).

[46] M. Okamoto, N. Nakajima, S. Satake, and W. Wang, Journal of Plasma and Fusion Research **78**, 1344 (2002).

[47] K. C. Shaing and R. D. Hazeltine, Phys. Fluids B **4**, 2547 (1992).

[48] G. M. Staebler, Plasma Phys. Control. Fusion **40**, 569 (1998).

[49] M. Wakatani, Plasma Phys. Control. Fusion **40**, 957 (1998).

[50] R. J. Hawryluk, in *Proceedings of the Course in Physics of Plasmas Close to Thermo-nuclear Conditions*, Varenna, 1979 (Commission of the European Communities, Brussels, 1980), Vol. I, P. 19.

[51] C. M. Greenfield, J. C. DeBoo, T. C. Luce, B. W. Stallard, E. J. Synakowski, L. R. Baylor, K. H. Burrell, T. A. Casper, E. J. Doyle, D. R. Ernst, J. R. Ferron, P. Gohil, R. J. Groebner, L. L. Lao, M. Makowski, G. R. McKee, M. Murakami, C. C. Petty, R. I. Pinsker, P. A. Politzer, R. Prater, C. L. Rettig, T. L. Rhodes, B. W. Rice, G. L. Schmidt, G. M. Staebler, E. J. Strait, D. M. Thomas, and M. R. Wade DIII-D Team, Phys. Plasmas **7**, 1959 (2000).

[52] M. N. Rosenbluth, R. D. Hazeltine, and F. L. Hinton, Phys. Fluids **15**, 116 (1972).

[53] S. Wang, T. Ozeki, J. Xie, and N. Hayashi, Phys. Plasmas **9**, 4654 (2002).